Peter Loidolt

Cold Deformation and Recrystallization of the Aluminium Alloy 6082

MASTER THESIS

For obtaining the academic degree
Diplom-Ingenieur

Master Programme of
Advanced Materials Science

Graz University of Technology

Supervisor:

Ass.Prof. Dr.techn. Maria Cecilia Poletti

Institute for Materials Science and Welding

Graz, March 2014

Statutory Declaration

I declare that I have authored this thesis independently, that I have not used other than the declared sources/resources, and that I have explicitly marked all material which has been quoted either literally or by content from the used sources.

Graz, _____ _____

Date Signature

Eidesstattliche Erklärung[1]

Ich erkläre an Eides statt, dass ich die vorliegende Arbeit selbstständig verfasst, andere als die angegebenen Quellen/Hilfsmittel nicht benutzt, und die den benutzten Quellen wörtlich und inhaltlich entnommenen Stellen als solche kenntlich gemacht habe.

Graz, am _____ _____

Datum Unterschrift

[1] Beschluss der Curricula-Kommission für Bachelor-, Master- und Diplomstudien vom 10.11.2008; Genehmigung des Senates am 1.12.2008

Contents

List of Figures

Thanks

This master thesis was written at the Institute for Materials Science and Welding at Graz University of Technology. I would like to thank my supervisors M.Sc. Romain Bureau and Prof. Cecilia Poletti for their supervision and the correction of this thesis. Further I would like to thank the head of the institute Prof. Christof Sommitsch for organising a scholarship and for providing the general framework.
During my experiments the assistance of the staff in the lab was very helpful for me. I am deeply grateful for that. I also want to thank my colleges in the office for the nice atmosphere. Special thanks are given to M.Tech. Surya Deo Yadav for supporting me during Gleeble experiments. Finally I want to thank all professors and assistants of the master programme Advanced Materials Science for giving me an insight into the wide field of materials science.

Abstract

The objective of this work is to describe the cold deformation of the aluminium alloy 6082 and to characterize and explain the formation of new grains during subsequent annealing. Therefore small samples cut out of a hot rolled sheet are cold deformed by means of plane strain compression tests. The measured data of the compression tests is used to calculate flow curves. Since the distribution of the strain is not uniform in plane strain deformed samples due to the geometry of the tools, finite element simulations and hardness mappings are performed to determine the local strain at every point of the cross section. Light microscopy pictures show an overview of the grain structure after cold deformation. Electron backscatter diffraction measurements reveal the substructure after cold deformation. High misoriented subgrains are formed during cold deformation near big second phase particles. These subgrains may act as nuclei for recrystallization during subsequent annealing.
After annealing of the cold deformed samples at different temperatures and for different holding times, hardness measurement and light microscopy is used to detect recrystallization. An annealing temperature of approximately 300°C is necessary to initiate recrystallization. At an annealing temperature of 350°C a minimum local strain of 0.4 is necessary to obtain full recrystallization. The investigation of partial recrystallized samples show the bulging of prior grain boundaries what refers to strain induced boundary migration as a nucleation mechanism. The growth of the new grains seems to be restricted to the grain boundaries of the cold deformed microstructure. A consequence is that after completed recrystallization grains still are elongated in the same direction as after cold deformation. Besides there are many small grains visible near to big second phase particles. So particle stimulated nucleation also takes place, but many grains nucleated at particles only end up as small island grains surrounded by bigger grains.

Kurzfassung

Das Ziel dieser Arbeit ist die Kaltverformung der Aluminiumlegierung 6082 zu beschreiben und die Bildung von neuen Körnern bei der anschließenden Glühung zu beobachten. Dazu werden kleine Proben eines warmgewalzten Bleches mit Hilfe von Kaltstauchversuchen unter ebener Dehnung verformt. Die gemessenen Daten des Stauchversuches werden für die Berechnung von Fließkurven herangezogen. Nachdem die Dehnungsverteilung bei den mit ebener Dehnung verformten Proben aufgrund der Werkzeuggeometrie nicht homogen ist, werden Finite Elemente Simulationen durchgeführt und Härtefelder angefertigt um die lokale Dehnung an jedem Punkt des Probenquerschnittes zu bestimmen. Lichtmikroskopiebilder geben einen Überblick über die Kornstruktur nach der Kaltverformung. EBSD-Versuche offenbaren die Substruktur nach der Kaltverformung. Subkörner mit einer hohen Missorientierung werden während der Kaltverformung in der Nähe von großen Ausscheidungen gebildet. Diese Subkörner könnten bei der anschließenden Glühung als Keime für die Rekristallisation agieren.
Nach der Glühung der kaltverformten Proben bei unterschiedlichen Temperaturen und für unterschiedliche Haltezeiten werden Härtemessung und Lichtmikroskopie verwendet um Rekristallisation nachzuweisen. Es ist eine Temperatur von ungefähr 300°C notwendig damit Rekristallisation starten kann. Bei einer Glühtemperatur von 350°C ist eine lokale Dehnung von etwa 0.4 notwendig um vollständige Rekristallisation zu erreichen. Die Untersuchung von teilweise rekristallisierten Proben zeigt das Auswölben von alten Korngrenzen was auf dehnungsinduzierte Korngrenzenbewegung als Keimbildungsmechanismus hinweist. Das Wachstum der neuen Körner scheint durch die alten Korngrenzen des kaltverformten Mikrogefüges begrenzt zu werden. Eine Konsequenz daraus ist, dass die neuen Körner nach abgeschlossener Rekristallisation nach wie vor in die gleiche Richtung ausgerichtet sind wie nach der Kaltverformung. Es sind außerdem noch viele kleine Körner in der Nähe von großen Ausscheidungen sichtbar. Es findet also auch von Ausscheidungen stimulierte Keimbildung für die Rekristallisation statt, jedoch verbleiben viele dieser Körner als kleine Inselkörner umgeben von größeren Körnern.

Part I.
Introduction

After a short motivation, the most important physical aspects which are related to cold deformation and recrystallization of metals are discussed, including metal structure, plastic deformation of metals and annealing phenomena of metals. As an aluminium alloy is used in the experiments, the focus of this fundamental part will be on aluminium.

1. Motivation

If metals are cold deformed and subsequent annealed at a temperature of approximately $0.4T_m$ (melting temperature in Kelvin), they start to recrystallize. Recrystallization originates at special places, where nuclei are formed, which are able to growth. One of the most important nucleation sites are grain boundaries of prior cold deformed grains. If there are hard particles included in the material, they also may act as nucleation sites (see figure 1). If nucleation occurs near to particles it is called particle stimulated nucleation PSN.

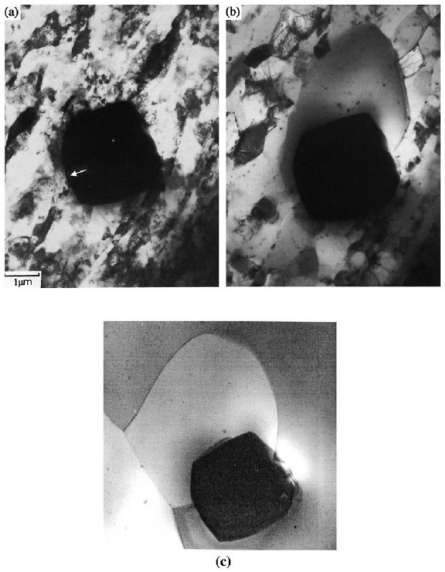

Figure 1: In-situ observation of PSN in Al-Si [1]

In PSN high misoriented subgrains near to particles grow very fast and form small grains, which are able to grow further. If these grains grow too slow, they get surrounded by other grains which grow faster (figure 1(c)). Figure 2 shows the condition necessary to initiate PSN in an aluminium monocrystal. The particle size should be at least 2 microns at high strains. At low strains, bigger particles are necessary to produce nuclei.

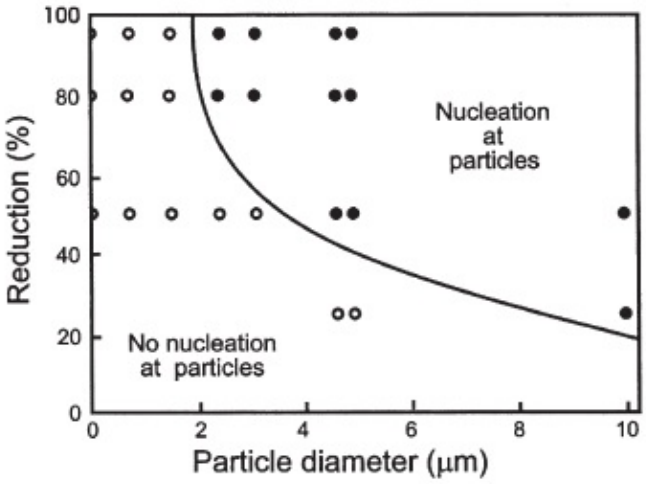

Figure 2: Critical conditions for PSN in an Al-Si monocrystal[1]

The aluminium alloy 6082 includes hard particles, which seem to be suitable for PSN, but it is not clear, if PSN is an important nucleation mechanism for recrystallization. The aim of this work is to characterize and explain the influencing factors for recrystallization after cold deformation. The plastic strain, the annealing time and the annealing temperature seem to be the most important parameters. During analysis of recrystallized microstructure, the actual nucleation sites should be observed.

2. Metal Physics

2.1. Structure

Metals are built up as a regular arrangement of atoms, called the crystal lattice or simply lattice. If there are no defects, a whole macroscopic part can be described as an arrangement of the unit cell, which is the face centred cubic (fcc) unit cell in case of aluminium (figure 3).

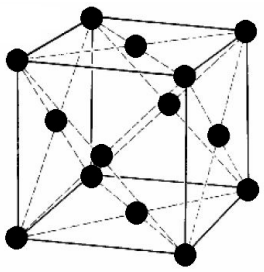

Figure 3: Unit cell of a fcc crystal [2]

In real metals there are always defects, which have a big influence on mechanical prop-

erties. One kind of these defects are dislocations. They appear if there is an additional or missing lattice plane. Dislocations are divided into screw and edge dislocations (see figure 4).

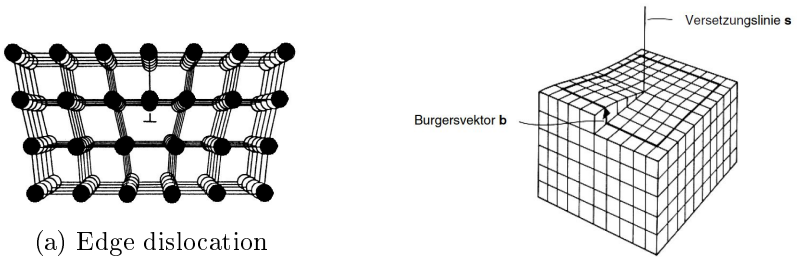

(a) Edge dislocation

(b) Screw Dislocation

Figure 4: Comparison of edge dislocation (a) and screw dislocation (b) [2]

Dislocations are important for metals, because their movement cause plastic deformation. During plastic deformation dislocations preferentially glide on the most densely packed lattice planes in the most densely packed direction. The combination of a slip plane and a slip direction yields a slip system. In fcc crystals, for example, there are 4 different slip planes and each of them has 3 slip directions. So there are 12 slip systems. Technical metallic parts usually do not consist of a single crystal but of a huge amount of grains of different orientations. The areas, which separate different grains, are called grain boundaries. The rotation axis and the rotation angle necessary to rotate one grain into the orientation of the neighbouring grain, are used to characterize grain boundaries. If the rotation axis is normal to the grain boundary, it is called pure twist boundary (figure 5 a). If the rotation axis is located in the grain boundary, it is a pure tilt boundary (figure 5 b and c). Tilt boundaries are either symmetric (c) or asymmetric (b).

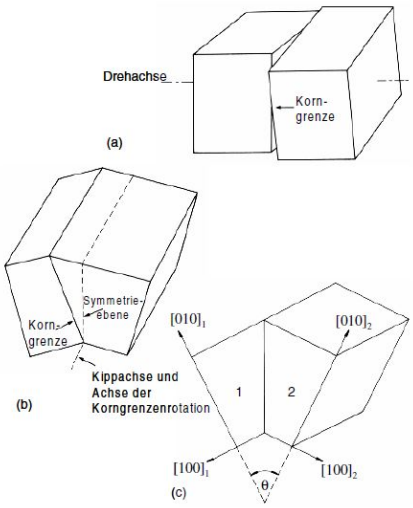

Figure 5: Comparison of a twist boundary (a), a non-symmetric and a symmetric tilt boundary (b) and (c) [2]

Grain boundaries with high rotation angles are called high angle grain boundaries HAGB, and boundaries with low angles are called low angle grain boundaries LAGB or subgrains. The upper limit for LAGB is approximately 15°. In the range of 0° to 15°, grain boundaries can be described as an arrangement of dislocations (see figure 6). The misorientation of such a LAGB can be calculated as function of the dislocation spacing.

$$\Theta \cong \frac{b}{D} \tag{1}$$

Here Θ is the misorientation, b the burgers vector and D the dislocation spacing.

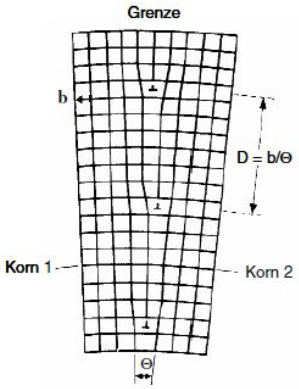

Figure 6: Structure of symmetric low angle tilt boundary [2]

This model fails if the misorientation exceeds 15°, because in that case the dislocation cores begin to overlap. Also the grain boundary energy rises with increasing misorientation and reaches a maximum level between 10° and 15° (see figure 7).

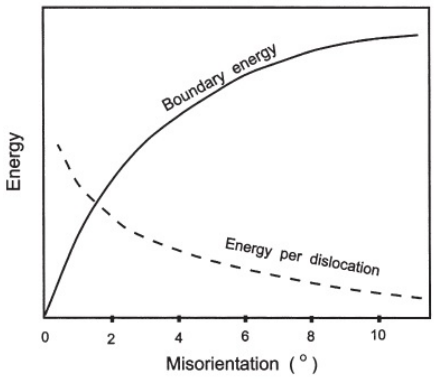

Figure 7: Grain boundary energy as a function of misorientation [1]

Technical metals are never pure, because there are always some foreign atoms included. Some of them are impurities from production processes and some of them are added on purpose to alter the properties of the material. Foreign atoms whether are in solution at lattice points and interstitial space or they build a second phase. If the amount of foreign atoms is rather small (up to some percent) and they build a second phase, they form particles surrounded by the matrix of the host material. Depending on the annealing treatment, the particles have different sizes. The particles in the range of nanometres are important for the strengthening of metals. The particles of micron scale cause a heterogeneous deformation of the matrix, which is of special interest for the nucleation of recrystallization.

2.2. Deformation

Plastic deformation in metals occurs either by slip of dislocations or by twinning. In aluminium alloys, dislocation slip is preferred. The relation between the shear rate $\dot{\gamma}$ and dislocation movement is given by Orowan equation (equation 2), where ρ_m is the density of mobile dislocations, b burgers vector and v the speed of mobile dislocations.

$$\dot{\gamma} = \rho_m b v \tag{2}$$

To move dislocations, a minimum resolved shear stress τ is necessary [2]

$$\tau = \alpha G b \sqrt{\rho_s} \tag{3}$$

where α is a geometric factor in range of 0.5, G is the shear modulus and ρ_s is the density of stored dislocations. Usually the applied force is not oriented to cause pure shear stress in the slip system of interest. For this reason Schmid introduced a law which correlates the tensile stress σ with the resolved shear stress τ in one special glide system (equation 4). Here κ is the angle between tensile direction and normal direction of the gliding plane and λ is the angle between tensile direction and glide direction (see figure 8).

$$\tau = \sigma \cos\kappa \cos\lambda = m\sigma \tag{4}$$

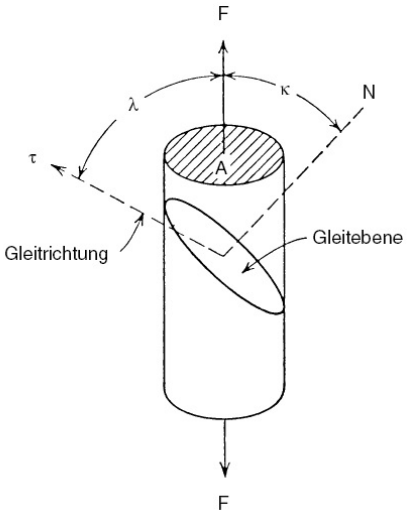

Figure 8: Resolved shear stress in a monocrystal [2]

The factor m is the Schmid's factor, whose maximum value is 0.5 (in the case of $\kappa = \lambda = 45°$). This expression is only valid for monocrystals. In case of polycrystalline fcc metals, Taylor computed the so called Taylor's factor M_T,

$$M_T = \frac{1}{m} = 3.06 \tag{5}$$

which yields an average Schmid's factor of $m = 0.327$. Combining equation 4 and equation 3 yields a relation between the stress and the dislocation density. Taking the average Schmid's factor m=0.327 into account the stress reads

$$\sigma = \frac{\tau}{m} = \frac{\alpha G b \sqrt{\rho_s}}{m} = 1.53 G b \sqrt{\rho_s} \tag{6}$$

where α is assumed to be 0.5. Since there may also be a flow stress at zero dislocation density, the constant σ_0 is added to get the actual flow stress.

$$\sigma = \sigma_0 + 1.53 G b \sqrt{\rho_s} = \sigma_0 + 1.138 \cdot 10^{-5} \sqrt{\rho_s} \tag{7}$$

The material data of aluminium ($G = 26000$MPa and $b = 2.86 \cdot 10^{-10}$m) is used here.

2.3. Hardening

During plastic deformation the yield stress increases. Figure 9 reveals the hardening behaviour of a polycrystalline aluminium alloy, which is shear deformed. The deformation process can be divided in different stages. At stage I, which only appears in monocrystals, there is a slight increase of stress. Dislocations are able to move easily and it is therefore also called "easy glide"-region. At some point, dislocations start to interact with each other, whereby some of them get immobile. To enable further plastic strain,

new dislocations have to be built, leading to an increase of stress. The zone of strong, constant hardening is called stage II hardening. At one point strong hardening of stage II starts to decrease continuously. The zone of decreasing hardening (bended curve) is called stage III hardening. Here stress is high enough for screw dislocation to leave their slip planes and make cross slip to compass obstacles. After stage III the hardening gets constant again in stage IV. In stage IV the hardening is much weaker than in stage II.

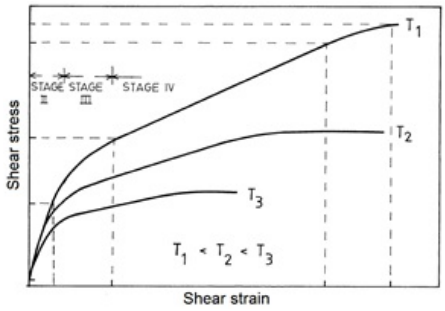

Figure 9: Hardening stages of a polycrystalline aluminium alloy [3]

2.4. Recovery

Dislocations store elastic energy in the surrounding distorted lattice. In case of an edge dislocation, there is a compression strain on the side of additional lattice plane and a tensile strain on the opposite side (figure 10).

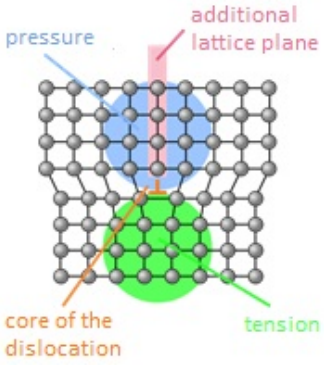

Figure 10: Stress field near to an edge dislocation [4]

The dislocations do not only feel the stress field of external loads, but also the stress field of other dislocations leading to interaction of dislocations with each other. They are able to reduce their stored energy if they build special arrangements. In these arrangements, the zones of tensile strain overlap with the zones of compressive strain. In the special case of edge dislocations with the same burgers vector (figure 11), they are in a stable arrangements if they built a vertical line (see figure 12a). These arrangements

lead to kinks in the crystal orientation. If there are many kinks, crystal orientation looks like a polygon. Thus the formation of these arrangements is called polygonisation.

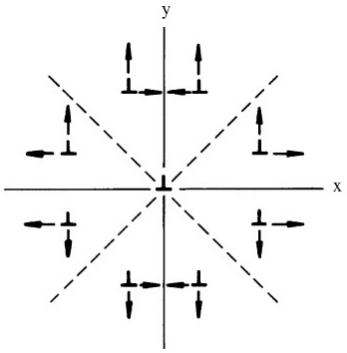

Figure 11: Interaction forces of dislocations [2]

In the case of two dislocations with opposite burgers vectors on the same slip plane, they are able to annihilate. The combination of rearrangement and annihilation of dislocations is called recovery. If recovery takes place during deformation it is called dynamic recovery. If recovery takes place after deformation it is called static recovery. To enable recovery, the dislocations have to be mobile since they have to change their position. At low temperatures, only slip of edge dislocations and slip and cross slip of screw dislocations is possible and the rearrangement of dislocations is limited. At higher temperatures, dislocations are able to climb as well. In doing so, they change their glide plane and additional slip is possible. This is the reason for lower stresses at higher temperatures due to dynamic recovery in figure 9. Climbing at higher temperatures is also the reason why cell walls of cold deformed aluminium (figure 12b left) get thinner during annealing (figure 12b right).

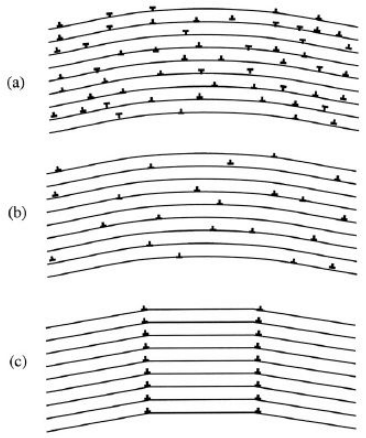

(a) Polygonisation principle

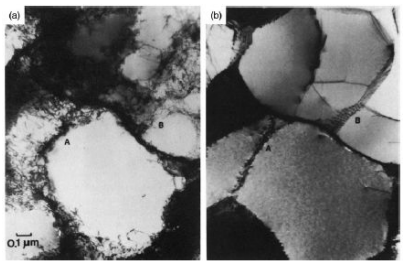

(b) Polygonisation in an aluminium alloy after cold deformation (left) and annealing (right) (TEM)

Figure 12: Principle of polygonisation (a) and real observation (b) [1]

2.5. Recrystallization

During recovery not all the dislocations annihilate. Most of them stay in the material. To get a crystal of really low dislocation density (some orders of magnitude lower than after cold deformation) recrystallization has to take place. During recrystallization new grains are built. The stored energy of dislocations acts as driving force for this process. For Humphreys [1] growing of new grains during recrystallization can be described as boundary movement due to a difference in stored energy on two sides of a boundary (figure 13).

$$P_D = G^A - G^B = \Delta G \tag{8}$$

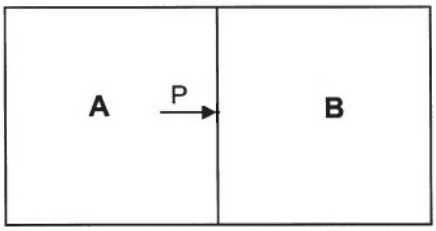

Figure 13: Driving pressure on boundary during recrystallization [1]

P_D is the driving pressure for the boundary movement and is equal to the difference in free energy per unit volume ΔG of A and B. In addition to the driving pressure, there are also retarding pressures P_Z and P_C due to dragging of precipitates (called Zener-drag pressure) and due to boundary curvature [1]. The net driving pressure P reduces to

$$P = P_D - P_Z - P_C = \frac{\alpha \rho G b^2}{2} - \frac{3 F_V \gamma_b}{d} - \frac{2\gamma_b}{R} \tag{9}$$

where F_V is the phase volume fraction of second phase particles, γ_b is the boundary energy, d is the second phase particle diameter and R is the radius of the growing grain. For boundary movement, a positive net driving pressure is necessary. Reformulation of equation 9 yields in the critical grain size R_c to initiate recrystallization:

$$R_c = \frac{2\gamma_b}{P_D - P_Z} \tag{10}$$

2.6. Nucleation for Recrystallization

Recrystallization originates from nucleation sites in the material. Due to comparable low driving forces, the classical nucleation theory does not apply for the nucleation of recrystallization. There is an agreement that nuclei have to exist in the deformed microstructure [1] [2].
There are two basic possibilities for nucleation: bulging of existing HAGB and introduction of a nucleus during deformation. The reason of bulging grain boundaries is the difference in strain energy. This mechanism is called strain induced boundary migration

SIBM. In figure 14a grain 1 has a lower stored energy than grain 2 and the boundary bulges from 1 to 2. There are two possibilities concerning the size of the bulging boundary. Whether the bulge is bigger than the cells of the original grain (figure 14b and figure 14c), leading to multiple subgrain SIBM, or the nucleus is one big cell figure 14d, which leads to single subgrain SIBM. In the case of multiple subgrain SIBM, the substructure remains in the nucleus (figure 14b) or not (figure 14c).

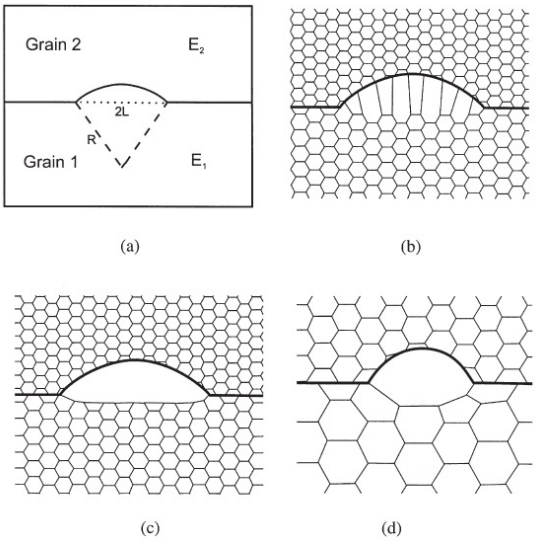

Figure 14: Explanation models for strain induced boundary migration[1]

A well arranged substructure is visible in figure 15, where SIBM takes place at a broad front. Here, the HAGB are shown in black and the LAGB in white. Remaining substructure causes a drag of moving boundary.
Figure 15 refers to the nucleation mechanism in figure 14 (b), in which a substructure remains in the growing grain. The density of substructure decreases if the actual area of moving boundary increases during recrystallization (see also conclusion in [8]). From the geometrical point of view it is obvious to have a higher total amount of substructure in case of a broad nucleation front. Since substructure causes an additional drag of moving boundary, slim nucleation front should be preferred as long as critical radius of bulging boundary is exceeded (compare with equation 10). In case of single subgrain SIBM, there is no substructure in the growing nucleus, but the radius of growing nucleus is limited to the subgrain size of some microns.

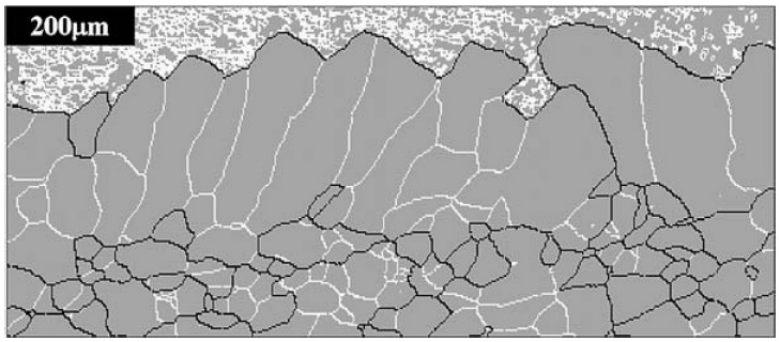

Figure 15: EBSD map of a broad front SIBM in an Al-0.12wt.%Sc alloy [5]

The second possibility of nucleation for recrystallization is the production of a nucleus and its mobile boundary during deformation and subsequent annealing. It is supposed, that the nuclei with HAGB originate from cells or subgrains. Referring to [1], following points seem to be clear:

- The orientation of the nucleus is present in the deformed structure
- Nucleation occurs by the growth of subgrains
- There must be an orientation gradient present.

There are some sites in the microstructure where inhomogeneous deformation takes place and high orientation gradients develop. These are preferential sites for nucleation.

- Grain boundaries
  In contrast to SIBM it is also possible to get nuclei near grain boundaries, which do not have the orientation of parent grain. One reason may be the activation of many different slip systems, to overcome the complex deformation mode near the grain boundaries, whereby high orientation gradients are produced. The generation of a nucleus near a grain boundary with a new orientation is more frequent if the strain increases.

- Transition bands
  Transition bands divide areas of one grain, which have split in two different orientations during plastic deformation. There are great long range orientation gradients within these bands like in figure 16.

- Shear bands
  Shear bands are thin highly strained regions which are usually oriented in 35° with respect to the rolling plane. There are high strains and high strain gradients in these bands which promote nucleation.

- Hard particles
  Hard particles cause a heterogeneous deformation, increased stored energy and high orientation gradients. Particles bigger than 1 micron can act as nucleation sites.

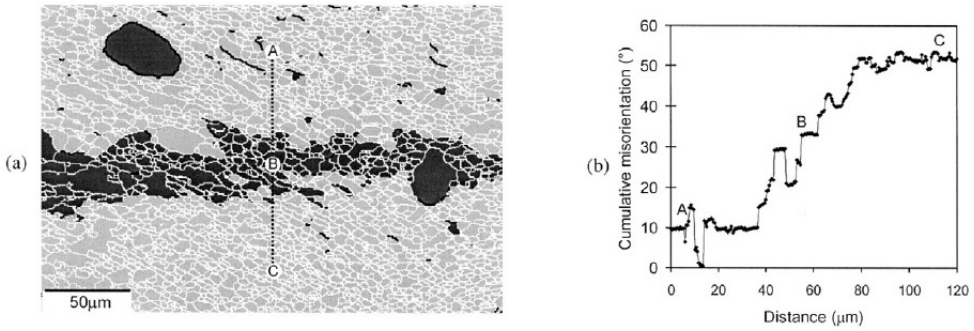

Figure 16: EBSD map (a) and cumulative misorientation (b) of a transition band [1]

3. Previous Study on AA6082

The material AA6082, which is considered in this thesis, was already investigated in [6]. In that work cold rolled sheets are oven annealed at 330°C up to 370°C for 2 to 60 minute holding time. In figure 17 a cold rolled and a cold rolled + annealed sample are compared. The sample in figure 17b seems to be full recrystallized after 2 minutes annealing at 330°C. Since all other samples are annealed for longer time and/or at higher temperatures, all samples can be considered as fully recrystallized.

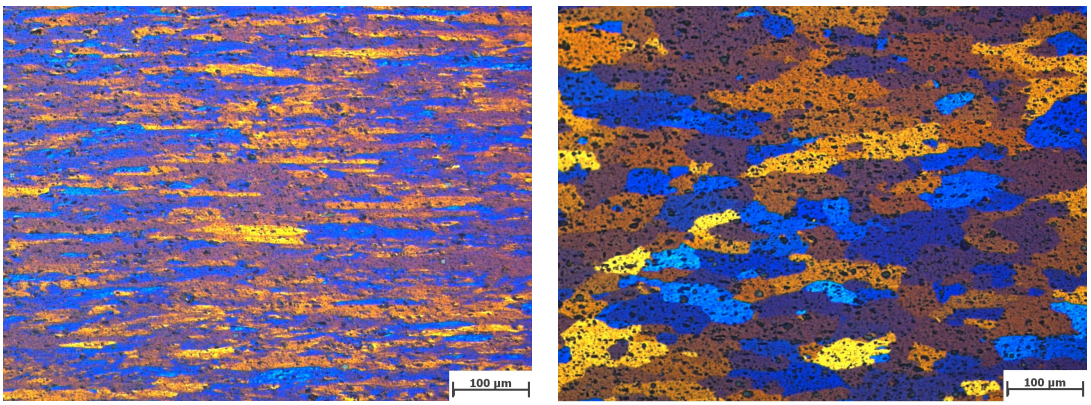

(a) cold rolled (b) annealed at 330°C for 2 minutes

Figure 17: LOM micrograph comparing two samples cold rolled (a) and cold rolled + annealed (b) analysed normal to rolling direction [6]

In figure 18 a cold rolled and a cold rolled + annealed sample analysed in the rolling direction are compared. After cold rolling the grains are elongated in the rolling direction. After recrystallization, the grains still are slightly elongated (figure 18b).

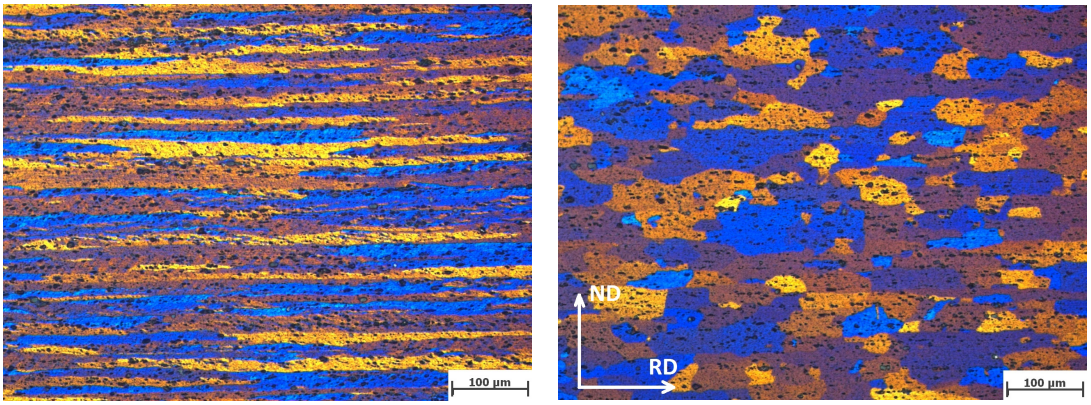

(a) cold rolled (b) annealed at 370°C for 10 minutes

Figure 18: LOM micrographs comparing two samples cold rolled (a) and cold rolled + annealed (b) analysed in rolling direction [6]

Figure 19 shows the grain area in the cross section of the sample, as well as the ratio of the grain length to the grain height for different annealing temperatures and times. The grain length is the average extension of the grains in the rolling direction, whereas the grain height is the average extension in the normal direction. The grains are elongated in the rolling direction, which is also visible in figure 18b. There is no clear trend for grain growth after annealing for long times.

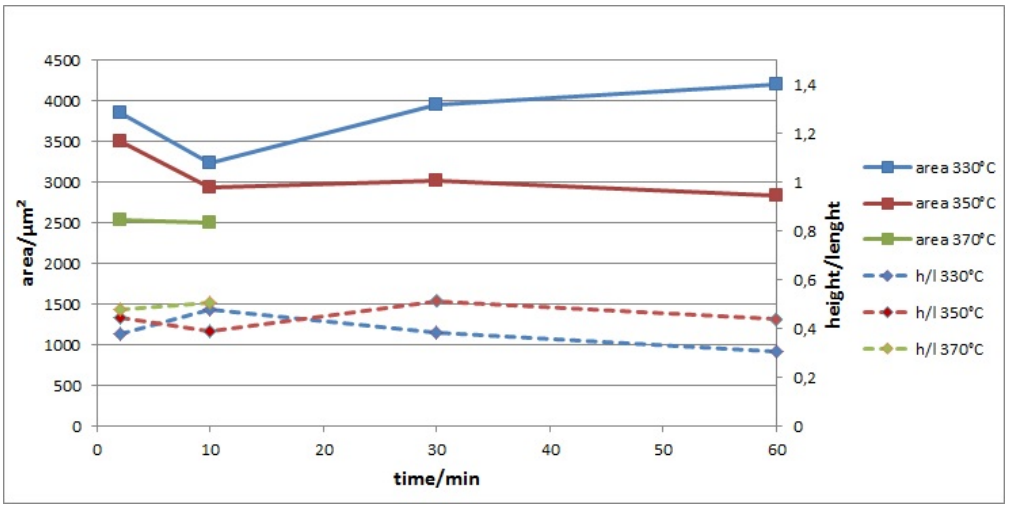

Figure 19: Grain size and elongation of recrystallized samples after annealing [6]

In this previous work only full recrystallization is observed. Thus, it is not possible to observe the sites where recrystallization originates. To find nuclei for recrystallization, partially recrystallized samples have to be investigated. Therefore the annealing temperature and holding time has to be reduced.

Part II.
Methods

This thesis includes the characterisation of different pre-stages of recrystallization at different length scales. On the one hand hardening and softening is considered at a macroscopic scale, on the other hand the formation of possible nuclei and the growth of new grains is considered on a microscopic scale. For this reasons sheet samples are cold deformed in plane strain compression tests. Finite element simulations of plane strain tests are performed to compute the local strains. Cold deformed samples are annealed to initiate recovery and recrystallization. Hardness measurements give information about the local hardening as well as the local softening. The local hardening obtained from FE-simulations should be comparable to the hardness measurements. Optical microscopy is used to investigate the microstructure after cold deformation and the microstructural change during annealing. Finally EBSD measurements produce more detailed information about the microstructure and give an idea of the possible nucleation sites.

4. Material (+ Heat treatment)

For the experiments, the aluminium alloy AA6082 is used. For the chemical composition look at table 1. The material is received as hot rolled and recrystallized sheet metal of 3.9mm thickness. Alternatively a cold rolled sheet reduced to 1.8mm is available.

Table 1: Chemical composition of AA6082 (wt%)

Material	Mg	Al	Si	Mn	Fe	Cu	Cr	Zn	Ti
AA6082	0.6-1.2	balance	0.7-1.3	0.4-1.0	0.5	0.1	0.25	0.2	0.1

The material contains two types of second phase particles which are visible in the chemical contrast image (see figure 20). On the one hand there are particles consisting of AlFeSi, which appear bright in the chemical contrast. On the other hand there are black Mg_2Si particles. The size distribution of AlFeSi particles is spread over 2 orders of magnitude. There are some very big particles with a diameter of approximately 10 microns and also many small particles of less than 0.1 micron. The size of Mg_2Si particles is in the range of 1 micron up to 5 microns.

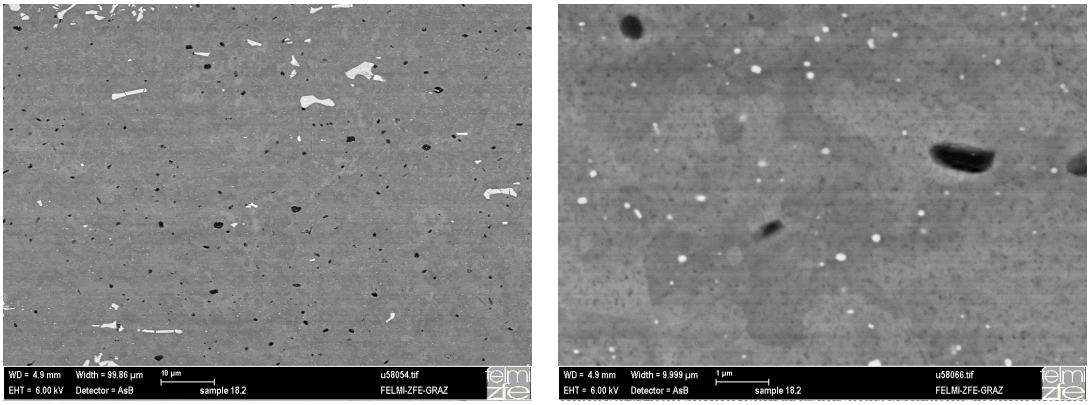

(a) Overview (b) Detail

Figure 20: Chemical contrast in the hot rolled material showing particle morphology and distribution

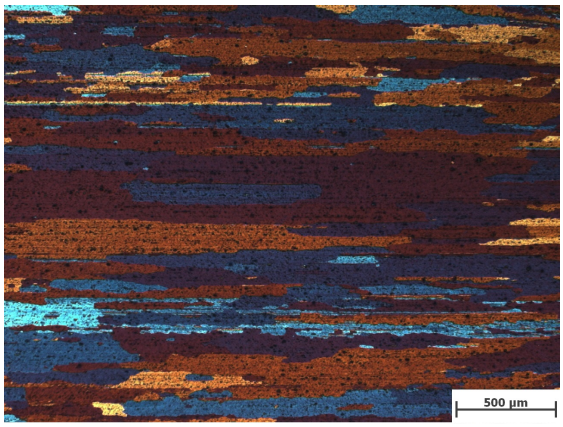

Figure 21: Optical micrograph showing the grain structure after hot rolling

The optical micrograph of the hot rolled sample shows elongated grains in the rolling direction (figure 21). In a past work [6], the average grain size was found to be 680 microns in the rolling direction, 430 microns in the transverse direction and 85 microns in the normal direction.
In order to change the particle morphology, a homogenisation treatment is performed. The material is heated up to 530°C and held for 20 hours at this temperature. After holding time it is slowly cooled to 350°C and held again for 4 hours to finish precipitation. Finally it is cooled down to room temperature slowly. The whole process is shown in figure 22.

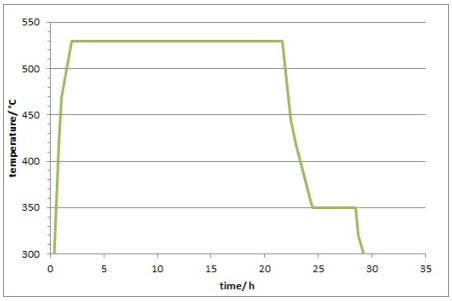

Figure 22: Temperature sequence of performed homogenisation treatment

After the homogenisation treatment Mg_2Si particles are much bigger than before. The number of Mg_2Si particles decreased. AlFeSi particles do not dissolve at 530°C and so they stay more or less the same. As the homogenized material differs from the origi-

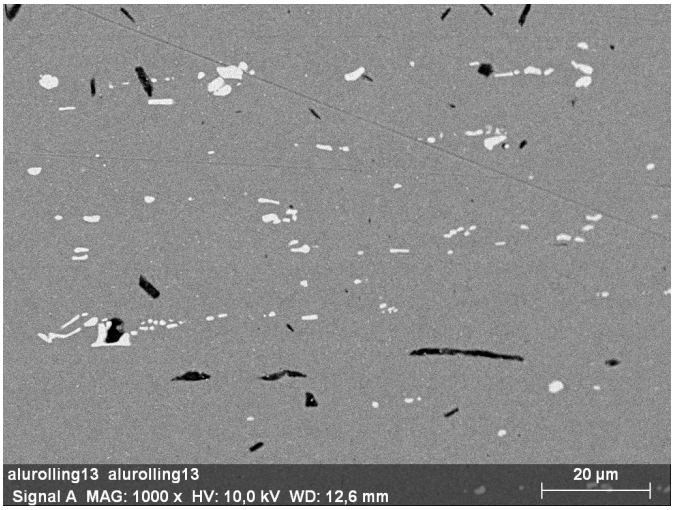

Figure 23: Phase contrast of homogenised material

nal hot rolled material, there are finally 3 different states of one material available for experiments. These are

- hot rolled
- hot rolled + cold rolled
- hot rolled + homogenized

5. Thermomechanical Treatments

5.1. Gleeble Plane Strain Tests

A Gleeble® 3800 machine is used to perform the plane strain compression tests. The hot rolled and hot rolled + homogenized samples are cold deformed and subsequently annealed. The annealing treatment is discussed in section 5.3.

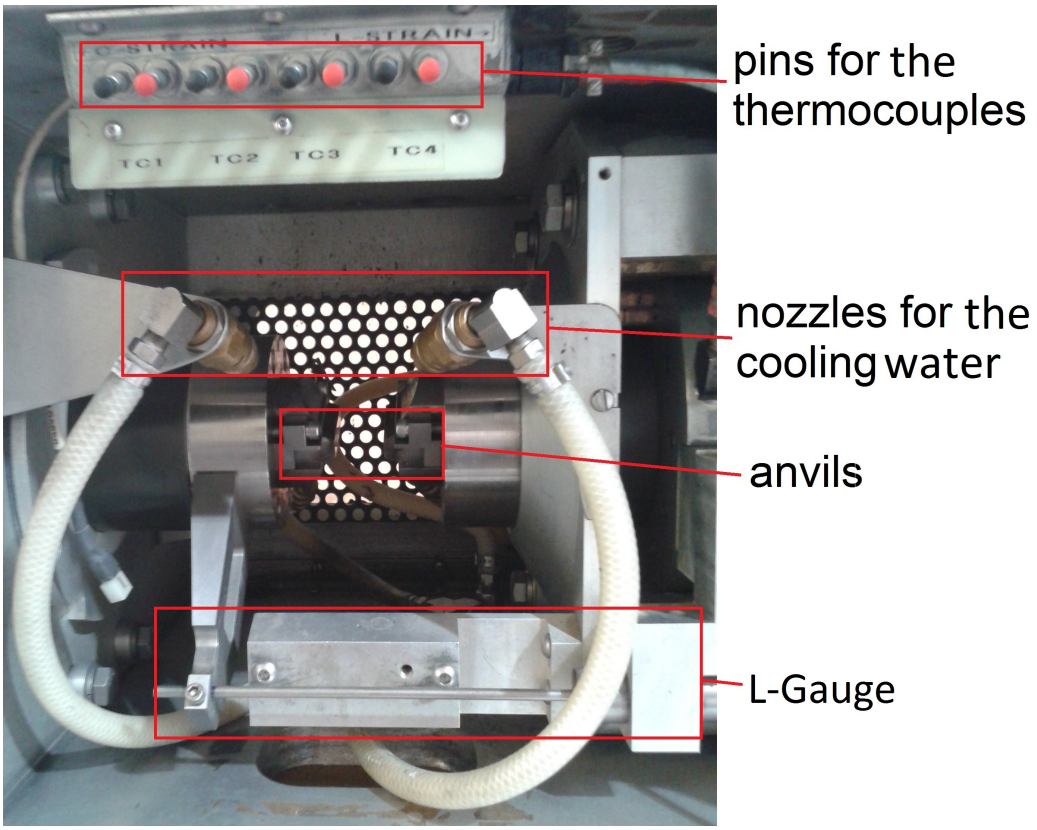

Figure 24: Working chamber of Gleeble machine

The plane strain tests are performed to physically simulate the rolling process. The geometry of the tools and the samples (in figure 25) cause plastic deformation in only two directions (h,w). The plastic flow into the third direction (t) is inhibited.

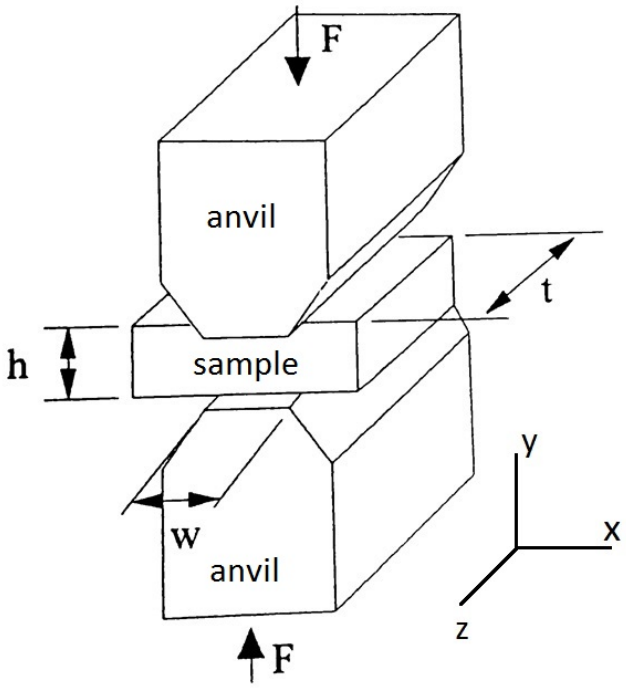

Figure 25: Geometry of a plane strain test [7]

There are some restriction concerning the geometry. To get as little deviation as possible from the plane strain conditions, t should be considerably greater than w and w should be greater than h ($t>>w>h$). In the standard tests performed in this work, the following geometry is used

- t=20mm
- w=5mm
- h_0=3.9mm
- h_f=2.35mm

in which h_0 is the initial thickness of the sheet, t is the lenght of the sample and w is given from the geometry of the tools. To get a true strain of 0.5, the sample has to be compressed to a final thickness h_f=2.35mm.
To obtain flow curves from plane strain experiments, there are some calculations necessary. The stress in compression direction σ_{yy} can be calculated very easily with

$$\sigma_{yy} = P = \frac{F}{wt} \tag{11}$$

where P is the pressure normal to the sample surface due to compression force F and w and t can be obtained from figure 25. The plane strain condition introduces an additional

stress. Due to the conservation of volume during plastic deformation, the stress in the z-direction σ_{zz} can be computed with [9]

$$\sigma_{zz} = \frac{1}{2}(\sigma_{xx} + \sigma_{yy}) \tag{12}$$

where the stress in x-direction $\sigma_{xx} = 0$ in case of zero friction. Using the von-Mises flow theory

$$f = \frac{1}{2\sigma_v^2}\left[(\sigma_{xx} - \sigma_{yy})^2 + (\sigma_{yy} - \sigma_{zz})^2 + (\sigma_{zz} - \sigma_{xx})^2\right] - 1 = 0 \tag{13}$$

yields

$$\sigma_v^2 = \frac{1}{2}\left[(0 - \sigma_{yy})^2 + \left(\sigma_{yy} - \frac{1}{2}\sigma_{yy}\right)^2 + \left(\frac{1}{2}\sigma_{yy} - 0\right)^2\right] = \frac{3}{4}\sigma_{yy}^2 \tag{14}$$

and finally the equivalent stress σ_v is

$$\sigma_v = \frac{\sqrt{3}}{2}\sigma_{yy} = \frac{\sqrt{3}}{2}\frac{F}{wt} \tag{15}$$

and the corresponding equivalent strain ε_v is

$$\varepsilon_v = \frac{2}{\sqrt{3}}\varepsilon_{yy} = \frac{2}{\sqrt{3}}\ln\left(\frac{h}{h_0}\right) \tag{16}$$

where h is the actual height of the sample. If friction also should be taken into account, it may look like in figure 26.

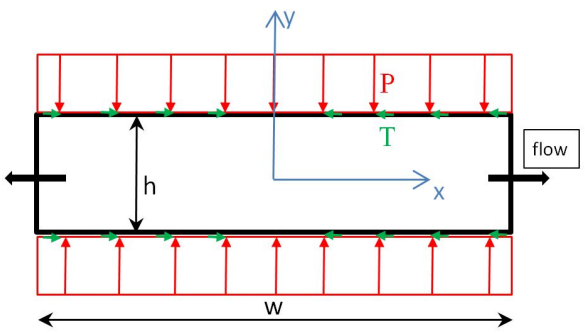

(a) Stresses acting on surface

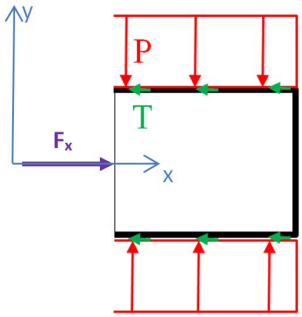

(b) Additional internal force due to friction

Figure 26: Influence of friction

In addition to the pressure P, which is necessary for the compression, there is a tangential frictional stress T, acting opposite to the flow direction. If the coefficient of friction μ is known, the tangential stress can be calculated with

$$T = \mu P \tag{17}$$

This tangential stress introduces an additional force in x-direction F_x normal to yz-plane (see figure 26b). If P and μ are considered as constant this force can be calculated for one special value of coordinate x with

$$F_x = 2P\mu\left(\frac{w}{2} - x\right)t \tag{18}$$

This internal force has to be carried by the material leading to an additional compression stress in the x-direction. If uniform stress is assumed the stress σ^*_{xx} at one point x reads

$$\sigma^*_{xx} = \frac{F_x}{ht} = \frac{2P\mu\left(\frac{w}{2} - x\right)}{h} \tag{19}$$

Then, the maximal stress in the x-direction is in the center of the sample. It increases with the pressure P, the coefficient of friction μ and the width of the tool w. It decreases when the height h of the sample increases. For the calculation of the flow curves, it is more convenient to have only one average stress σ_{xx}. This stress can be calculated for $x = w/4$ with

$$\sigma_{xx} = \frac{\sigma_{yy}\mu w}{2h} \tag{20}$$

where P is substituted by the internal stress in the y-direction. Now the equivalent stress is calculated using the von-Mises theory (equation 13), where σ_{xx} and σ_{zz} are substituted with equation 20 and 12.

$$\sigma_v^2 = \frac{1}{2}\left[\left(\frac{\mu w}{2h}\sigma_{yy} - \sigma_{yy}\right)^2 + \left(\sigma_{yy} - \left(\frac{\mu w}{4h} + \frac{1}{2}\right)\sigma_{yy}\right)^2 + \left(\left(\frac{\mu w}{4h} + \frac{1}{2}\right)\sigma_{yy} - \frac{\mu w}{2h}\sigma_{yy}\right)^2\right] \tag{21}$$

Finally one gets:

$$\sigma_v = \frac{1}{\sqrt{2}}\sigma_{yy}\left[\frac{3}{2} - \frac{21\mu w}{16h} + \frac{9\mu^2 w^2}{16h^2}\right]^{\frac{1}{2}} \tag{22}$$

In case of vanishing friction equation 22 yields, as expected, the same solution as equation 15. Taking equation 22 into account, the influence of friction can be estimated. A correction factor CF is introduced, which is the ratio of equation 22 and equation 15. If the following parameters are chosen to calculate one special correction factor:

- $\mu = 0.1$
- $w = 5mm$ (tool width)
- $h = 3.9mm$ (sheet thickness)

then,

$$CF = \frac{\frac{1}{\sqrt{2}}\sigma_{yy}\left[\frac{3}{2} - \frac{10.5}{62.4} + \frac{2.25}{243}\right]^{\frac{1}{2}}}{\frac{\sqrt{3}}{2}\sigma_{yy}} = 0.95 \tag{23}$$

This means that the flow stress is overestimated a little bit if the friction is omitted (as in equation 15). As the experiments are performed at room temperature and lubricant

is used to reduce the friction, it is assumed that this influence can be very low. Thus the equivalent stress expressed in equation 15 may be accurate enough. Equation 22 is then useful, if friction is high, but no sticking between anvils and sample occurs. The way to account for sticking conditions is shown in [9].
After many experiments, tools are damaged. Especially, tool heating causes that the tool surface gradually gets rough due to sparks (see figure 27). Referring to equation 22 surface roughness has an influence on the flow stress, because it enhances the friction and hinders the material flow. However, no increase in the flow stress has been noticed after 20 experiments.

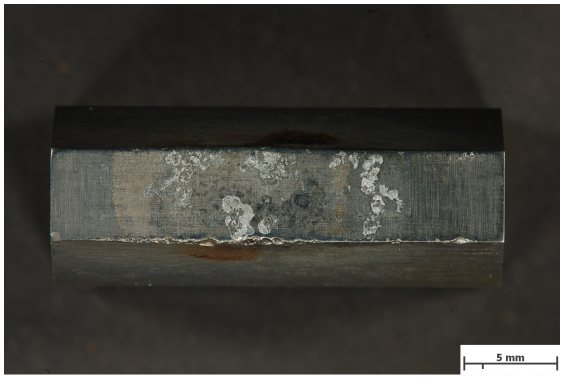

Figure 27: Damaged anvil

The standard compression tests are performed at a comparable low strain rate of 0.01. Usually there should be no strain rate sensitivity in cold deformation. Nevertheless also tests at strain rate of 0.1 and 1 are performed.
To get information about the influence of the tool geometry and the friction, some additional tests are performed with bigger tools, having the following geometry:

- w=10mm
- t=35mm
- h_0=3.9mm

Two experiments are carried out without lubricant and two experiments with lubricant (nickel based lubricant [10]). As the ratio w/h is greater, the friction should have more influence when the tools are bigger.

5.2. Tensile Tests

When extracting the flow curves from the compression tests, there are always some uncertainties. As discussed in section 5.1, friction is one possible problem. In tensile tests, there is no friction and so it is possible to compare the data obtained from the compression tests. Tensile tests are performed with a Zwick tensile test machine (figure

28). Simple rectangular stripes of hot rolled material as well as one stripe of cold rolled material are used for the test.

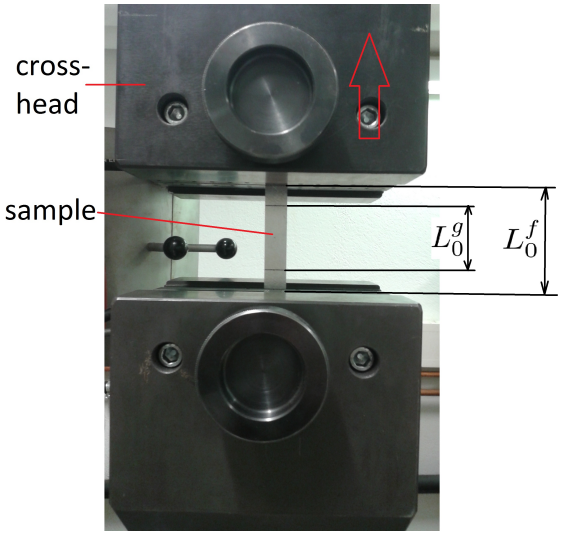

Figure 28: Zwick tensile test machine

- cross section 20mmx3.9mm (hot rolled)
- cross section 15mmx1.8mm (cold rolled)
- free clamping length L_0^f=80mm
- gauge length L_0^g=50mm

The samples are stretched in the rolling direction. There are two different length measurement systems installed. The extensometer is directly attached to the sample and measures the gauge length L_0^g very precisely, and is only usable at very low strains. It is used to determine the Young's modulus and the yield stress. The second measurement system measures the displacement of the crosshead. The displacement of the crosshead equals more or less the change of free clamping length L_0^f, but there is also an influence of the elastic deformation of the machine. It is less precise than the extensometer, and is used for large strains up to fracture.

In tensile tests, stress and strain are always calculated with respect to initial cross section and initial length. As they are very common in engineering, they are called engineering values. In a more physical context, usually the true (or logarithmic) stress and strain are used. There are different nomenclatures for engineering and physical values possible. In this thesis σ_e and e refer to engineering stress and strain respectively, whereas σ and ε refer to true values. In case of uniaxial tensile tests, these values can be computed with the following equations (taken from [11])

$$\sigma = \frac{F}{A} \tag{24}$$

$$\varepsilon = \ln \frac{l}{l_0} \tag{25}$$

$$\sigma_e = \frac{F}{A_0} \tag{26}$$

$$e = \frac{l - l_0}{l_0} \tag{27}$$

where F is the applied force, A and A_0 are the cross section and the initial cross section, l and l_0 are the length and the initial length. The true strain is related to the engineer strain as follows:

$$\varepsilon = \ln (1 + e) \tag{28}$$

Taking also conservation of volume into account it is also possible to compute true stress

$$\sigma = \sigma_e \exp (\varepsilon) \tag{29}$$

The data from tensile tests is only useful before necking occurs. The critical condition for necking can be described with the Considere criterion equation 30 (see also [11]).

$$\frac{d\sigma}{d\varepsilon} = \sigma \tag{30}$$

During tensile tests, the stress at 0.2% plastic strain $R_{p0.2}$ and the tensile strength R_m are evaluated automatically. The stress at a plastic strain of 0.01% $R_{p0.01}$ is also calculated. The values of $R_{p0.01}$ and $R_{p0.2}$ can be determined by intersecting the flow curves with a line parallel to the elastic response (see figure 29). In case of the cold rolled sample, the tensile stress R_m is used instead of the yield stress, since buckling during the clamping of the sample makes the stress-strain curve useless.

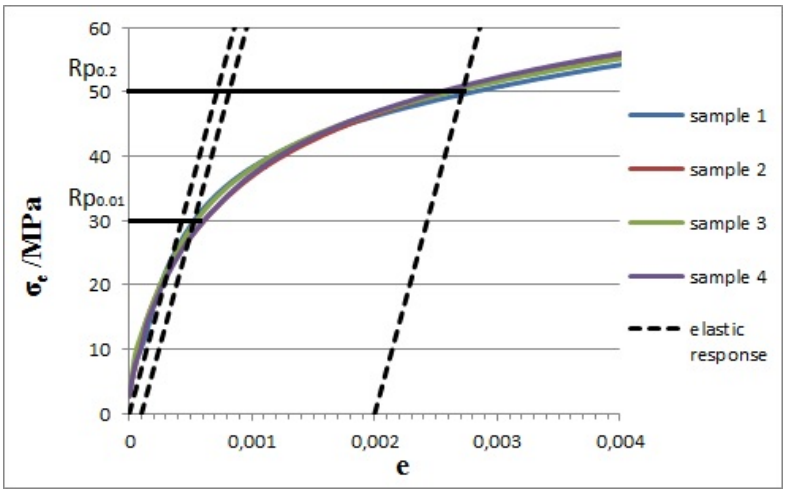

Figure 29: Flow curves at very low strain showing the calculation/graphical estimation of $R_{p0.01}$ and $R_{p0.2}$

Since rectangular samples are used, deformation zone is not restricted to the free clamping length L^f(see figure 30). Especially at high strains, deformation of samples also occurs in between of the clamps, where thinning of samples indicates sample elongation (see sample 1 and 3). As extensometer is used at low strains, the measurement of yield stress is not effected by slip.

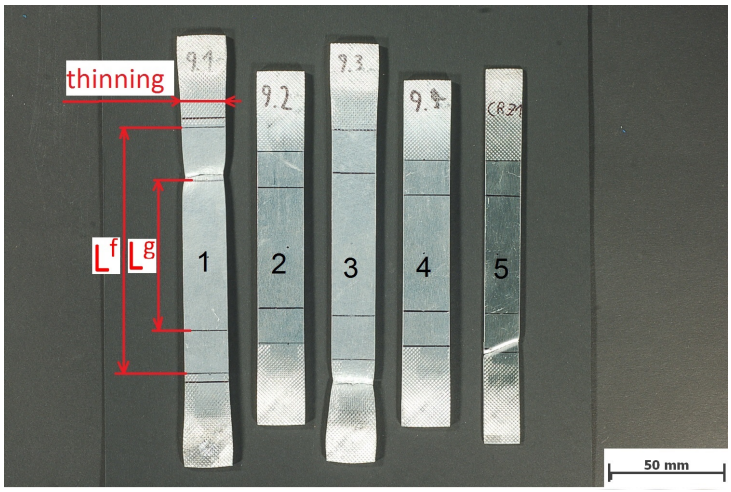

Figure 30: Samples after tensile test

To make stress-strain curves comparable to flow curves of compression tests, the true stress and the true strain is used. The transformation is shown in equation 28 and 29. The calculation of true stress-strain curves is done in three different ways: Firstly, the strain is calculated based on the length measurement of the extensometer. This is accurate, but only available at strains up to 0.05. Secondly, the strain is calculated based on the measurement of the cross head movement, where the initial free clamping length $L_0^f = 80mm$ is used for the calculation. Thirdly, the additional deformation in between of the clamps is taken into account and an effective length of deformation (L_0^{effect}=100mm) is used to calculate the strain.

5.3. Annealing Tests

After cold deformation, the samples are annealed to investigate recovery and recrystallization. Therefore, two different devices are used: oven and Gleeble. On the one hand, oven annealing is used to get a basic idea about the kinetics of recovery and recrystallization at different temperatures. For this preliminary test cold rolled samples (identified by CR) are used. After annealing, all samples are water quenched. As shown in a previous work [6], recrystallization of cold rolled samples may be finished already after annealing for 2 minutes at 350°C. Nevertheless, test at 350°C for 10 minutes is performed to have a fully recrystallized reference state for hardness and micrograph investigations.
Since oven annealing is not practical for short time annealing treatments, shorter annealing treatments are performed in the Gleeble® machine directly after cold deformation,

Table 2: Annealing treatment cold rolled samples

sample	temperature/°C	time/min
CR1	150	2
CR2	150	10
CR3	200	2
CR4	200	10
CR5	250	2
CR6	250	10
CR7	300	2
CR8	300	10
CR11,CR12	350	10

followed by quenching. The same tools are used for deformation and the resistant heating of the samples. Temperature is measured with a thermocouple type J, welded at the center of sample edge. Figure 31 shows the remained pins of the thermocouple.

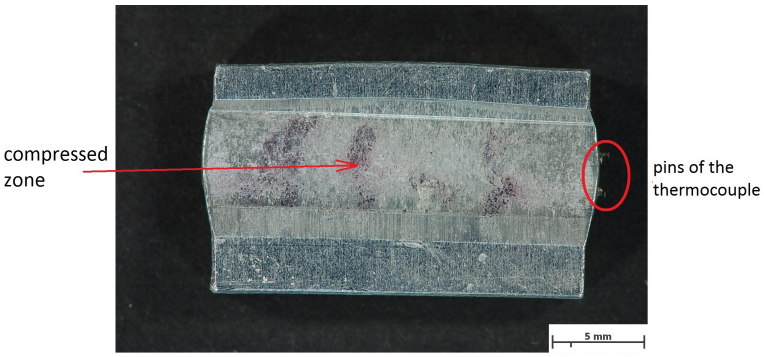

Figure 31: A plane strain deformed sample showing remaining pins of the thermocouple

The cold deformation and heat treatment is shown in figure 32. In the standard tests only holding temperature and time are changed. Parameters, which are the same for every standard test, are shown in table 3.

Table 3: Parameter for standard test

parameter	value
material	hot rolled sheet material
strain	0.5
strainrate	0.01
heating rate	20K/s
colling	water quenched

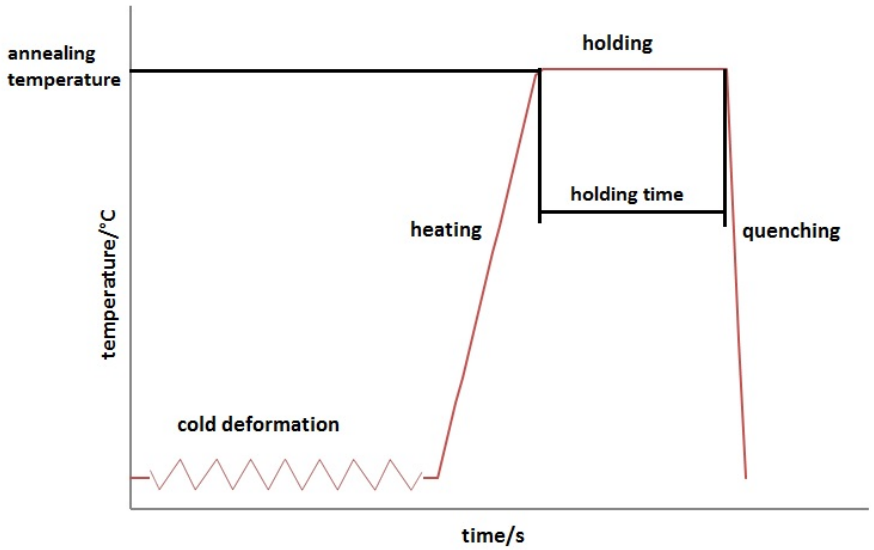

Figure 32: Thermomechanical treatment

Table 4: Holding conditions in standard tests

temperature\time	0s	15s	30s	60s	120s	300s
200°C	-	-	-	-	ps73	-
250°C	ps64	-	ps62	ps71	ps63	ps72
300°C	ps59,ps60	-	ps61	-	ps65,ps75	-
350°C	ps54	ps57	ps53	ps55	-	-

The abbreviations in table 4 refer to sample names: ps meaning plane strain deformed followed by the identification number. In order to get information about the influence of the different parameters on the recrystallization (strain, strain rate), additional experiments are performed. The parameters are shown in table 5. Each experiment differs only in one parameter compared to the experiments in the standard tests. The initials HG refer to a homogenized material at 530°C for 20 hours.

Table 5: Parameters extra tests

sample	strain	strain rate	annealing temp/°C	holding time/s	material
ps66	0.5	0.1	300	30	standard
ps67	0.5	1	300	30	standard
ps76	0.3	0.01	250	120	standard
ps74	0.8	0.01	250	120	standard
ps_HG79	0.5	0.01	250	120	homogenized
ps_HG80	0.5	0.01	300	120	homogenized

Many observations made after resistant heating experiments at the Gleeble show no clear dependency of recrystallization with respect to the annealing temperature. Therefore, cold deformed plane strain samples are also annealed in the oven to check recrystallization temperature. At different temperatures, a 2 minute short time annealing is performed to get the recrystallization temperature for an industrial process and a 60 minute time annealing is performed to get the recrystallization temperature for longer annealings (see table 6).

Table 6: Annealing plane strain samples in oven

sample	temperature/°C	time/min
ps69a	200	2
ps69b	200	60
ps70a	250	2
ps70b	250	60
ps78a	300	2
ps77b	300	60
ps77a	350	2
ps78b	350	60

If the names of two samples only differ in a and b, it means that one plane strain sample is cut in the middle to make two different annealing treatments. Thereby the influence of fluctuation of strain may be reduced.

6. Numerical Investigation of the Deformation

Plane strain compression tests, used in this work to cold deform the samples, lead to a non-uniform strain distribution over the sample cross section. As the stored energy and the formation of nuclei for recrystallization mainly depend on the local strain, it is essential to determine the local strain distribution. The standard tool for calculating plastic strain is the finite element method FEM. In a FE model, the geometry of the work-piece is defined, material properties are assigned to it, and boundary conditions are applied.

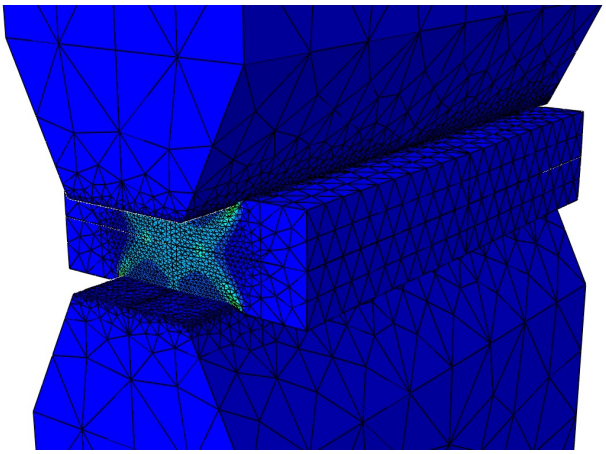

Figure 33: 3D model of plane strain test

Figure 33 shows a three dimensional model of a plane strain compression test of a small sample cut from a hot rolled sheet. Thanks to the plane strain conditions, the model can be reduced to 2 dimensions (figure 34). Here the plane strain tools are modelled as rigid bodies and drawn as lines. Figure 34a and 34b show a model with the full cross section. This model is used to simulate imperfections in the plane strain tests. In figure 34a there is an offset between the upper and the lower anvil. The reverence points RP, which indicate the center of each tool, are not aligned with the center line of the sample: the lower anvil is shifted 0.2mm to the right. In figure 34b, a model with non-uniform friction distribution is shown. If a symmetric case is considered, the model in figure 34c is the best choice. Simulations run more stable and faster if only a quarter of the whole sample is modelled and symmetric boundary conditions are applied.

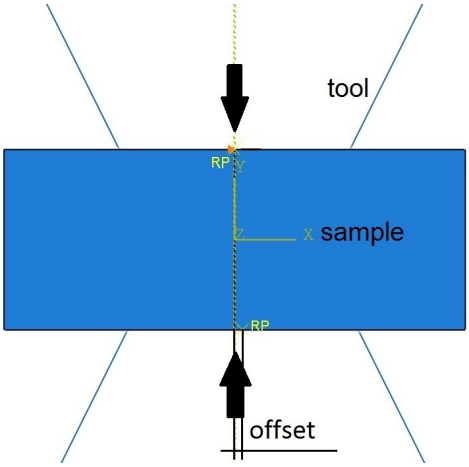

(a) Tool offset

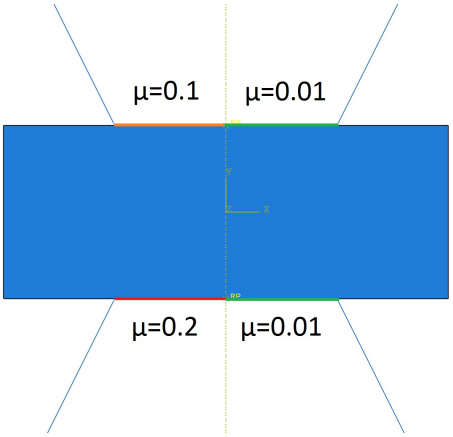

(b) Unsymmetrical friction

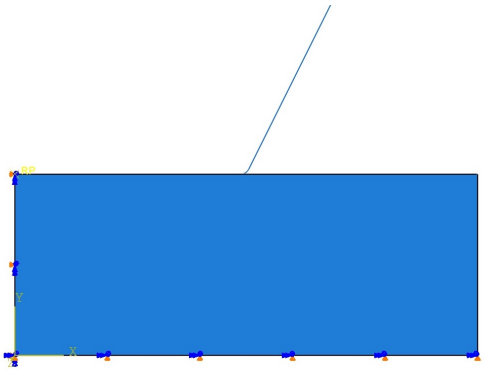

(c) Symmetric case. Quarter FE-model

Figure 34: 2-dimensional FE-model

The mechanical properties of aluminium are used in the simulation. As plastic deformation is considered, a flow curve is needed beside Young's modules E and Poisson's ratio ν. The Johnson-Cook material model (see equation 31) turned out to fit flow curves, previously determined in compression tests. As only cold deformation is considered, the strain-rate sensitivity and the temperature dependency are omitted here. The model coefficients A, B and c are extracted from flow curves which are shown in section 9.

$$\sigma = A + B\varepsilon^c \tag{31}$$

- Young's modules E=70GPa
- Poisson's ratio ν=0.34
- A=30MPa
- B=170MPa
- c=0.28

7. Sample Preparation

Samples are embedded with a cold embedding resin, to avoid any thermal effect. Plane strain samples are investigated in the rolling direction RD (see figure 35b). To get the optimal cross section, samples are cut in the middle (figure 35a).

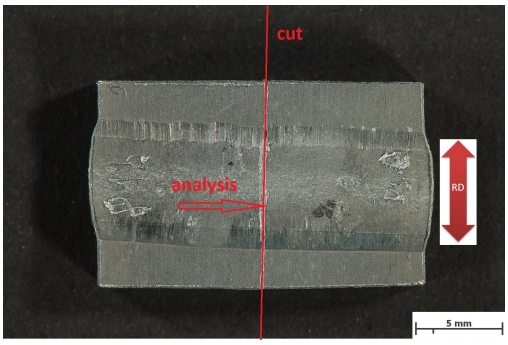

(a) Plane strain sample cutted in the middle

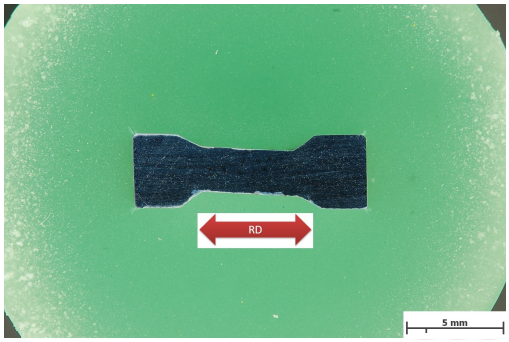

(b) Cross section after embedding

Figure 35: Preparation of plane strain samples for metallography

After embedding, samples are ground with 500 grade SiC paper with semi-automatic grinding machine to get a plane surface. After that, step by step grade is increased (800, 1200, 2400, (4000)). Every paper is used for 2 minutes, whereas the applied force is 15 N/sample. After grinding, preparation continues with diamond polishing (3μm and 1μm). Polishing should be limited to short times, to avoid breakage of intermetallics and holes formation (figure 36). Two minutes of diamond polishing for each of the two steps and a force of 15N seem to be a good compromise.

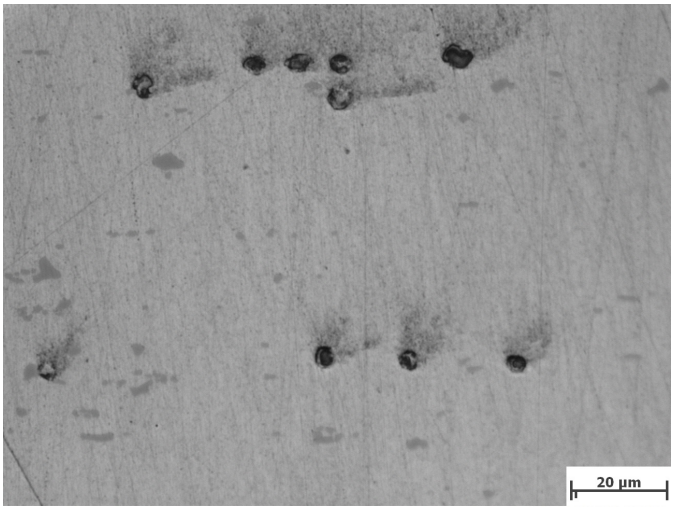

Figure 36: Holes after 1μm polishing for long time

After diamond polishing, fine scratches are removed with oxide polishing (acidic OP-S suspension). The chemical attack is very helpful for soft materials. A sequence of two or three times 2 minutes, each with 15N force is enough. At the end of each 2 minutes session, polishing plate should be cleaned with a plenty of water to avoid crystallization of the suspension. In case of sample preparation for EBSD, vibration polishing is used with a neutral oxide suspension OP-AN for 12 hours. The same procedure is used for some of the light microscope samples to obtain better pictures. To see the grain structure in light optical microscopy, etching is necessary after OP-S or vibration polishing. Electrochemical etching is done using a Struers LectroPol electrolytic etching unit. The composition of the solution and parameters of electrolytic polishing are shown in table 7. A closed electrical circle is necessary for electrochemical etching. Therefore, a small hole is drilled into the sample mould opposite to the polished section, to contact the sample with a nail during electrochemical etching process. Drilling is done before grinding to avoid scratches during the drilling process. Electrochemical etching in combination with polarized light microscopy results in good grain contrast.

Table 7: Parameter for Barker etching

destillated water	200ml
tetrafluoroboric acid 35%	5g
temperature	25°C
voltage	25V
flow rate	20
cross section	0.5 cm^2
time	60s to 120s

8. Sample Analysis

The samples are analysed with different methods at different length scales. On the one hand hardness measurements are used to investigate the macroscopic hardening and softening of the samples. Further, light microscopic pictures reveal the grain structure of cold deformed as well as of recrystallized samples. Finally EBSD measurements show substructure at a sub-micron scale.

8.1. Hardness Measurement

Hardness measurement is a technological method to determine material properties. In this thesis Vickers hardness tests are used to describe the hardening and the softening phenomena after cold deformation and annealing. A pyramidal indenter is pressed into the material with a certain load F for 15s (standard condition). The point angle of the indenter is 136°. The hardness value is calculated as follows:

$$Q = \frac{d^2}{2\sin(136°/2)} \approx \frac{d^2}{1.8544} \tag{32}$$

where Q and d are the area and the average diameter of the indentation, respectively. Finally the Vickers hardness HV is:

$$HV = \frac{F}{Q} \approx \frac{1.8544F}{d^2} \left[\frac{kp}{mm^2}\right] \tag{33}$$

where F is the load given in kilopond kp. Vickers hardness is reported as a combination of the hardness value, loading force and loading time, for example 60HV5/20, where 60 is the hardness value coming from equation 33, 5 is the load in kp and 20 is the time in seconds. Declaration of time is only necessary in case of non-standard tests. Hardness measurements with different loads give similar hardness values. During experiments differences of hardness values are obtained. For example, the automatic operated measurement of HV0.1 of the hot rolled sample yields a value of 36.1HV0.1, which is significant higher than the manually measured 32.9HV5 and 33.7HV1. There are similar differences in the hardness measurements of cold rolled samples, where 65.9HV0.1 is obtained from the automatic and 61.6HV5 from the manually operated machine. The loading force is chosen as a function of the material hardness (small force for soft material). In order to get more physical units, equation 33 can be multiplied by standard gravity 9.81 to get hardness values in MPa.

$$HV = \frac{F}{A} \approx \frac{18.17F}{d^2}[MPa] \tag{34}$$

In this thesis, hardness measurement is used in two different ways. Firstly, to determine the average softening of cold rolled samples after oven annealing. Therefore, a manually operated hardness testing machine is used. Secondly, an automatically operated hardness testing machine is used to measure the spatial distribution of hardening of the plane strain samples. In addition, a correlation of the hardness with the yield stress is used to describe spatial distribution of the flow stress. The relation between hardness and yield stress depends on the material. The relation $HV = 3\sigma_{UTS}$ is used for carbon steels, where HV is the Vickers hardness in MPa and σ_{UTS} is the tensile strength [12]. In general, the relationship between HV and σ is a function of the thermo-mechanical pre-treatment. For example, the relation of hardness and yield stress HV/σ_y for cold worked copper is 3.70, whereas for annealed copper it is 6.76 [12]. Especially for soft materials, like annealed aluminium, a constant relationship between the hardness and the yield stress is not very accurate. The reason for that is that hardness measurements cause additional work hardening in the vicinity of the indentation. The additional work hardening is high for annealed material, but it is low for cold worked material. For that reason a novel method was developed, which takes the hardening of the material during hardness measurement into account. It means that the additional hardening during measurement depends on the slope of the flow curve. This is valid for uniaxial load, and is assumed to be similar for strain hardening during hardness measurement. Figure 37 shows slope of the flow curve decreasing with increasing strain.

To estimate hardening at a certain value of pre-strain, the tangent of the flow curve is calculated based on the material model (equation 31). To avoid infinite slope at zero strain and to make the method applicable for functions which are not possible to

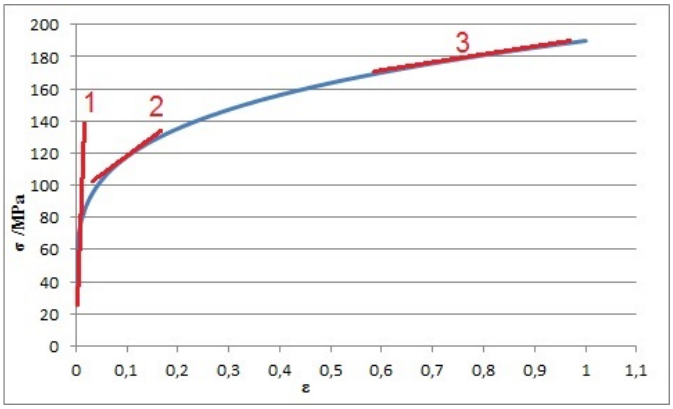

Figure 37: Hardening at different strains

differentiate, the secant is calculated instead of the tangent. For the calculation of the secant the strain increment $\Delta\varepsilon = 0.01$ is used.

$$\frac{d\sigma}{d\varepsilon} \cong \frac{\Delta\sigma}{\Delta\varepsilon} = \frac{A + B\left[(\frac{\sigma - A}{B})^{\frac{1}{c}} + \Delta\varepsilon\right]^{c} - \sigma}{\Delta\varepsilon} \tag{35}$$

Table 8 shows the measured yield stress σ_y and hardness HV0.1. The last column shows the slope after equation 35.

Table 8: Hardness-stress relationship of tensile samples

σ_y/MPa	HV0.1/MPa	$\frac{HV0{,}1}{\sigma_y}$	$\frac{d\sigma}{d\varepsilon}$/MPa
29	354	11.8	4718
70	390	5.58	1325
100	418	4.18	405
180	646	3.59	50

Figure 38 illustrates the relation between HV/σ_y and the strain hardening $\frac{d\sigma}{d\varepsilon}$. A quadratic regression is made (equation 36), and used later to determine the local flow stress from hardness measurements. Since equation 36 is non-linear with respect to the stress, it has to be solved iteratively using a starting value for the stress. Mathematically, there is more than one possible solution. To obtain the physically correct solution, a high starting value (for example 150 MPa) has to be used.

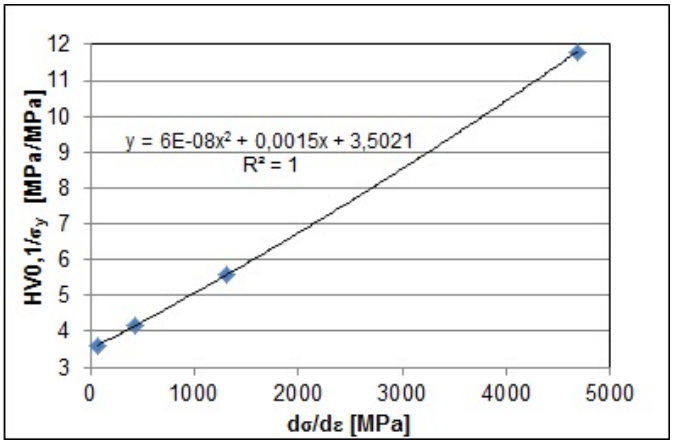

Figure 38: hardness/stress-relation as function of strain hardening

$$\frac{HV0.1}{\sigma} = 6 \cdot 10^{-8} \left(\frac{d\sigma}{d\varepsilon}\right)^2 + 0,0015 \left(\frac{d\sigma}{d\varepsilon}\right) + 3.5021 \tag{36}$$

After determining the local flow stress, it is quite easy to calculate the local strain. Rewriting equation 31 yields:

$$\varepsilon = \left(\frac{\sigma - A}{B}\right)^{\frac{1}{c}} \tag{37}$$

Further, the spatial values of stress can be used to determine the spatial distribution of dislocation density ρ. Therefore equation 7 is rewritten as:

$$\rho = \left(\frac{\sigma - A}{1.138 \cdot 10^{-5}}\right)^2 \tag{38}$$

It is obtained, that $A = \sigma$ when $\rho = 0$.
This equation only holds, if the constant part of equation 7 does not change during processing. This means that flow stress is not changing due to changes in any of the hardening terms: solute, precipitation and grain size hardening. Since hardness measurements after recrystallization of cold rolled samples give nearly the same values as for hot rolled samples, this requirement seems to be fulfilled.

The relationship between the hardness and the stress (equation 36) is determined for the automatic hardness measurement system. Since manual operated system also is used, in which higher loads are applied, another relation was found for higher loads. The relation for manual operated tests reads:

$$\frac{HV1}{\sigma} = 7 \cdot 10^{-8} \left(\frac{d\sigma}{d\varepsilon}\right)^2 + 0,0013 \left(\frac{d\sigma}{d\varepsilon}\right) + 3.3331 \tag{39}$$

8.2. Optical Microscopy

The optical microscope Zeiss Axio Observer.Z1m is used to make micrographs. Two different kinds of images are produced. On the one hand bright field mode is used to observe particles after polishing. It is also used to analyse the grain structure after HF-solution etching. On the other hand, electrochemical etching is used to reveal the grain structure using polarized light mode (parameter for the electrochemical etching are in table 7). Figure 39 shows the difference of bright field mode after HF etching and polarized light mode after electrochemical etching (Barker's reagent).

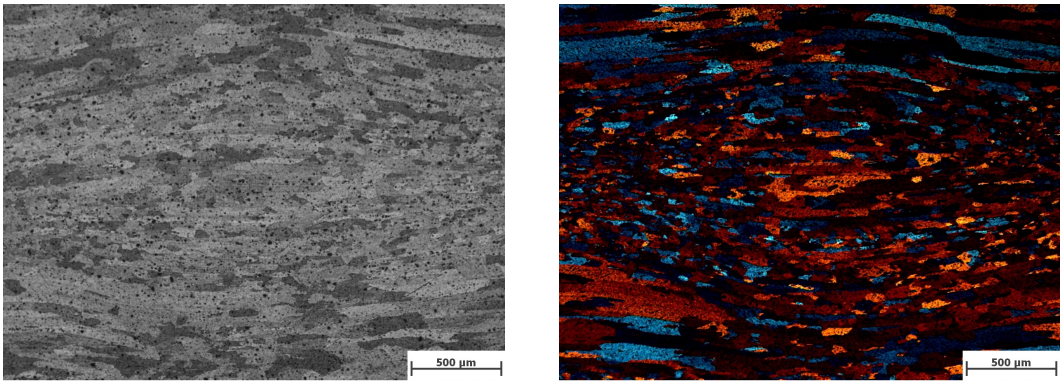

(a) HF etching (b) Barker's etching

Figure 39: Comparison HF etching and Barker etching

The colour of the grains varies with their crystallographic orientation and with the adjustments of the microscope. The adjustment of the quarter-wave plates modifies the colours of the grains (figure 40).

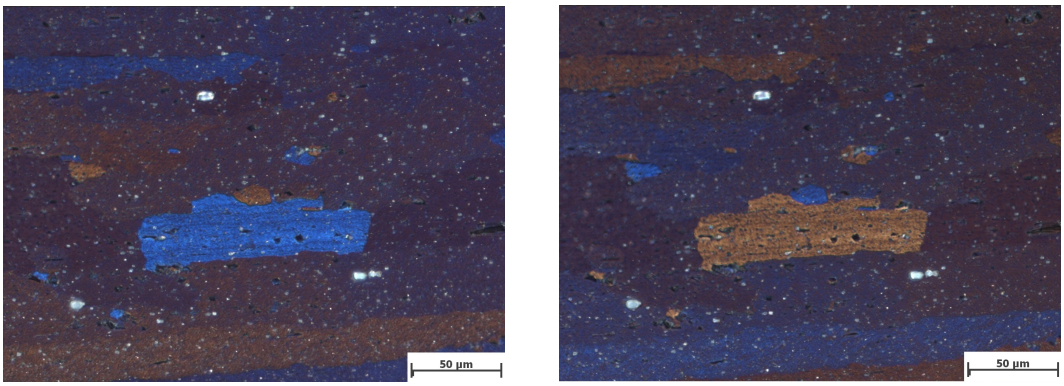

(a) blue grain (b) yellow grain

Figure 40: Variation of colours in polarized light mode after Barker electrochemical etching

8.3. EBSD

Electron backscatter diffraction (EBSD) is used to determine the crystal orientation using a scanning electron microscope (SEM). The orientation data obtained from EBSD measurements can be used to create different maps with the orientation imaging software OIM.

- Inverse pole figure
  An inverse pole figure is a two-dimensional coloured representation of crystal orientation. It can be used for example to identify grains and sub grains.

- Image quality map
  An IQ-map indicates the quality of the Kikuchi pattern for every point. The quality of the patterns depends on the distortion of the crystal lattice. In volumes of high dislocation density the quality is bad and IQ map appears dark. Thus cell walls appear darker than the cell interiors, and cold deformed grains are darker than recrystallized ones.

- Unique colour grain map
  As written in section 2, grains are volumes with a certain misorientation with respect to their neighbourhood. Using a criterion of minimum misorientation required to identify grains, areas are painted in a uniform colour for each single grain. This minimum misorientation is called tolerance angle. In this work, tolerance angle of 11° is used.

- Kernel average misorientation
  In Kernel maps, the average misorientation of one point to its neighbours is calculated. It is possible to compute the misorientation to the nearest neighbours, for the second neighbours, etc. In this work, only the nearest neighbours to each point are considered.

- Grain Reference Orientation Deviation
  In GROD maps the misorientation of every point with respect to the average orientation of the grain to which this point belongs is calculated. The grains follow the same definition like in unique colour grain map. Therefore grain maps are used complementary for interpret a GROD map. GROD maps seem to be a useful tool to identify high misoriented sub grains. These sub grains may act as nucleation sites for recrystallization [1].

Since Barker etching also reveals orientation data, IPF maps and optical micrographs are qualitatively comparable. In figure 41 the inverse pole map (left) is compared with a Barker etching picture (right). A grain of uniform colour obtained with the light microscope is highlighted with thick grain boundaries. The same procedure is done for the IPF map for the same region. The black areas in the IPF map are particles, which are modified be means of confidence index (CI) correction. Although optimizing of Barker etching, information of crystal orientation gets lost using light microscopy.

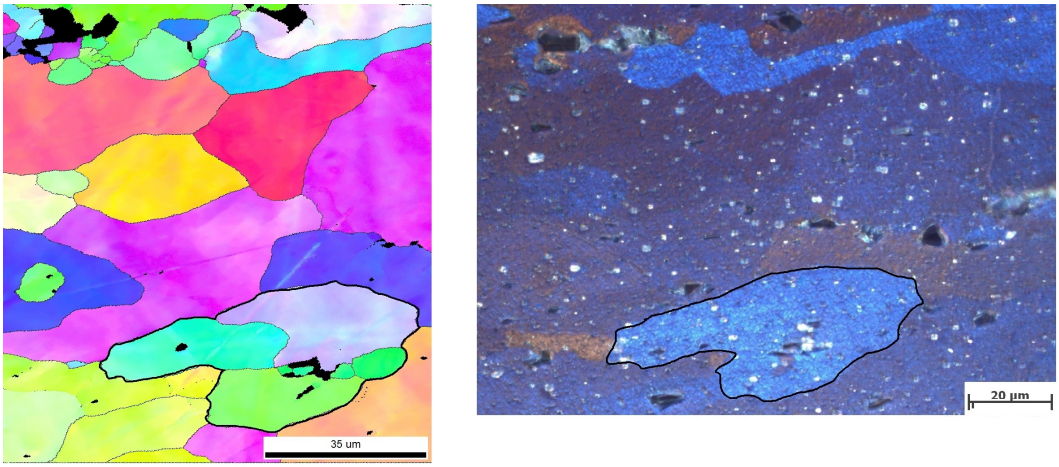

Figure 41: Comparison of EBSD IPF map (left) and light optical microscopy after Barker etching

Part III.
Results and Discussion

Experimental and numerical results are reported in this section. First, the macroscopic plastic properties are shown in the flow curves. Further, the distribution of the local hardening of plane strain samples is discussed in terms of finite element simulation as well as in terms of hardness measurements. Since the nucleation of recrystallization is of general interest, the substructure after cold deformation is analysed with respect to possible nucleation sites. Particle stimulated nucleation phenomena is of special interest and thus, the substructure near hard particles.
Annealing after cold deformation causes softening due to recovery or recrystallization. This softening is observed in the hardness measurements comparison. Furthermore, if recrystallization takes place, changes in microstructure are expected.

9. Flow Curves

9.1. Stress-Strain curves from Tensile Tests

Figure 42 shows the engineering stress-strain curves automatically produced after tensile tests. Here the engineering stresses and strains are plotted. A cross drawn at the end of a curve means that the sample is broken and a circle, that the test was stopped before fracture. The relevant data is collected in table 9. The tensile test of the hot rolled (HR) samples give reproducible results. $R_{p0.01}$ is approximately 30MPa which is remarkable lower than the $R_{p0.2}$ of 50MPa. The tensile stress R_m reached for sample 1 and 3 is approximately 120MPa. Sample 2 and 4 stretched up to an stress of 100MPa and 70MPa, respectively are used for the correlation of hardness and stress (section 8.1, table 8). The curve of sample 1 in figure 42 shows a large drop of stress at 22% strain.

Table 9: Data tensile test

No	material	$R_{p0.01}$ /MPa	$R_{p0.2}$ /MPa	R_m /MPa	fracture
1	HR	30	50	119	yes
2	HR	27	51	100	no
3	HR	29	51	118	yes
4	HR	27	51	70	no
5	CR	-	154(181)	181	yes

At that point, clamping force was increased to avoid slip of the whole sample.

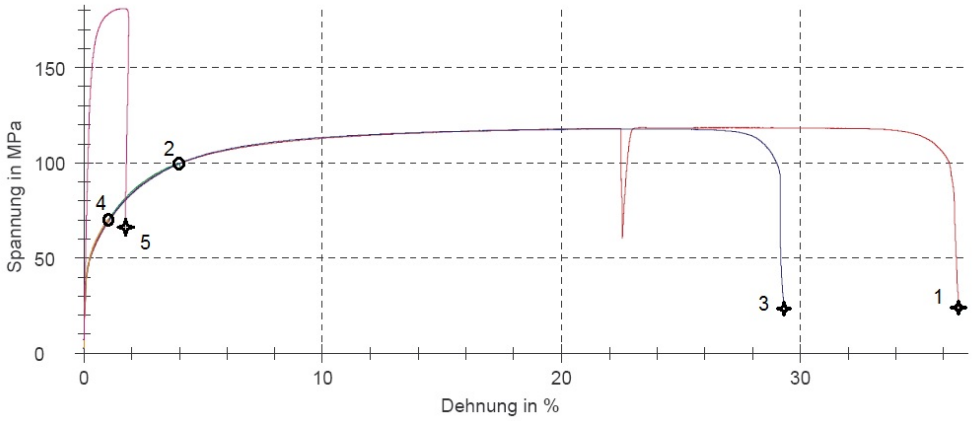

Figure 42: Stress-strain curves at room temperature and strain rate $\dot{\varepsilon} = 0.00025$

In figure 43 the true stress-strain curve of sample 3 is shown. There are two curves based on the measurement of the cross head movement, where different effective sample length (L_0) are used. The curve with L_0=100mm is closer to the curve based on the accurate extensometer. Both curves are compared to flow curves of the plane strain compression tests in the next section.

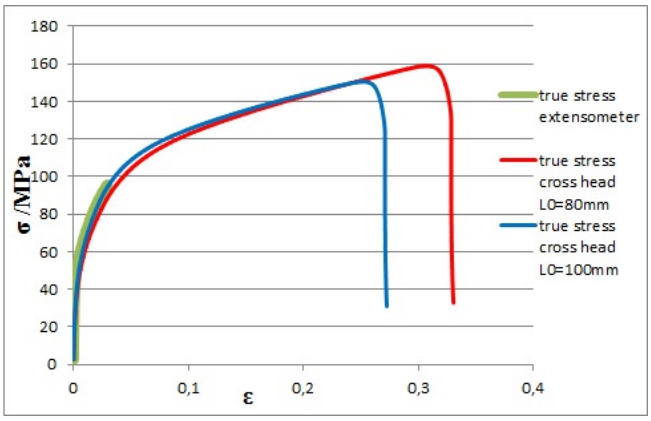

Figure 43: True stress-strain curve of tensile test sample 3

9.2. Flow curves from Plane Strain Tests

Figure 44 shows all curves resulting from standard plane strain tests evaluated with (equation 15 and 16). Plane strain condition is considered, and friction is omitted. These flow curves are used to determine the coefficients of the material model (equation 31). The material model reads:

$$\sigma = 30 + 170\varepsilon^{0.28} \tag{40}$$

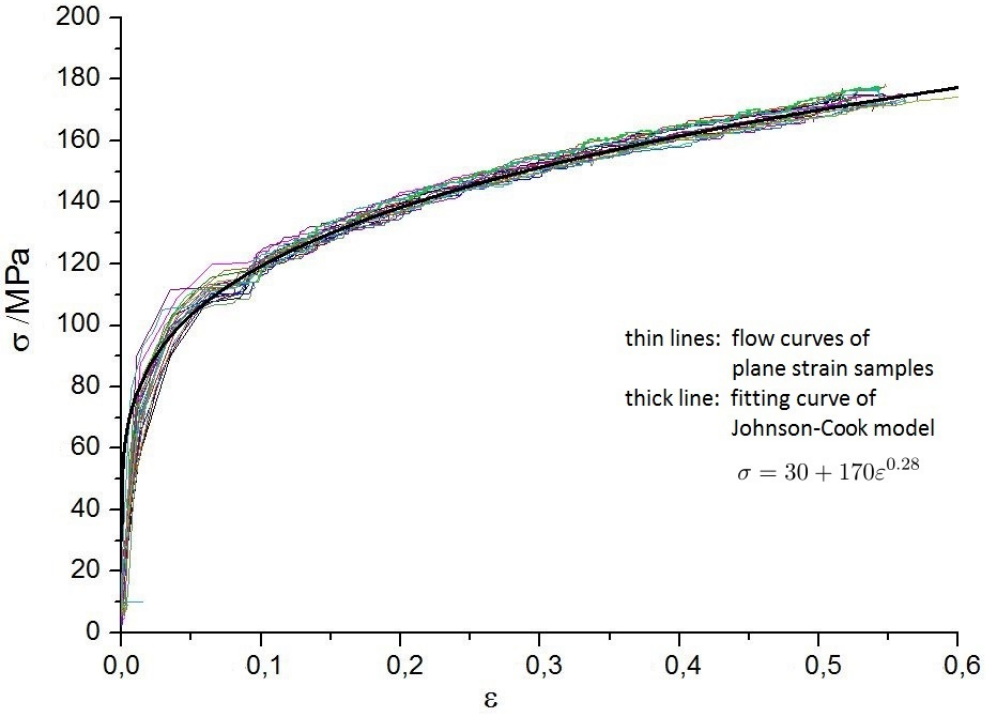

Figure 44: True stress-strain curves and Johnson-Cook model obtained from standard plane strain tests at $\dot{\varepsilon} = 0.01$

In figure 45 flow curves shown in black obtained from compression tests using 5mm wide tools are compared with flow curves obtained from compression tests using 10mm wide tools shown in green and red. The green curves belong to tests using the same lubricant (shown in [10]) as for the 5mm tool, whereas no lubricant is used for the red curves. Comparison of flow curves obtained from experiments using lubricant but different tool sizes yields that the flow stress decreases if the tool width increases. If the flow curves of the 10mm tools are compared, the flow stress increases if no lubricant is used. The tool size as well as the lubricant seem to have an influence on the flow stress. To get more reliable results, more experiments are necessary.

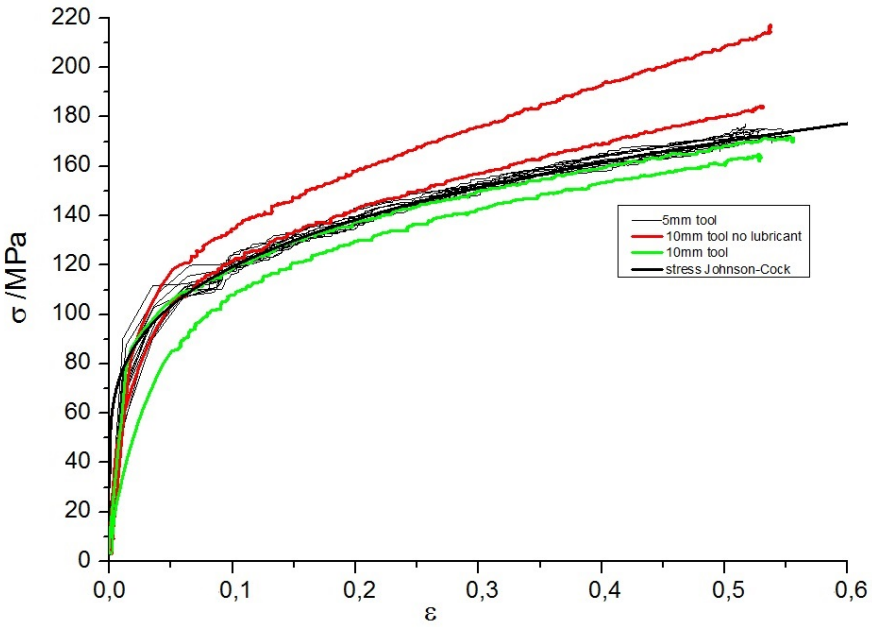

Figure 45: Flow curves as function of tools geometry and friction

In figure 46 flow curves obtained for homogenized samples are compared with hot rolled samples. The same strain rate $0.01s^{-1}$ is used. Since there is no difference, this could indicate, that hot rolled samples are already well annealed.

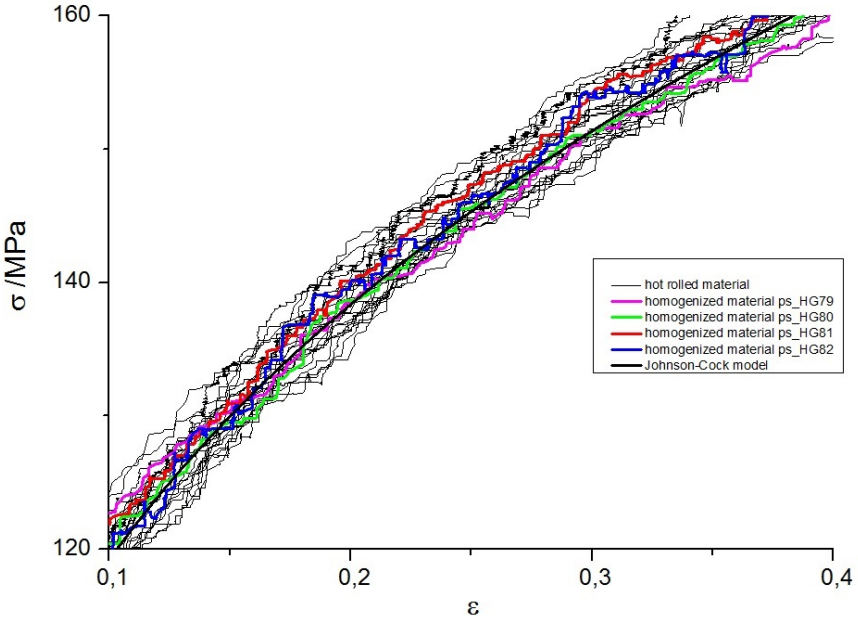

Figure 46: Flow curves of homogenized samples

Figure 47 shows flow curves obtained at different strain rates namely sample deformed at $\dot{\varepsilon} = 0.1$ (flow curve in red) and sample deformed at $\dot{\varepsilon} = 1$ (flow curve in green). Although deformation takes place at room temperature strain rate sensitivity is larger than zero.

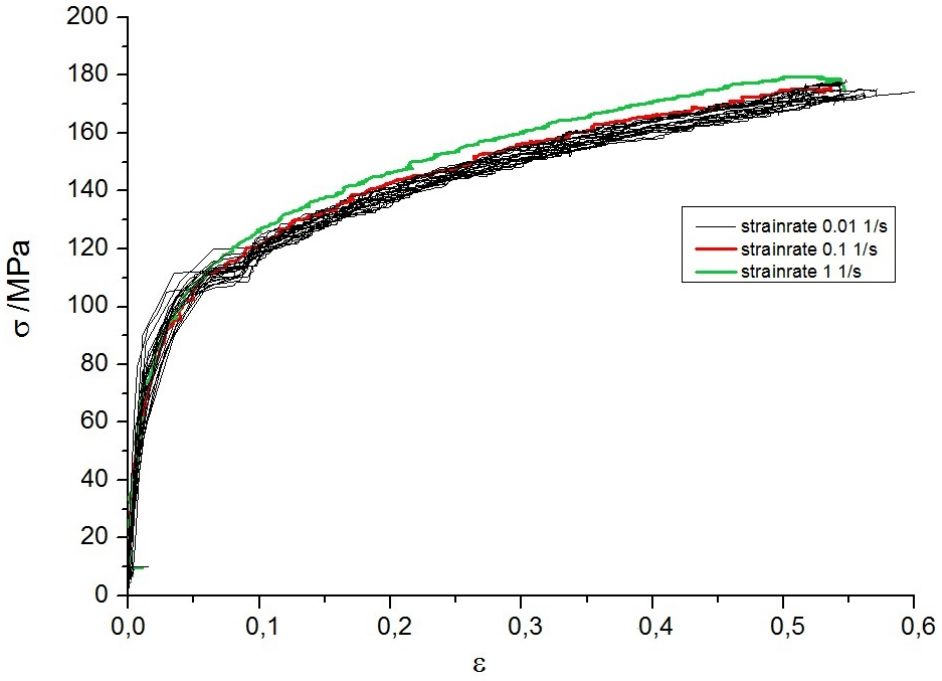

Figure 47: Flow curves at different strain rates

The flow curves obtained from the tensile test 3 are compared with the flow curves from the plane strain tests (figure 48). Flow curves seem to be comparable to some extent, although tensile test give slightly higher stress values, especially at larger strains. Nevertheless tensile test is a good validation of compression tests, since there is no influence of friction. If intensive friction in compression tests takes place, flow stress gets overestimated. Since flow stress is lower in compression tests than in tensile tests, intensive friction can be excluded.

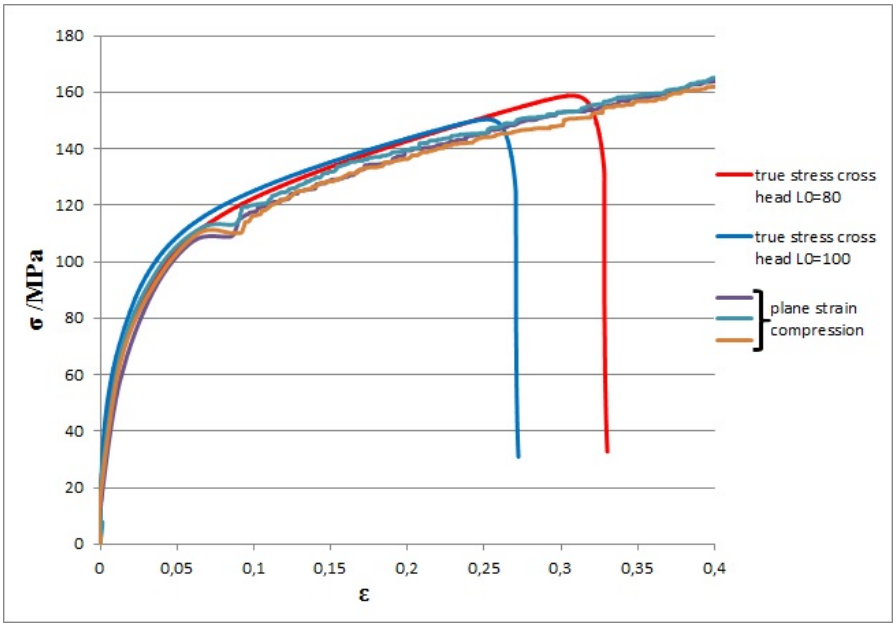

Figure 48: Comparison of true stress-strain curves from tensile test at $\dot{\varepsilon} = 0.00025s^{-1}$ and plane strain tests at $\dot{\varepsilon} = 0.01s^{-1}$, both at room temperature

Necking can also be considered, if the Considere criterion (equation 30) is applied for the Johnson-Cook material model (equation 31). The obtained critical strain for necking is $\varepsilon_{neck} = 0.22$, which is lower than the observed value $\varepsilon = 0.3$ and closer to the value obtained with L_0=100mm $\varepsilon = 0.25$.

10. Spatial Distribution of Strain

The local stored energy given by the plastic strain acts as the driving force for recrystallization. Therefore, evolution of the local strain is essential. The quarter FE-model shown in figure 34c is used to investigate the strain distribution of plane strain samples for ideal symmetric conditions. In figure 49, the solution is mirrored to see the whole cross section for a coefficient of friction of $\mu = 0.05$. Plastic equivalent strain PEEQ is used and the legend shown in figure 49 is valid in all the following figures. It can be observed that in the center of the sample a strain of 0.5 is reached, which equals approximately the value of global strain, while left and right higher strains are shown. Zones of high strain build a typical pattern, which look like a cross. In the center of these deformation crosses, the local strain is approximately 1.

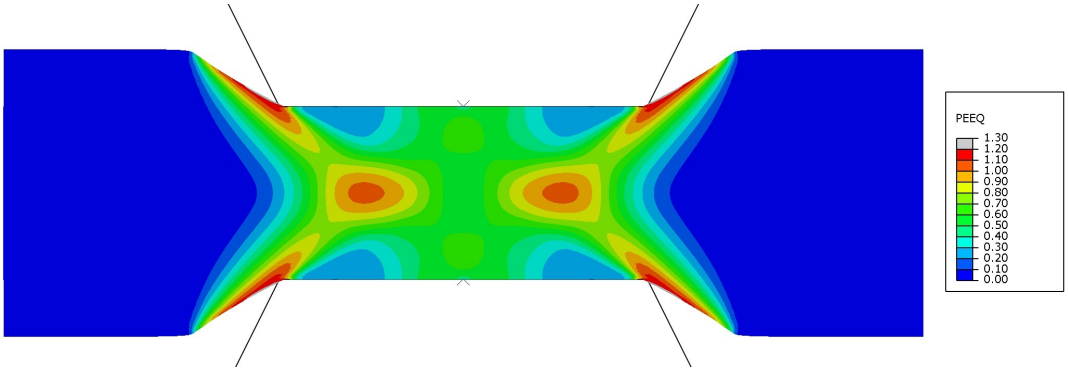

Figure 49: FEM simulation of the plane strain sample showing the strain distribution ($\varepsilon_{global} = 0.5$, coefficient of friction $\mu = 0.05$)

Figure 50 shows spatial PEEQ for different coefficients of friction. It is shown that with increasing friction, the deformation crosses meet in the middle of the sample, meaning that the strain pattern is related to friction. When comparing the strain patterns of the numerical solutions with the strain pattern of the experimental observations, as done later in figure 54, it is possible to estimate the friction in the experiment. Since two clear distinguishable deformation crosses are observed from the experiments, the coefficient of friction must lie below 0.1.

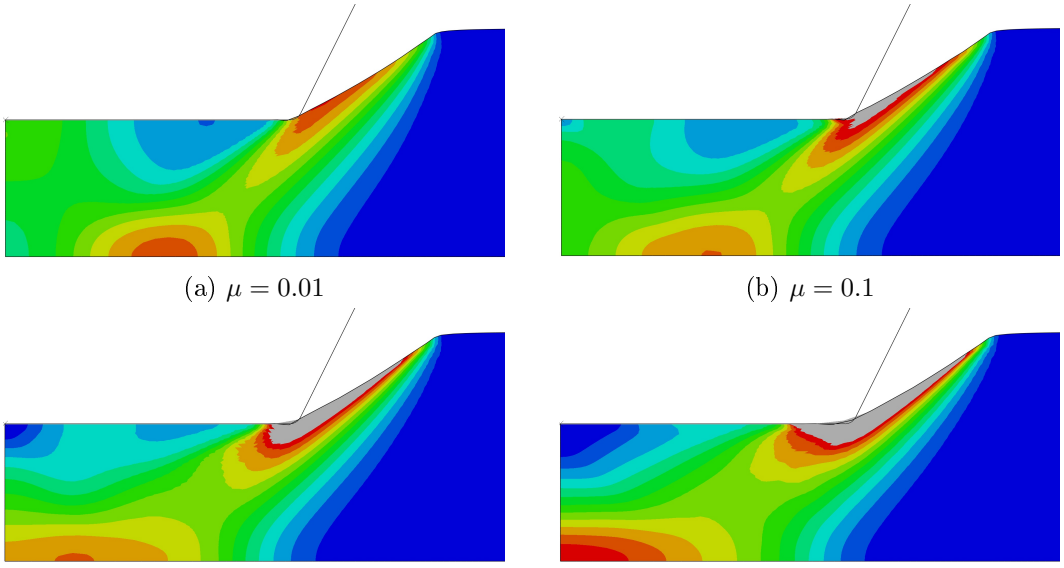

(a) $\mu = 0.01$ (b) $\mu = 0.1$

(c) $\mu = 0.2$ (d) $\mu = 0.3$

Figure 50: FEM simulation of a quarter plane strain sample showing the strain distribution as function of μ (legend of PEEQ in figure 49)

Besides the strain distribution, it is also possible to determine the reaction forces of tools, which are necessary for the deformation. Table 10 shows simulated values of the

tool reaction forces at different coefficients of friction for a 5mm tool and for a 10mm tool after deformation from initial thickness of 3.9mm to 2.35mm. Since the simulation is in 2D, the reaction forces are given for a sample length of unity. If there is no influence of tools geometry, the reaction force of the 10mm should be two times the force of the 5mm tool.

Table 10: Simulated tool reaction force of a plane strain test for a deformation from 3.9 to 2.35mm in the thickness

μ	RF 5mm/$\frac{MN}{m}$	$\frac{RF5}{RF5_{\mu=0}}$	RF 10mm/$\frac{MN}{m}$	$\frac{RF10}{RF10_{\mu=0}}$	$\frac{RF10}{RF5}$
0	1.040	1	2.036	1	1.96
0.01	1.044	1	2.08	1.02	1.99
0.05	1.092	1.05	2.268	1.11	2.08
0.1	1.158	1.11	2.528	1.24	2.18
0.2	1.302	1.25	3.162	1.55	2.43
0.3	1.38	1.33	3.718	1.83	2.69
0.4	1.476	1.42	4.038	1.98	2.74

At zero friction, the reaction force for the 10mm tool is a little bit less than two times the force for the 5mm tool. The reaction force increases by increasing friction, which is implicit predicted from equation 22. The influence of friction $\frac{RF}{RF_{\mu=0}}$ is more marked in case of bigger tools. Using the correction factor of equation 23, the reaction force at a certain coefficient of friction can be reduced to the value of to the reaction force obtained at zero friction (table 11). The values $\frac{RF}{RF_{\mu=0}}$*CF (bold letters) should be equal 1. It can be seen that this correction loses its validity in the case of high friction and big tools due to sticking conditions.

Table 11: Tool reaction force correction

μ	$\frac{RF5}{RF5_{\mu=0}}$	$CF_{w=5,h=2.25}$	$\frac{RF5}{RF5_{\mu=0}}$*CF	$\frac{RF10}{RF10_{\mu=0}}$	$CF_{w=10,h=2.25}$	$\frac{RF10}{RF10_{\mu=0}}$*CF
0	1	1.00	**1.00**	1	1.00	**1.00**
0.01	1	0.99	**0.99**	1.02	0.98	**1.00**
0.05	1.05	0.95	**1.00**	1.11	0.91	**1.02**
0.1	1.11	0.91	**1.01**	1.24	0.83	**1.04**
0.2	1.25	0.83	**1.04**	1.55	0.73	**1.13**
0.3	1.33	0.77	**1.02**	1.83	0.70	**1.28**
0.4	1.42	0.73	**1.03**	1.98	0.77	**1.53**

For a better illustration, the normalised reaction forces of table 10 and table 11 are shown in a graph (figure 51)

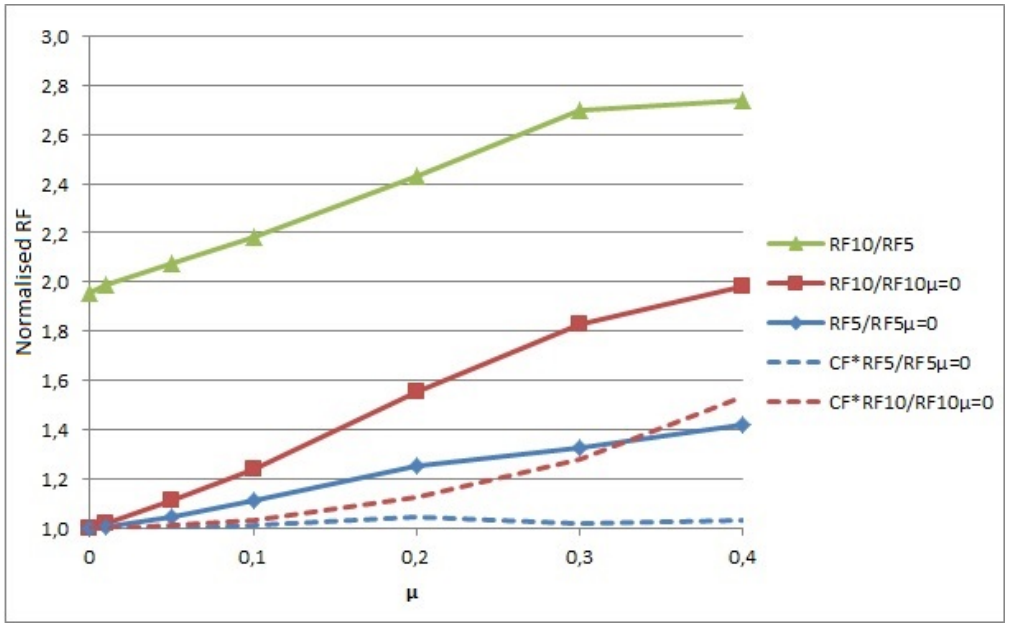

Figure 51: Normalised reaction forces without correction factor (CF) and after application of the correction factor

Up to this point, only symmetric conditions have been considered, meaning that only a quarter of the cross section was simulated. In real experiments, there are some factors, which lead to non-symmetric deformation of plane strain samples. In this thesis, two deviations of plane strain tests are considered, namely offset of tools axis (FE-model figure 34a) and non-uniform friction distribution (FE-model figure 34b). In contrast to the symmetric conditions, the whole cross section has to be simulated. First, a tool offset of 0.2mm is considered. This value is determined based on measurement of a real sample after compression. Figure 52 shows the spatial strain distribution in case of tool offset. The strain is not mirror-symmetric any more, but skew-symmetric. The local strain bottom left and top right is higher than top left and bottom right. The strain in both centers of deformation crosses is equal. In the transition zone between the deformed and the non-deformed material, bending occurs and the non deformed material is tilted with respect to the deformed material.

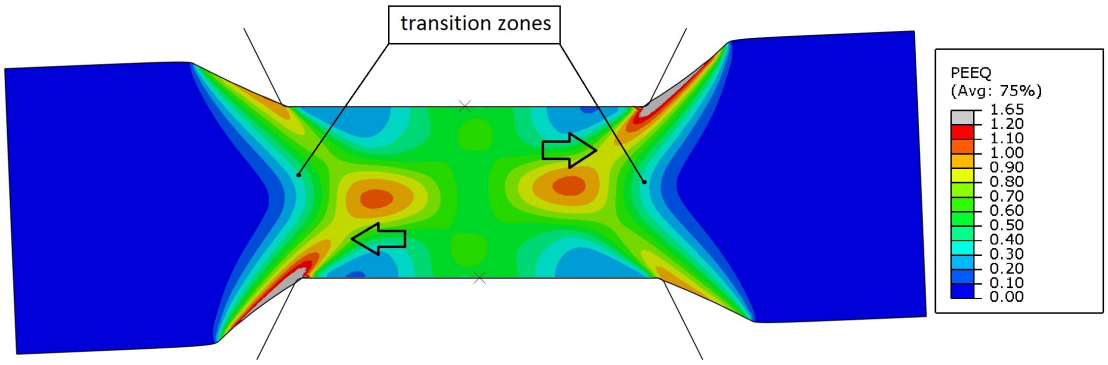

Figure 52: Strain distribution for a tool offset of 0.2mm and a coefficient of friction $\mu = 0.05$

The second case of derivation from ideal behaviour is the non-uniform friction distribution, as is shown in figure 53. Higher friction on the left side of the sample hinders the flow of the material. Therefore the material preferentially flows to the right side. The flow restriction in the left side also causes higher local strain. Because the coefficient of friction on the bottom left is higher than on the top left, tilting occurs in the transition zone.

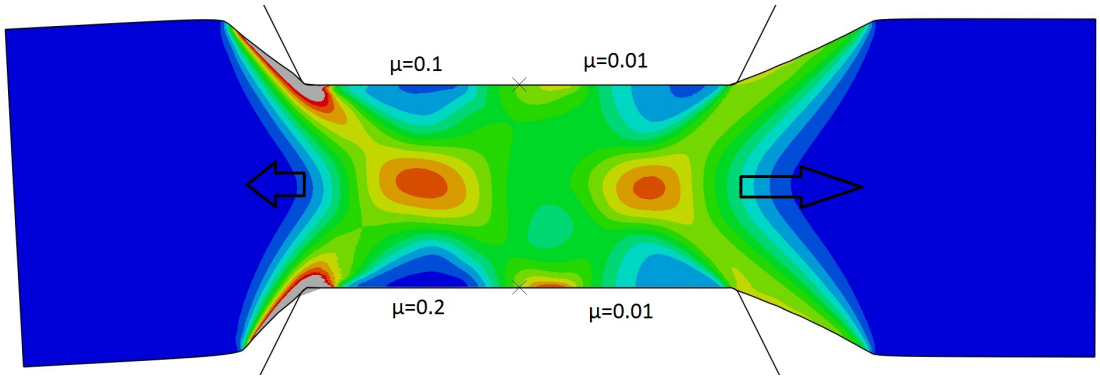

Figure 53: Strain distribution after plane strain under non uniform friction condition

To determine the actual strain distribution in real plane strain samples, hardness measurements are an appropriate method for the case that the precipitate/phase condition of the material is not modified under deformation, such as in this work. Raw hardness mappings without any calculations are useful to get qualitatively the strain distribution. In figure 54 a hardness map is superimposed with the numerical result of strain distribution for $\mu = 0.05$. Since deformation crosses overlap and the position of the deformation crosses is a function of friction (figure 50), $\mu = 0.05$ is a realistic coefficient of friction. Additionally, an offset value of 0.2mm is used.

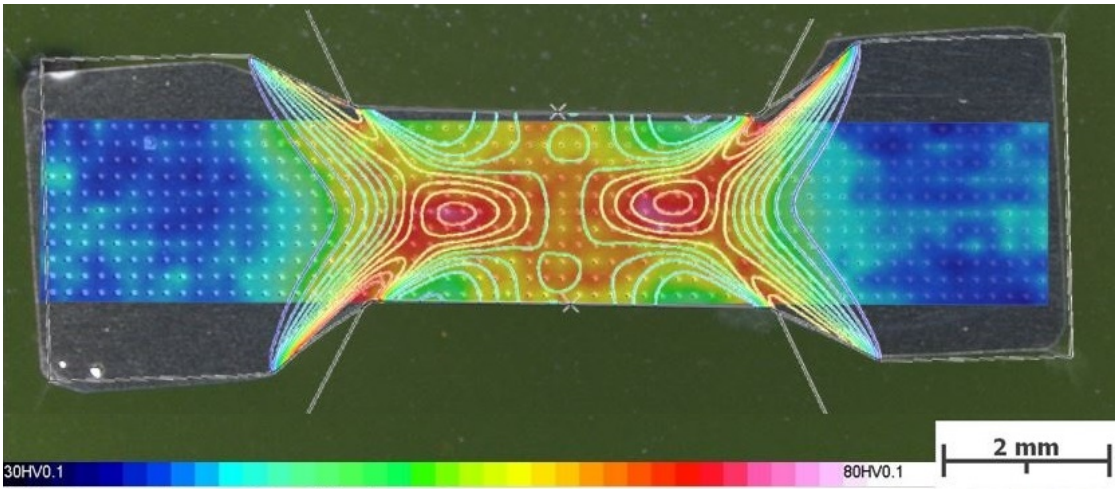

Figure 54: Superposition of experimental hardness map and solution of plastic strain from FE-simulation ($\mu = 0.05$ and tool offset of 0.2mm)

The relation of experimental hardness values and flow stress is obtained by equation 36. Further, the local strain is calculated with equation 37. The stress and the strain are shown in figure 55. Since the strain is very sensitive to the stress at high strains, strain values fluctuate. The maximum strain values obtained with this method are lower than in the numerical solution. There are many sources of errors (hardness measurement, hardness-stress relation, stress-strain relation), which limit the accuracy of this method.

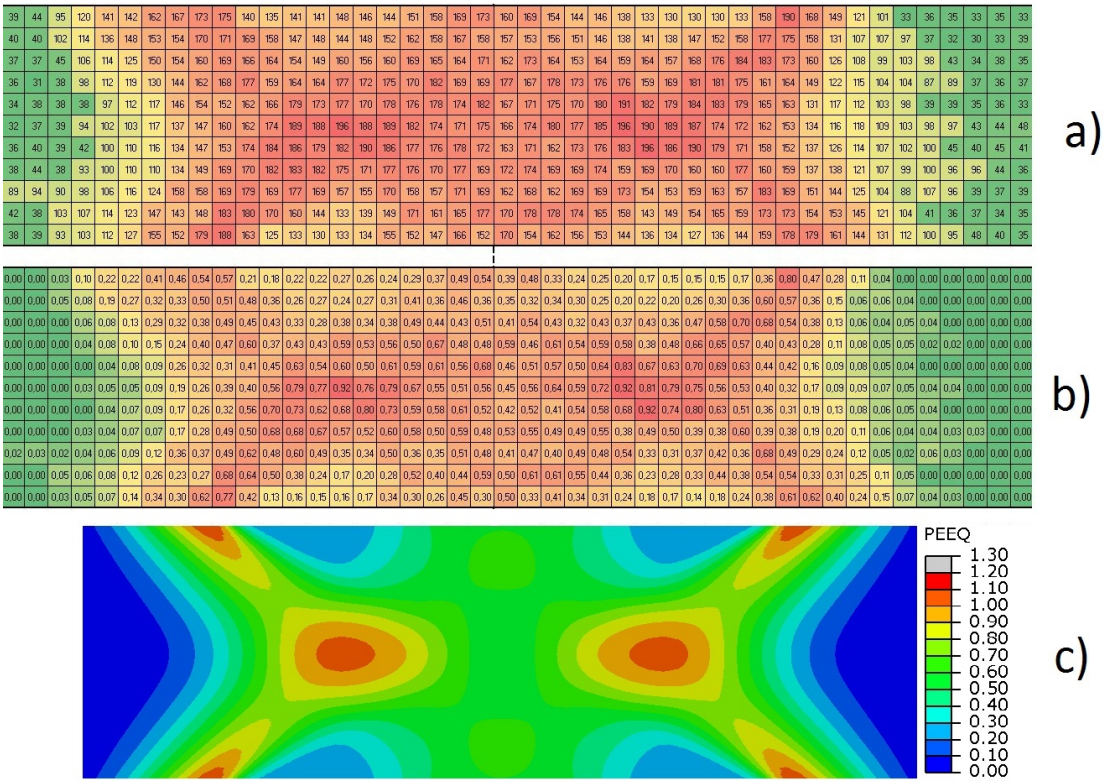

Figure 55: a) Local flow stress (in MPa) b) plastic strain based on hardness mapping c) PEEQ based on FEM

11. Microstructure after Cold Deformation

The evolution of the microstructure after cold deformation before annealing is investigated. Two samples are investigated after plane strain compression: Hot rolled and hot rolled + homogenization

11.1. Hot Rolled Sample after Plane Strain Test at RT

Figure 56 gives an overview of the microstructure of a plane strain cold deformed sample. Due to the plastic deformation during plane strain compression, the grains become more elongated than after hot rolling. The deformation crosses predicted by th FE simulation (figure 49) are also visible in the micrograph.
At higher resolutions (figure 57) some grains show micro shear bands. It is not possible to obtain information about the substructure near particles with LOM but with EBSD measurements.

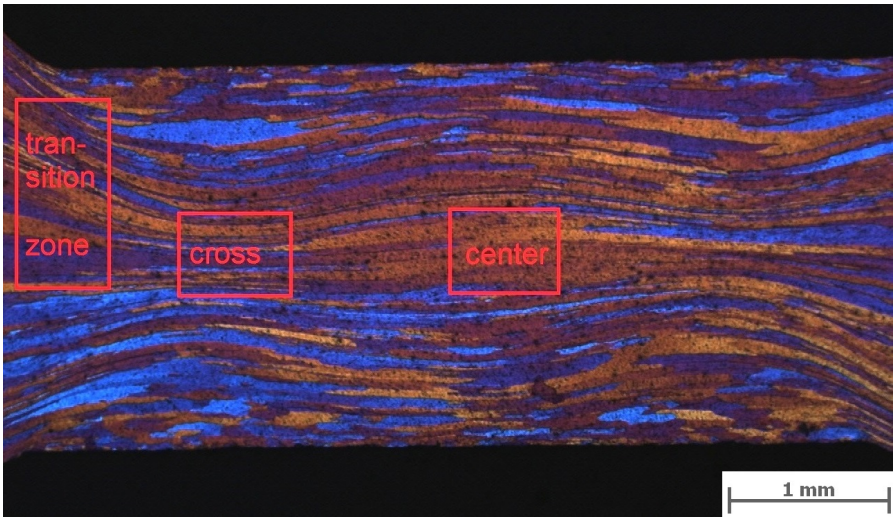

Figure 56: Optical micrograph of cold deformed plane strain sample

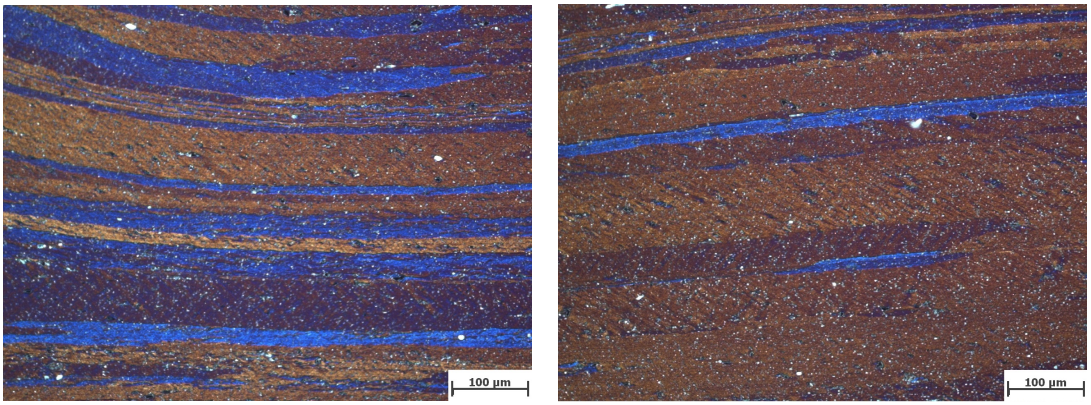

(a) Detail in cross

(b) Detail in center

Figure 57: Details of sample figure 56

Figure 58 gives an overview of the microstructure obtained from EBSD measurements in the center of the cold deformed sample in figure 56. Grain map (tolerance angle 11°) is used to identify grain structure. One interesting point is the appearance of many small grains inside bigger grains. This means, that either there are many boundaries built during deformation or existing before deformation, which exceeded a misorientation of 11°. These boundaries are represented as black lines. The big magenta coloured grain near to the bottom contains many of these boundaries. To get information about long range orientation gradients a Grain Reverence Orientation Deviation (GROD) map is plotted beside grain map. Red pixels are highly misoriented with respect to the average orientation of the grain they belong to. So interpretation of GROD maps is only possible if the definition of a grain is known. Inside of the magenta grain, there are many red

zones in the GROD map, which indicates high misorientations inside of this grain.

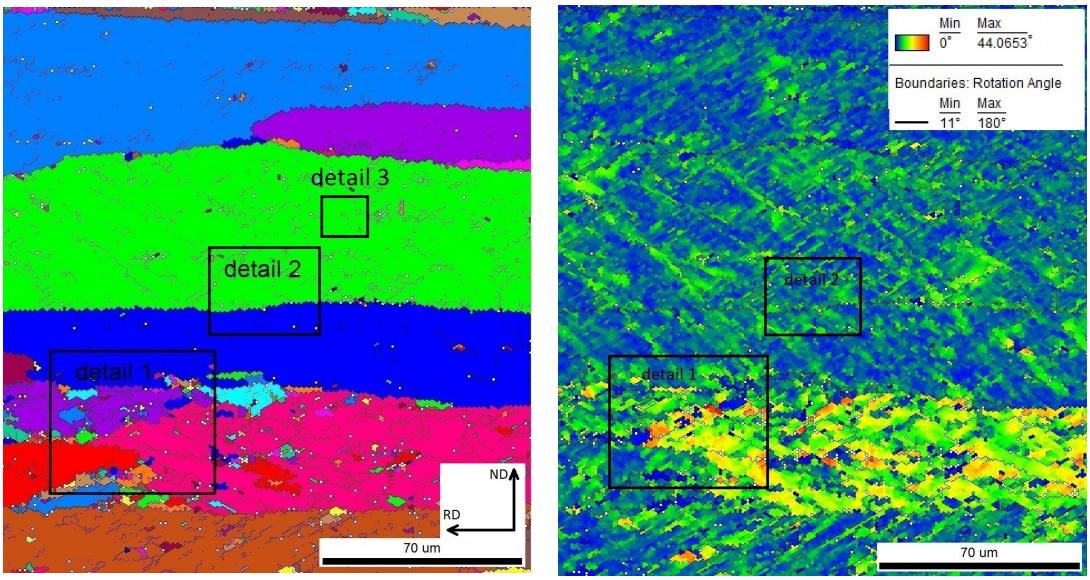

(a) Grain map

(b) GROD map

Figure 58: EBSD maps cold deformed sample figure 56 center region

In detail 1 (figure 59) the substructure and intermetallic particles are clearly visible. There are two different types of particles. AlFeSi-particles appear in a uniform grey scale in image quality (IQ) map (figure 59a), and are compared to iron from EDS. Mg_2Si-particles appear black in IQ-map and blue in EDS map. Big iron particles are expected to act as nucleation sites for recrystallization due to their size. Thus a closer look is taken at some of them.

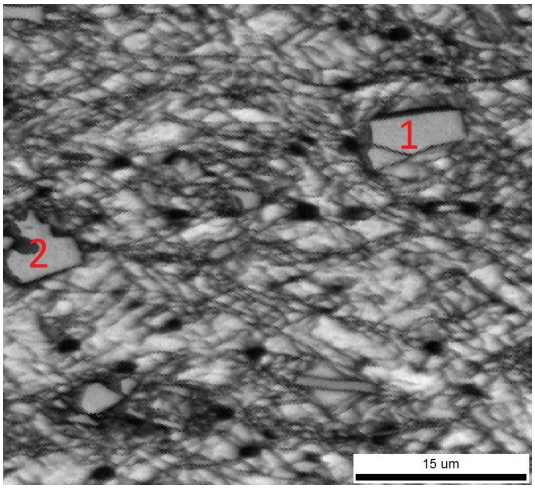

(a) IQ map

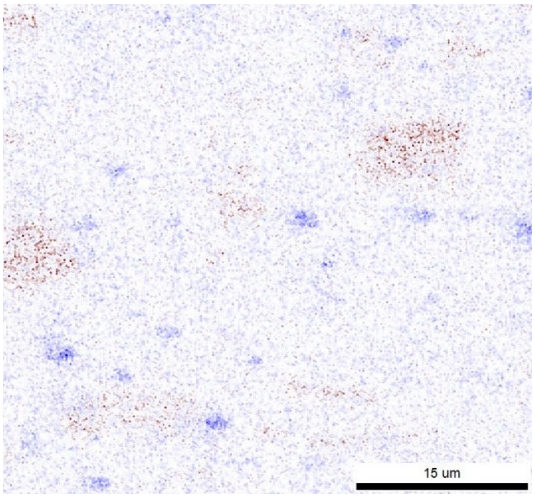

(b) Fe (brown) and Mg (blue) rich particles

Figure 59: Detail 1

Figure 60 shows the two biggest AlFeSi particles of figure 59. Both are displayed in GROD maps to show high misorientations near the particle. In both cases the maximum misorientation is approximately 45°. If nucleation occurs near the particle, the whole orientation spread is offered to the nucleus. So the orientation of nucleus can be considered as random. Since the GROD map only gives scalar values, there is no information about the rotation direction of the crystal. A very simple method to illustrate the rotation direction is to draw a simplified unit cell at some points of the microstructure. Rotation of material seems to be around the transverse direction TD.

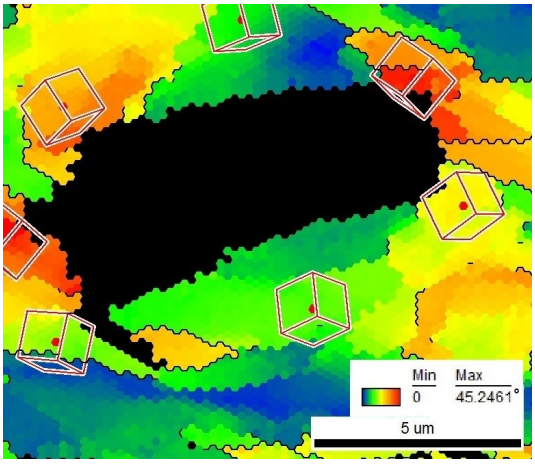

(a) GROD map big particle 1

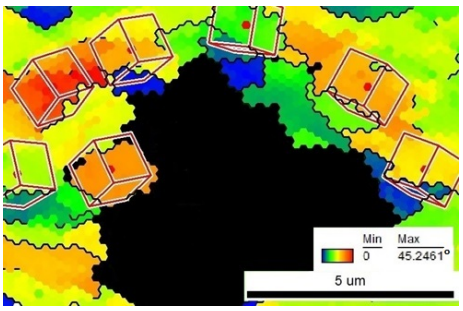

(b) GROD map big particle 2

Figure 60: Big AlFeSi-particles at detail 1

In figure 61 the smaller Mg_2Si particles are shown. Again, the maximum misorientation

is close to 40°. There are boundaries with high misorientations shown as black lines. Some boundaries build closed loops, which are interpreted as grains (figure 61a).

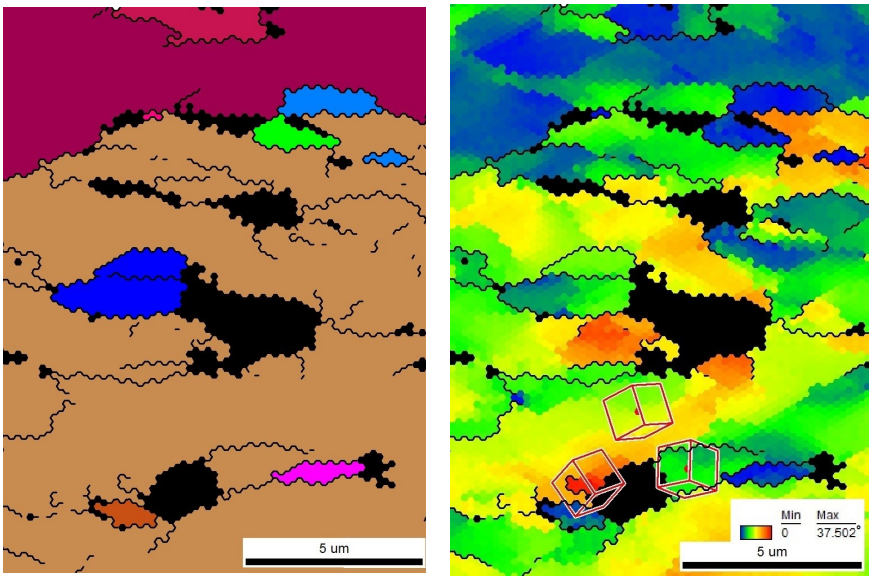

(a) Grain map (b) GROD map

Figure 61: Detail 1: Small MG_2Si-particles at detail 1

A higher resolution measurement of figure 58b (detail 2) is shown in figure 62. IQ and Kernel maps in figure 62a and 62c, respectively have similar patterns. This is due to misorientations which come from geometrically necessary dislocations, which also cause a contrast in the IQ map. The Kernel map is related to IPF and GROD map, because if there is an orientation change at some point, Kernel signal is high. Highly misoriented zones are not only observed near to the particles, but also in bands, aligned diagonally with respect to compression direction (ND in figure 58a).
The maximum misorientation shown in GROD map of detail 2 is smaller than that in detail 1. This is also the case if particles of same size in figure 61 and in figure 62 are compared. The reason may be the crystallographic orientation of the grain with respect to the compression direction. In the GROD map (figure 58b) there is a lot of misorientation in zone of detail 1 and less misorientation in detail 2.

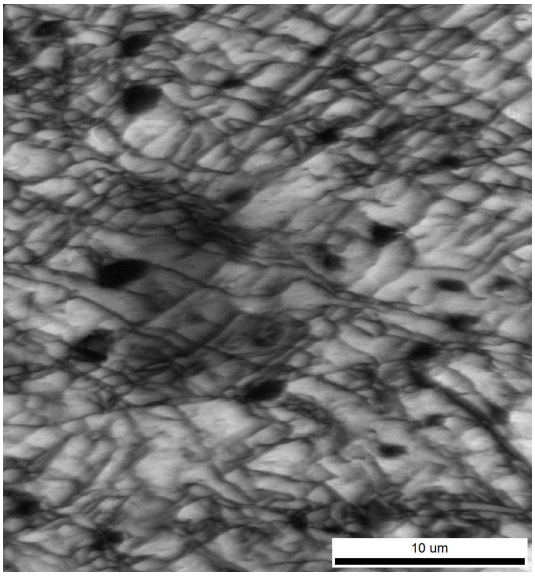

(a) IQ map

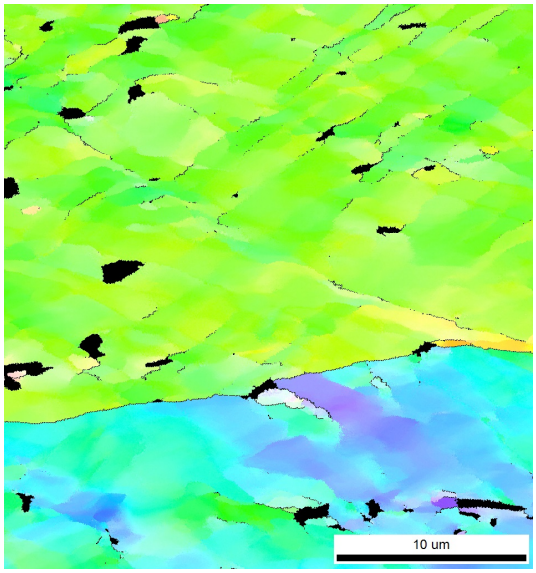

(b) IPF map

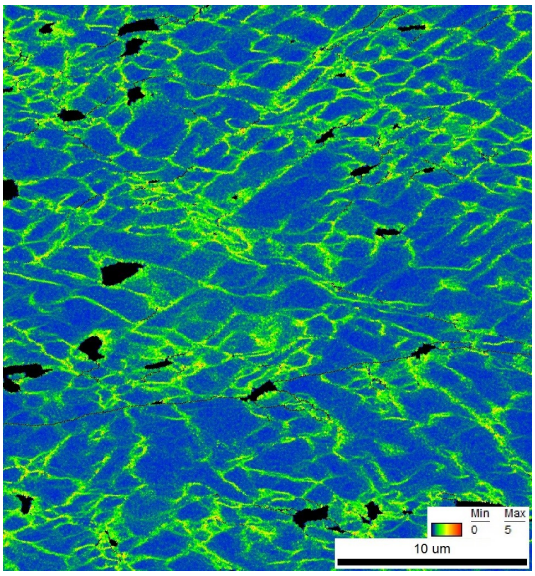

(c) Kernel map

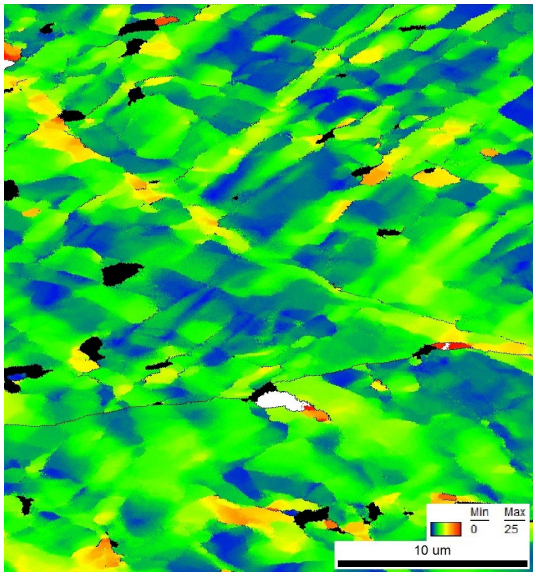

(d) GROD map

Figure 62: Detail 2

An high resolution map (pixel size 0.04μm) was carried out in the area named as detail 3 in the center of figure 58. One interesting observation is that the cell formation seems to be altered by the particles. Figure 63c shows cells grown between of two particles (highlighted with arrows). Furthermore high misoriented bands touch particles (highlighted with a line in figure 62d). Also high angle boundaries (misorientation higher than 11°) are built here and shown as black lines.

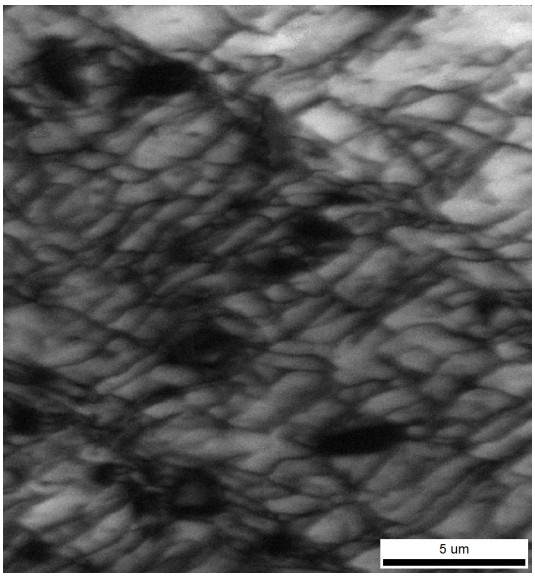

(a) IQ map

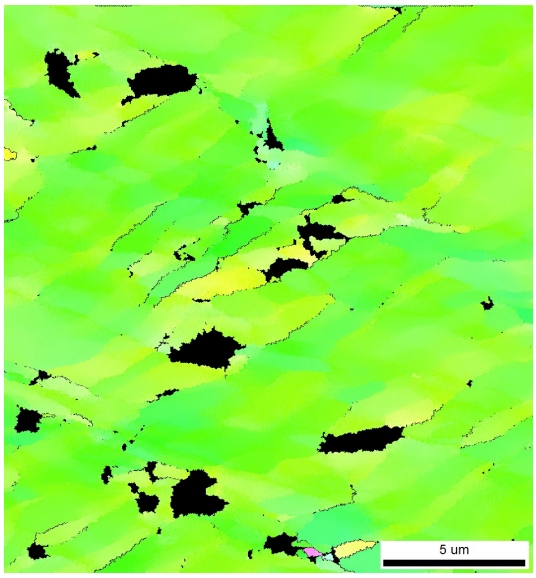

(b) IPF map

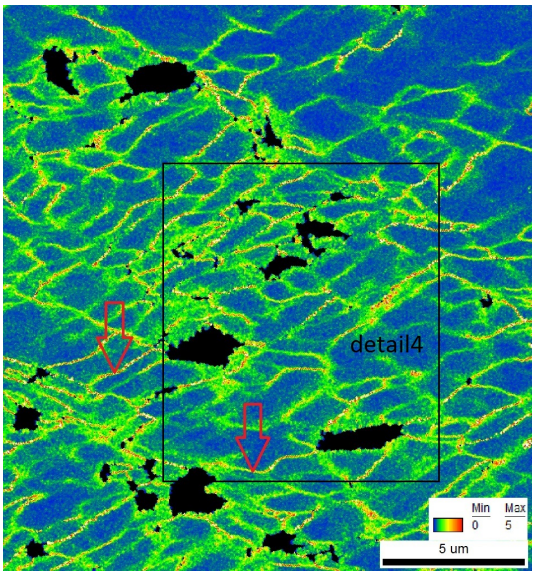

(c) Kernel map

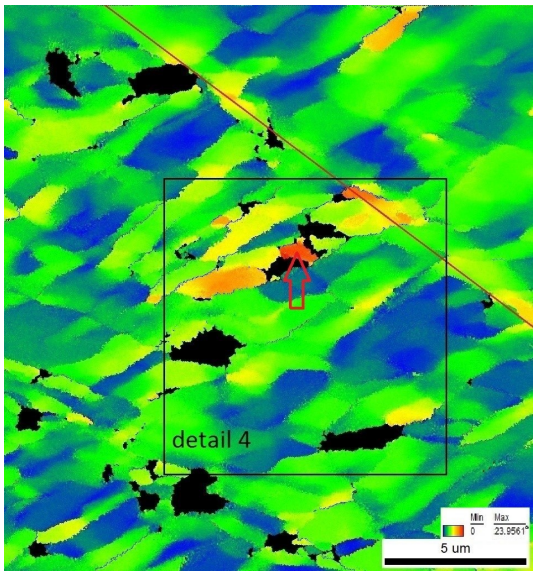

(d) GROD map

Figure 63: Detail 3

Detail 4 is investigated at a higher resolution and a pixel size of 0.02μm (figure 64). The maximum values in the Kernel map of detail 3 (figure 63c) are higher than the maximum values in detail 4 (figure 63c) due to their difference in pixel size. In the center of the GROD maps in figure 63d and 64b the same area is highlighted with an arrow. The difference in GROD maps is due to the definition of grains. In figure 64b the area is defined as a grain, and therefore a low GROD signal is obtained.

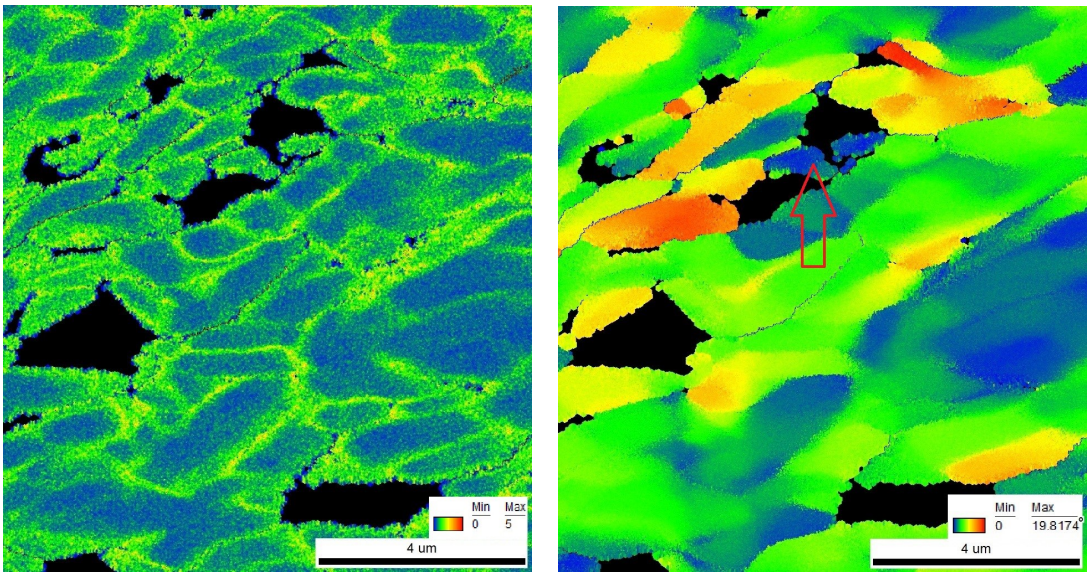

(a) Kernel map (b) GROD map

Figure 64: Detail 4

11.2. Hot Rolled + Homogenized Sample after Plane Strain Test at RT

Homogenized and plane strain cold deformed samples are investigated in order to have a different condition with respect to the particle morphology. After the homogenization treatment (figure 22) the particles are bigger but still non spherical (see figure 23). Therefore a quantitative analysis of the misorientation with respect to the particle size is not possible, since neither the particle size nor the particle shape is clearly allocable in a two dimensional image of the micro structure. Figure 65 and 66 show the sample deformed in the center and in the transition zone, respectively. The micron bar is 35 micron and aligned into rolling direction. At the center the sample is compressed at larger and uni-axial strain, while the sample is less deformed and shear components are present in the transition zone.

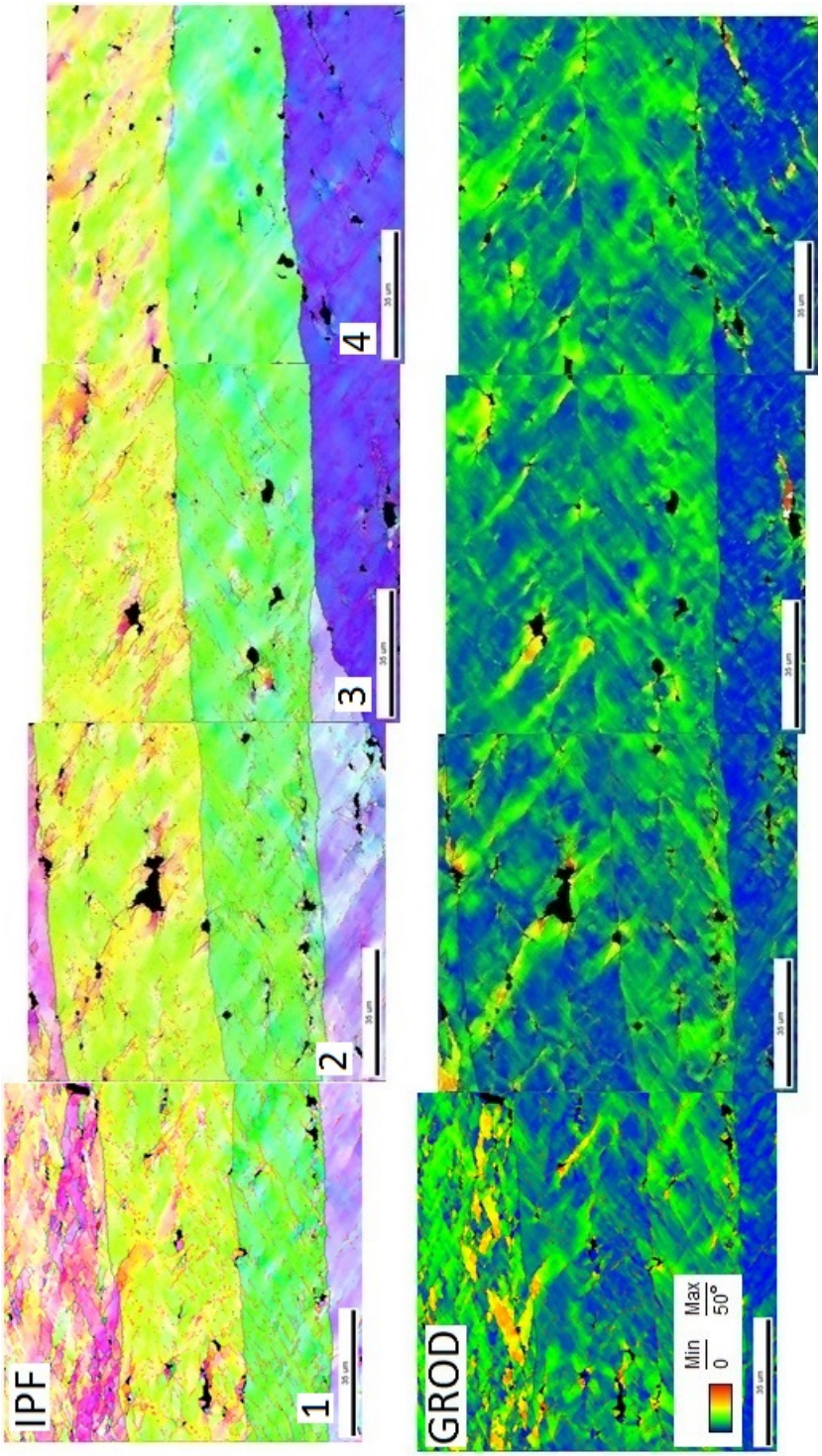

Figure 65: IPF and GROD maps of homogenized and plane strain cold deformed sample in the center

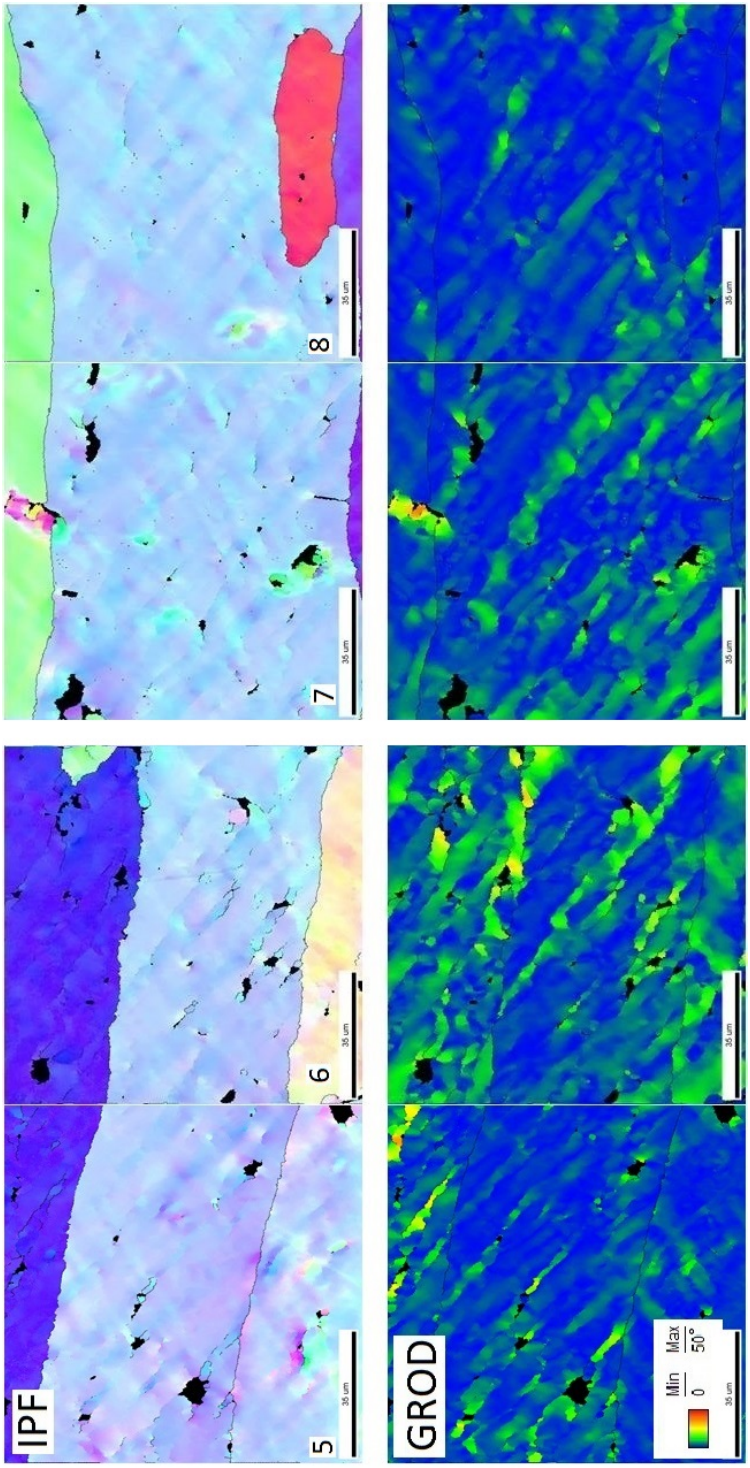

Figure 66: IPF and GROD maps of homogenized and plane strain cold deformed sample in the transition zone

In figure 65 bands of high misorientation are aligned from top left to bottom right or from top right to bottom left. These bands are affecting the misorientation near the particles, because if a band is aligned from the top left to the bottom right, there is also high misorientation top left - bottom right near to the particle. Since material in that quadrants rotates anticlockwise (compare with figure 60), the material rotation anticlockwise should be stronger than clockwise. Since the orientation of the bands is varying, they do not have an influence on the direction of material rotation near particle in average. On the other hand, in the transition zone (figure 66) the bands are always aligned in one direction, namely from the top left to the bottom right. The high misoriented zones near the particles are also always oriented in this way. The maximum values of misorientation in mapping 1 to 8 differ. This is due to different local strains. The strain in the center is approximately 0.5 while in the transition zone it is estimated to be around 0.3. The average value of Kernel average misorientation mappings is used to get a qualitatively idea about the local strain (figure 67). The local strain in the transition zone is lower than in the center resulting in lower misorientations in mappings 5 to 8 than in mapping 1 to 4.

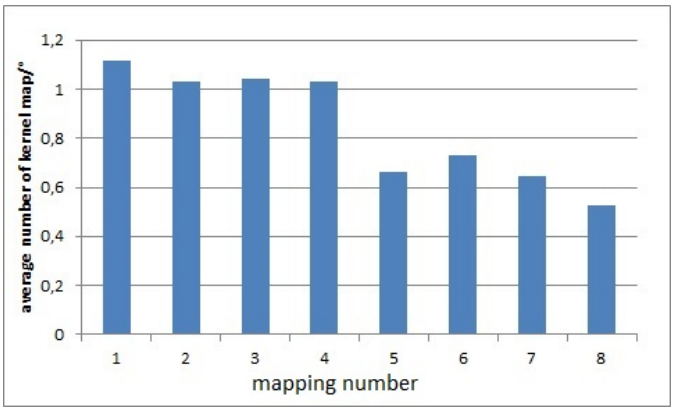

Figure 67: Average Kernel values for different mappings

12. Softening after Annealing

12.1. Softening of Cold Rolled Samples

Annealing of cold rolled samples (table 2) gives an overview of softening. Softening is due to recovery and recrystallization, since they both cause a reduction in stored energy. The decrease of stored energy is measured by hardness tests. Figure 68 shows hardness and dislocation density as function of the annealing temperature after 2 and 10 minutes of annealing. The dislocation density is calculated in two steps. First, the stress is calculated using the equation 39. Then, the dislocation density is calculated using equation 38.

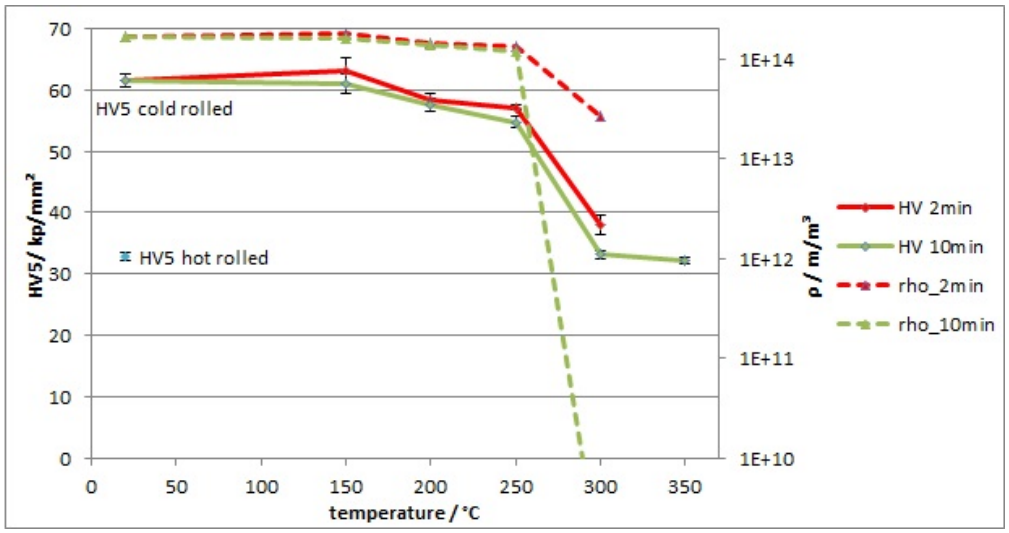

Figure 68: Hardness and dislocation density after annealing for 2 and 10 minutes, as a function of the annealing temperature

Up to an annealing temperature of 250°C, the hardness decreases slowly. Furthermore the hardness after 10 minutes is slightly lower than after 2 minutes of annealing. From 250°C to 300°C there is a more significant drop of hardness. The difference in hardness after 10 minutes and 2 minutes annealing also gets bigger. The hardness after 10 minutes at 300°C is very close to the hardness of the hot rolled sample, which may be related to 100% recrystallization. To assure this solution, an additional test at 350°C for 10 minutes is performed. Hardness values are compared in table 12.

Table 12: Hardness of recrystallized samples

hot rolled	cold rolled+10min 300°C	cold rolled+10min 350°C
32.9HV5±0.8	33.1HV5±0.7	32.2HV5±0.6

12.2. Softening of Hot Rolled Samples after Plane Strain

In contrast to the cold rolled samples, the strain distribution of the plane strain cold deformed samples is not uniform. This is the reason to make hardness mappings instead of single hardness points after annealing. First, the annealing treatments of plane strain cold deformed samples is done at 350°C in the Gleeble as summarized in table 4. The hardness distribution of two samples after annealing is shown in figure 69.

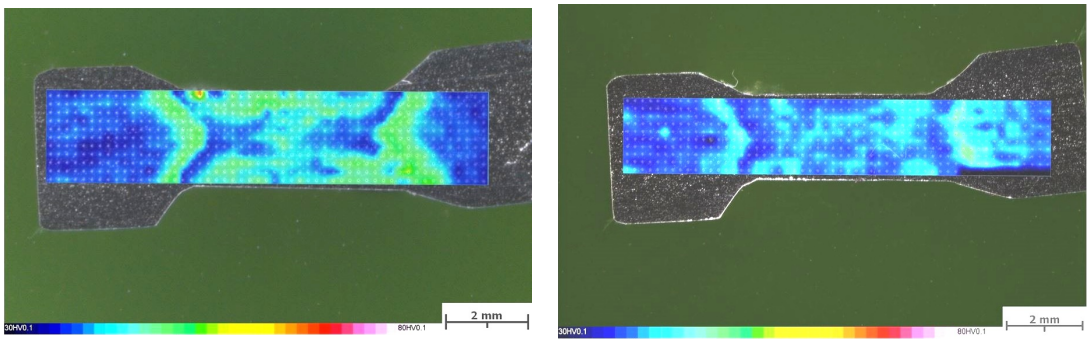

(a) 0 sec at 350°C and water quenching

(b) 60 s holding at 350°C and water quenching

Figure 69: Hardness maps of plane strain cold deformed samples after resistant heating at 20K/s in the Gleeble and holding at 350°C

Annealing after the cold deformation of a sample produces softening due to recrystallization and recovery, this last with little decrease of hardness. Furthermore the qualitative distribution of hardness is maintained during recovery, whereas recrystallization starts at places of high stored energy and places of high hardness after deformation will soften faster during recrystallization. At 350°C recrystallization seems to happen during heating, because even without any holding time one fraction is recrystallized. The zones of the deformation crosses, which are the zones of highest strain, recrystallize first. After 60 seconds holding time the recrystallized fraction increases and the volume between the tools is nearly full recrystallized. In the transition zone, there is a sharp line, which divides the recrystallized material from the non-recrystallized material. Since one goal of this work is to observe the early stages of recrystallization, an annealing temperature of 350°C is too high, because recrystallization happens too fast. The annealing treatments of cold rolled samples suggest a recrystallization temperature of approximately 300°C (section 12.1). Figure 70 shows the hardness map of a partially recrystallized plane strain sample which was annealed at a nominal temperature of 250°C for 2 minutes. Recrystallization only takes place in the vicinity of one of the deformation crosses. This suggests that there might be a small difference in local strain between both deformation crosses, due to friction heterogeneities, as shown in figure 53. On the other hand an inconsistency is observed at one sample annealed for 5 minutes at 250°C in the Gleeble which does not show recrystallization. Furthermore two cold deformed samples both annealed in the Gleeble for 2 minutes at 300°C show large differences: One sample is only slightly recrystallized at places of local strain larger than ε_{local}=0.9 and the other

sample at places of ε_{local}=0.5, meaning sample is nearly full recrystallized.

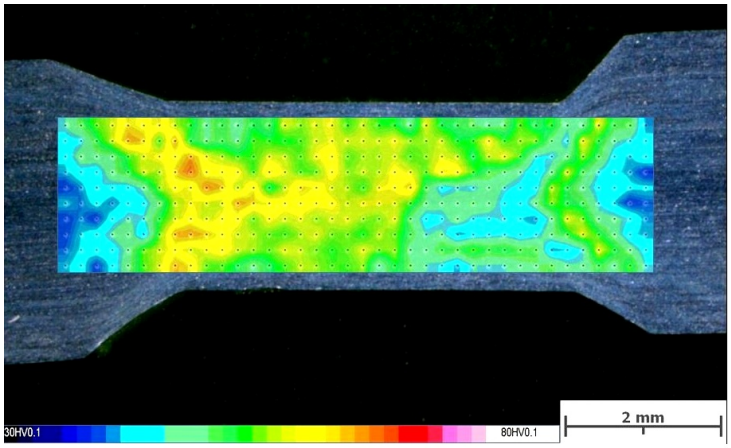

Figure 70: Hardness distribution of a sample plane strain plus annealed at 250°C for 2 min.

To bring the observations in line, oven annealing is performed with plane strain cold deformed samples (table 6). The samples annealed at 200°C and 250°C do not show new grains in the micrographs (see figure 71).

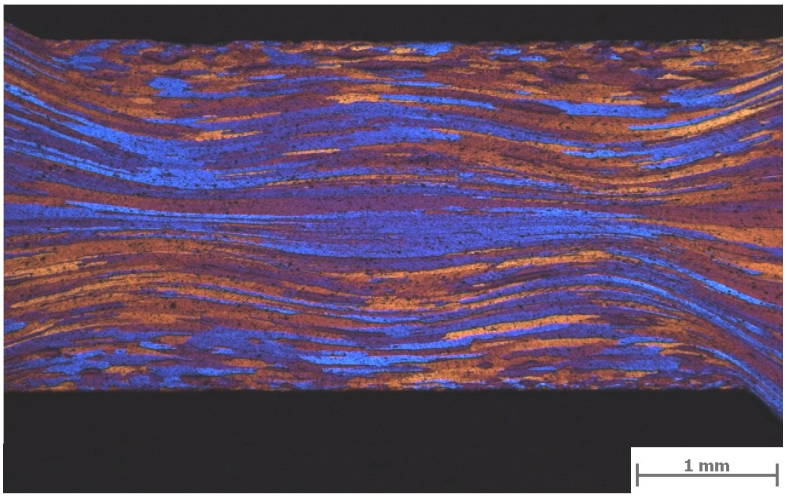

Figure 71: Microstructure after plane strain deformation and oven annealing for 1 hour at 250°C

Additionally, a hardness map performed before annealing (figure 72a) and after annealing for one hour at 250°C (figure 72b) for the same sample shows that sample isn't softened after the annealing treatment. It should be noted that the comparison of cold deformed and annealed cross section is limited to some extent, because during metallography approximately 1 mm of material is removed.

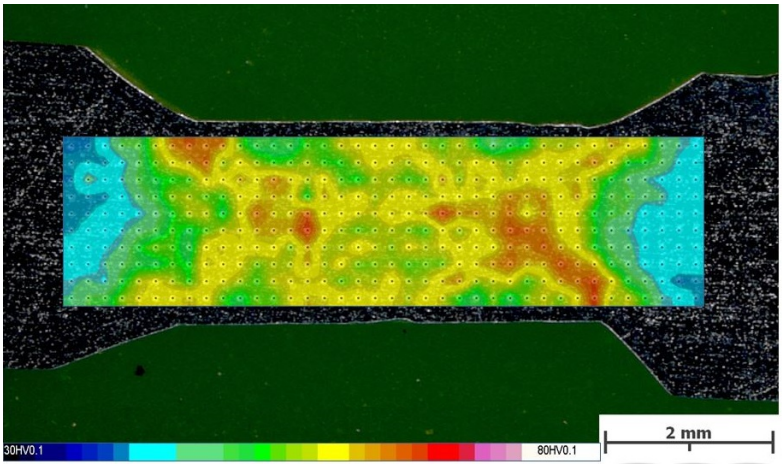

(a) cold deformed

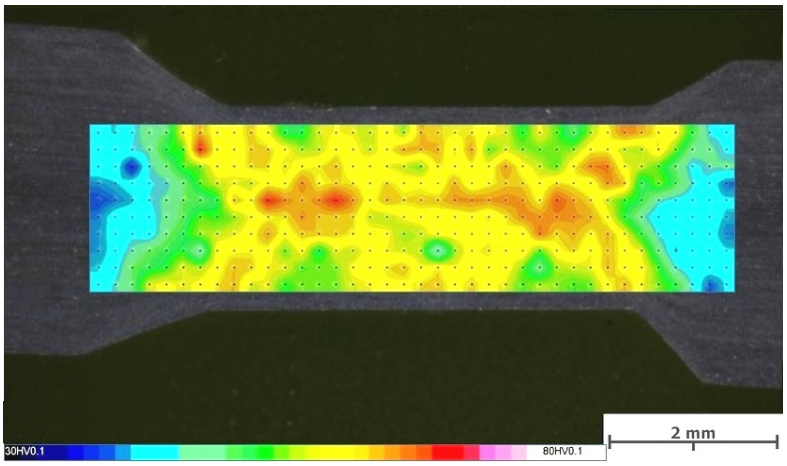

(b) cold deformed and oven annealed at 250 °C for 1h

Figure 72: Comparison cold deformed and annealed sample

In figure 72 there is no substantial decrease of hardness after annealing, meaning that after one hour at 250°C there is no recrystallization. Summarizing:

- cold rolled samples with equivalent strain of 0.89 do not recrystallize after 10 minutes at 250°C and they are partially recrystallized after 2 minutes at 300°C in the oven
- plane strain cold deformed samples with a maximal local equivalent strain of approximately 1 are not recrystallized after one hour at 250°C in the oven
- samples plane strain deformed and heated in the Gleeble give inconsistent results: samples recrystallize between 250°C and 300°C for a holding time of 2 minutes

A temperature control problem in the Gleeble could be the reason of this difference. The temperature is measured with a thermocouple, which is welded directly at samples face

in the center of the cross section (shown in figure 31). Electric current flows through material, which is in between of tools faces. The material in the transition zones and the non-deformed zones does not lie between the tools and is heated by conduction. The highest temperature occurs in the center, which is also the place, where the temperature is measured. Figure 73b shows the temperature-time plot corresponding to sample shown in figure 70. In case of non-uniform electric contact between tools and the sample, electric current is also not uniform. Therefore, there will be a temperature gradient within the sample leading to local temperatures differing from the temperature of the thermocouple. If there is a point with good contact, there is high current in the vicinity of this point, but there is nearly no current far away. Figure 73a schematically illustrates the problem. There is an evidence for contact problems leading to sparks observable as marks on the samples and the tools (figure 27).

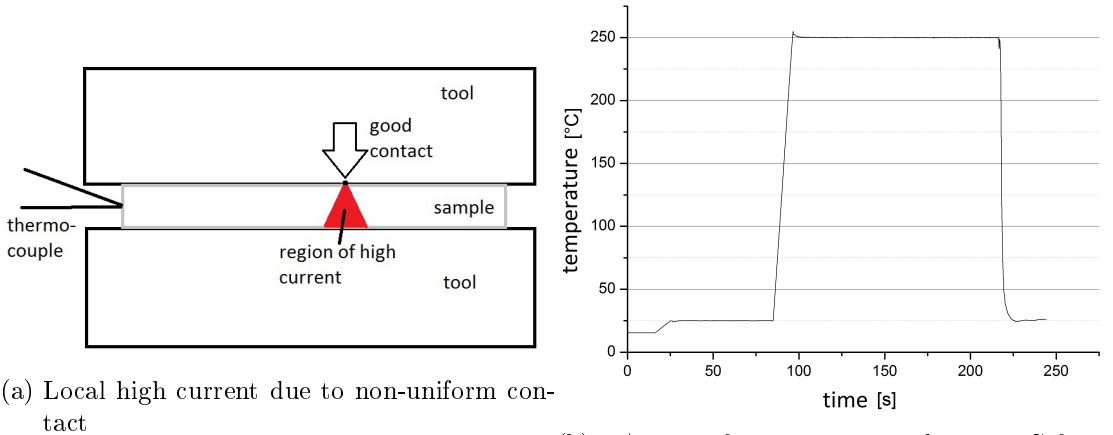

(a) Local high current due to non-uniform contact

(b) T/t-plot of sample annealed at 250°C for 2 minutes

Figure 73: Temperature control during Gleeble annealing

To avoid that kind of problems, a good electric contact over the whole contact surface of tool and sample has to be assured. One important parameter may be flat surfaces of the tools and the sample, which fit together. In case of cold deformation and subsequent annealing, this should be always the case, because sample is plastically deformed before annealing. Another parameter is the contact pressure during heating which should be as high as possible to get a good contact but is limited to avoid creep of the sample. A third parameter to take into account is the lubricant. A nickel based anti-seize compound is used in this work to reduce the friction during deformation. Finally, thermal overshooting can be avoided if lower heating rates are used, because thermal conductance even out the temperature gradients.
Figure 74 shows hardness mappings after cold deformation and after oven annealing at 300°C and 350°C. The sequence of figures is organised in that way that it is possible to compare the distribution of hardness after cold deformation with the distribution after annealing.

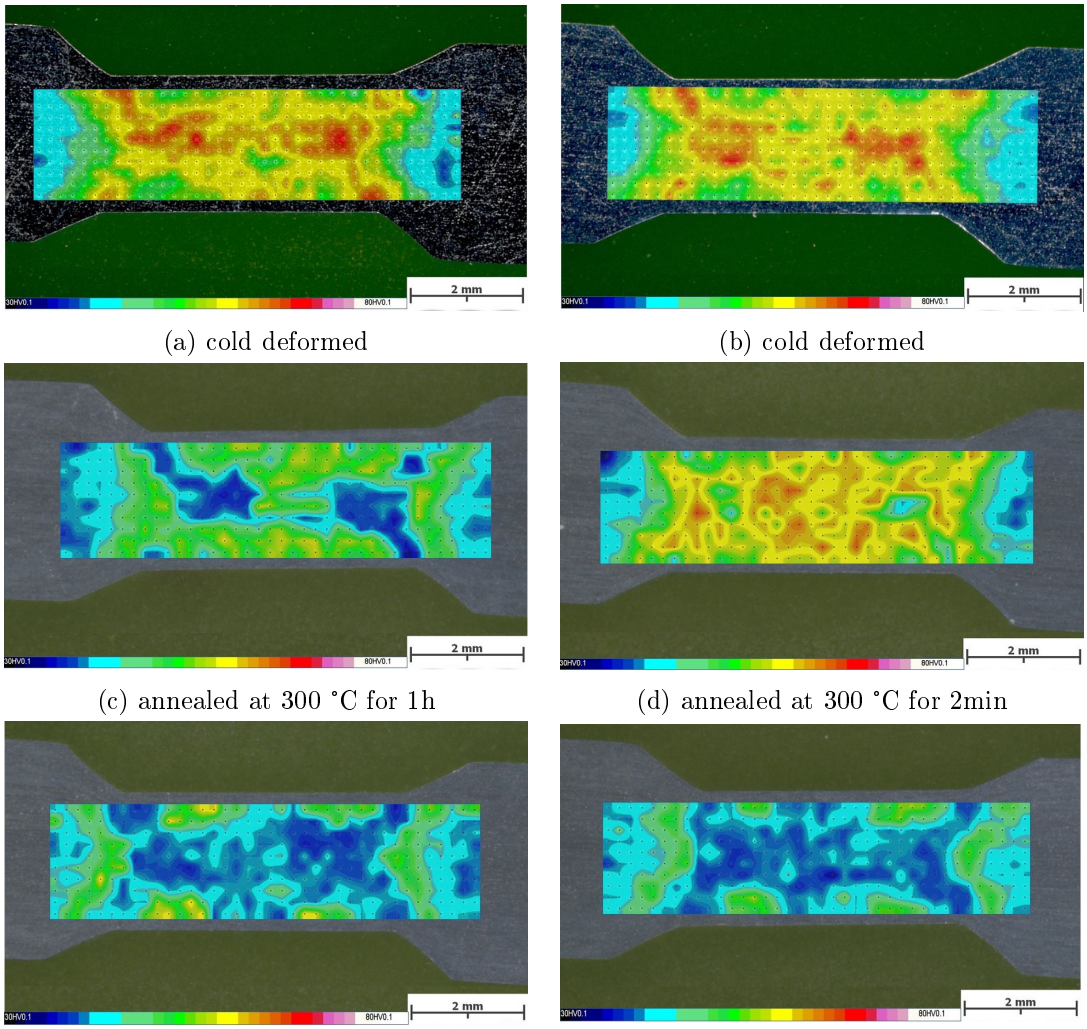

(a) cold deformed

(b) cold deformed

(c) annealed at 300 °C for 1h

(d) annealed at 300 °C for 2min

(e) annealed at 350 °C for 2min

(f) annealed at 350 °C for 1h

Figure 74: Hardness distribution after cold deformation and annealing using one sample. Mappings which are shown in one column are based on one plane strain deformed sample which is cut in the middle and subsequently heat treated.

After 2 minutes annealing at 300°C (figure 74d) there is only recrystallization at some areas of initially high strain at the deformation crosses and at the point where tool meets the sample surface. In the cold deformed state, the strain is not symmetric due to offset of tools similar to the FE-simulation with tool offset (figure 52). If the annealing time is increased to 1 hour at 300°C, the fraction of recrystallized area increases (figure 74c). This hardness map is a good example to illustrate the sensitivity of recrystallization to the strain. Finally samples are annealed at 350°C for 2 minutes (figure 74e) as well as for 1 hour (figure 74f). Both samples have a higher recrystallized fraction than sample annealed for 1 hour at 300°C. For 350°C the recrystallized fraction after annealing for 1 hour is only

slightly higher than after 2 minutes. The recrystallized fraction of the annealed samples depends on the temperature, the annealing time and the local strain. To determine the critical strain for 100% recrystallization, hardness maps are superimposed with strain distribution maps from FE-simulation (figure 75). The strain distribution of FE-solution is obtained by taking tools offset into account.

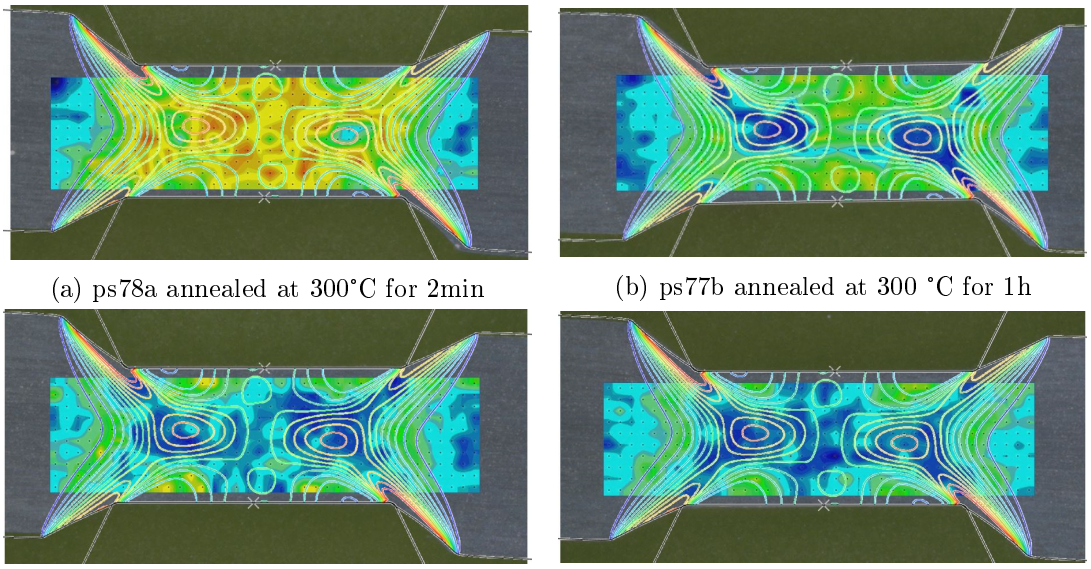

(a) ps78a annealed at 300°C for 2min

(b) ps77b annealed at 300 °C for 1h

(c) ps77a annealed at 350 °C for 2min

(d) ps78b annealed at 350 °C for 1h

Figure 75: Superimposition of hardness and strain maps

The analysis of figure 75 yields following results for the critical strain for 100% recrystallization. Values in table 13 are approximated, since during analysis of figure 75 it is

Table 13: Critical strain for recrystallization

time [min]	temperature [°C]	$\varepsilon^{critical}$
2	300	1
60	300	0.7
2	350	0.4
60	350	0.4

not possible to define a sharp line between 100% recrystallized and partially recrystallized material. For example at figure 75d, there are points with local strain of 0.3 which seem to be recrystallized and points with strain 0.5 with comparable high hardness.

13. Microstructure after Annealing

13.1. Microstructure of annealed Cold Rolled Samples

Cold rolled samples are annealed as shown in table 2. Since there is no microstructural change observed up to an annealing temperature of 250°C, only two micrographs are shown from this temperature range, namely the sample annealed at 150°C for 2 minutes (figure 76a) and the sample annealed at 250°C for 10 minutes (figure 76b). Grains are elongated in the rolling direction.
The hardness measurement of cold rolled and annealed samples in figure 68 show a small decrease of hardness for the sample annealed at 250°C for 10 minutes compared to the sample annealed at 150°C for 2 minutes. Since there is no substantial change in the microstructure, this decrease of hardness refers to recovery.

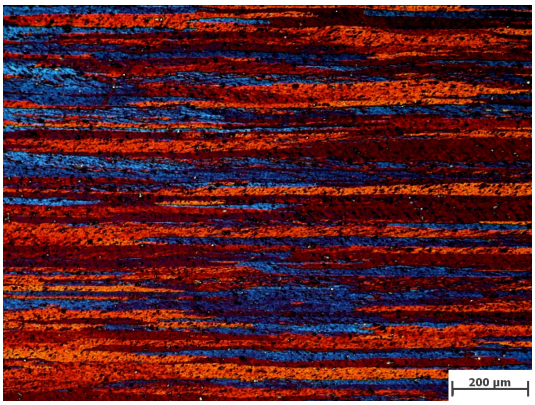

(a) Cold rolled sample annealed for 2 minutes at 150°C

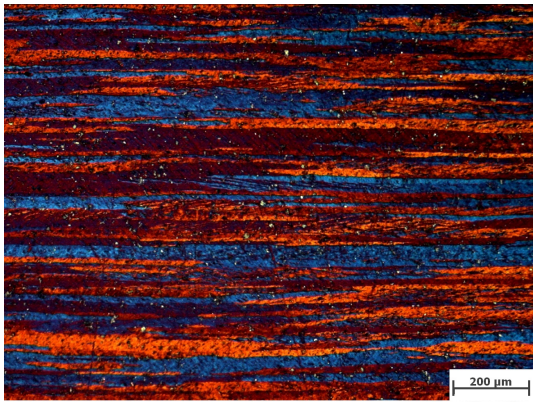

(b) Cold rolled sample annealed for 10 minutes at 250°C

Figure 76: Cold rolled samples annealed at 150°C and 250°C

At an annealing temperature of 300°C a big drop of hardness is observed in figure 68. Recrystallization is observed at the samples annealed at 300°C for 2 and 10 minutes (figure 77 and figure 78). Compared to figure 76b there are more grains and they are less elongated. A closer look reveals a difference between the sample annealed for 2 and the sample annealed for 10 minutes at 300°C: elongated grains are still visible after 2 minutes at 300°C (highlighted with arrows) meaning that recrystallization is not finished after 2 minutes. This is in accordance with hardness measurement in figure 68. Whether sample annealed for 10 minutes at 300°C is fully recrystallized or not remains unclear, but hardness measurement and micrographs suggest, at least, a nearly fully recrystallized state.

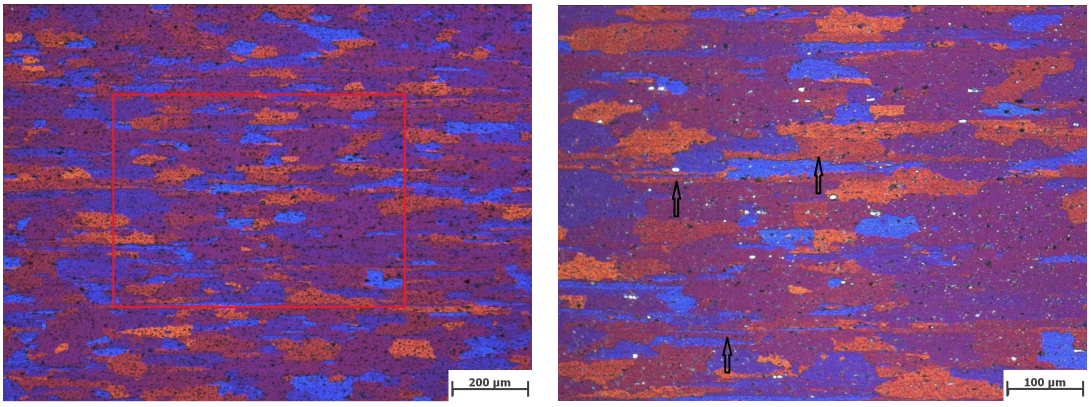

(a) Overview (b) Detail

Figure 77: LOM pictures showing the microstructure of a sample cold rolled and annealed for 2 minutes at 300°C

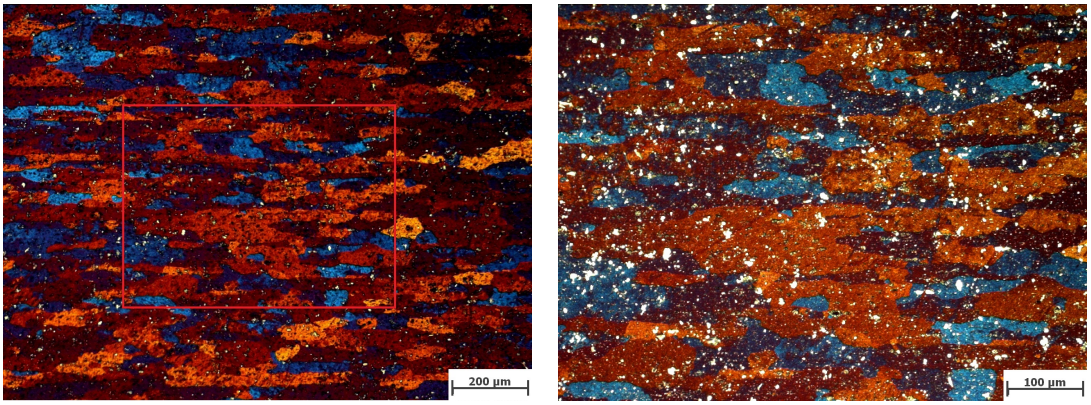

(a) Overview (b) Detail

Figure 78: LOM pictures showing the microstructure of a sample cold rolled and annealed for 10 minutes at 300°C

Samples are almost fully recrystallized after 10 minutes annealing at 300°C, and also are fully recrystallized after 10 minutes at 350°C (Figure 79). There is no difference between samples annealed at 300° and at 350°C, in agreement with hardness measurement in figure 68.

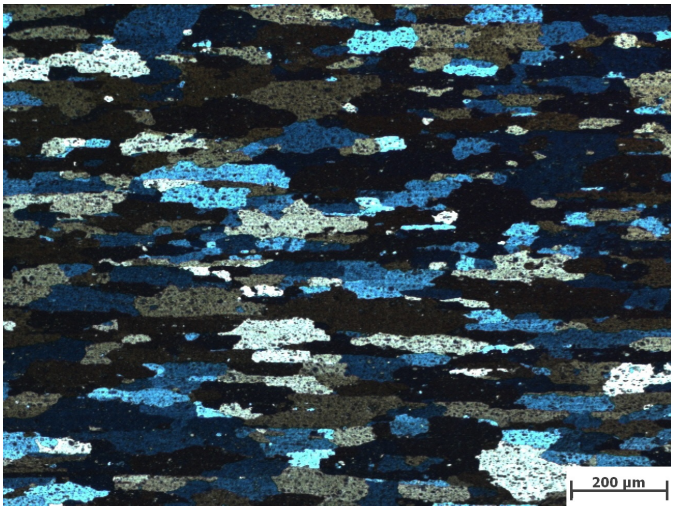

Figure 79: LOM of a sample cold rolled and annealed for 10 minutes at 350°C

Figure 80 shows the microstructure of the sample annealed at 350°C for 10 minutes, analysed in the cross section normal to rolling direction. There are some grains (indicated with arrows), containing some kind of substructure similar to cold deformed microstructure suggesting that there is a small fraction which is not recrystallized.

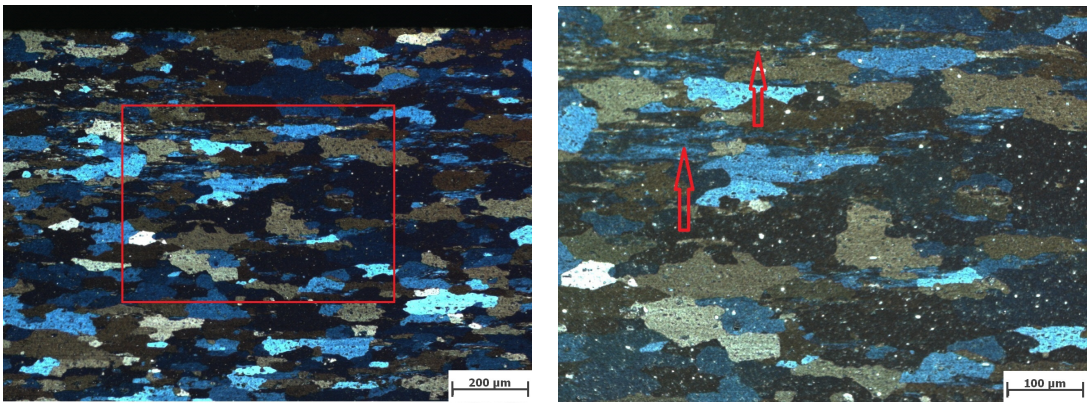

(a) Overview (b) Detail

Figure 80: LOM showing the microstructure of a sample cold rolled annealed for 10 minutes at 350°C (analysed in plane ND-TD).

13.2. Microstructure of annealed Plane Strain Samples

The micrographs in figure 81 belongs to the same sample which was also investigated by means of a hardness mapping (figure 69a). The sample was heated up with 20K/s to 350°C and water quenched without holding. The overview in figure 81a shows a lot of new grains, and the microstructure seems to be quite recrystallized. There are only four

zones (highlighted with arrows) where grains look like after the cold deformation (figure 56).

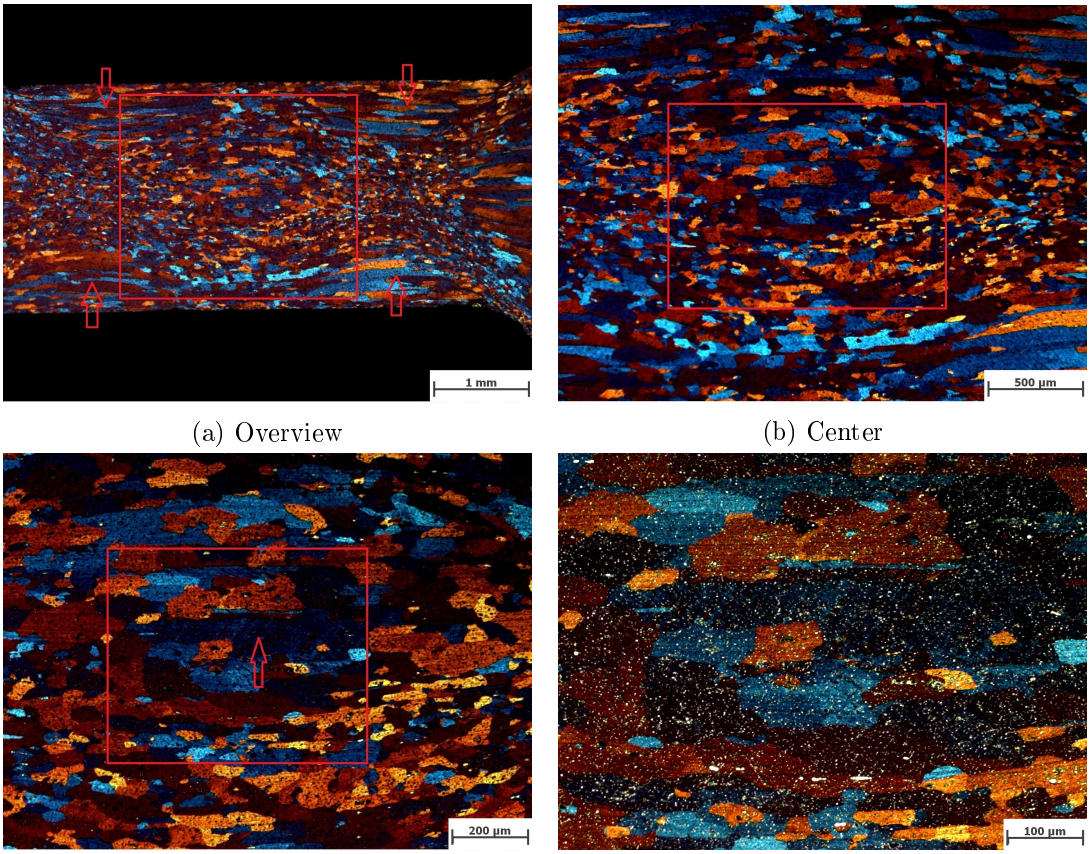

(a) Overview (b) Center

(c) Center2 (d) Center3

Figure 81: LOM showing the microstructure of a sample plane strain cold deformed and heated to 350°C and quenched

There are some grains in figure 81 which are not recrystallized and have a substructure as for example the big blue grain in figure 81c marked with an arrow. Better contrast with respect to substructure is obtained for the sample also heated to 350°C but with 15 seconds holding before quenching (figure 82). There is a clear substructure visible in the yellow grain, which is highlighted with an arrow.

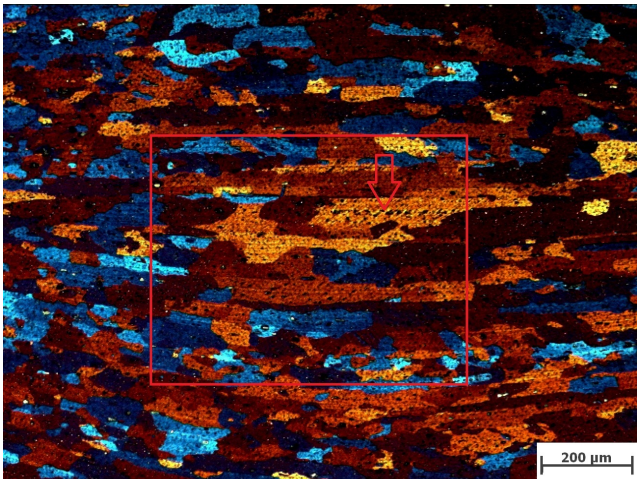

(a) Center of the sample

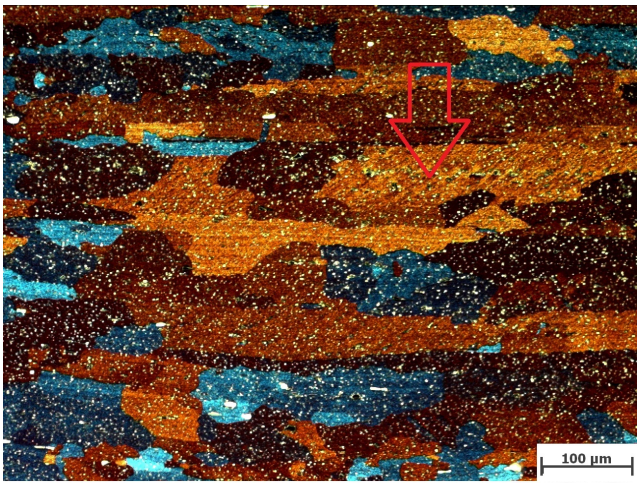

(b) Detail with substructure in yellow grain

Figure 82: LOM showing the microstructure of a sample plane strain cold deformed, heated to 350°C, 15s held and quenched

Figure 83 shows the micrograph of the sample annealed at 350°C for 60 seconds. The picture of center area (figure 83b) does not differ substantially from the sample in figure 81, which was only heated and quenched. From this point of view, hardness maps are a more sensitive tool to quantify recrystallization because there is a clear difference of the corresponding hardness maps in figure 69.
A look at transition zone figure 83c and 83d illustrates how the alignment of new grains is affected by cold deformation pattern (compare with figure 84). The growth of new grains seems to be retarded at original grain boundaries.

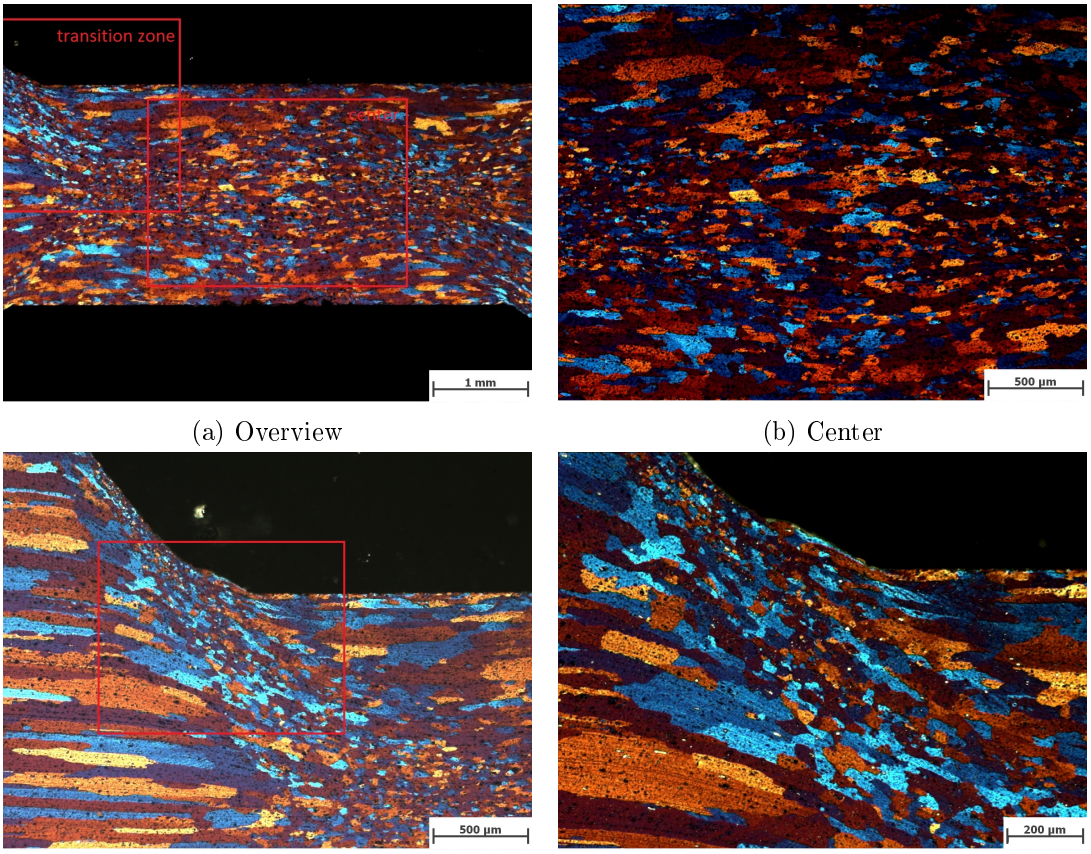

(a) Overview (b) Center

(c) Transition zone (d) Transition zone detail

Figure 83: LOM pictures showing microstructure of a sample plane strain cold deformed, heated to 350°C, 60s held and quenched

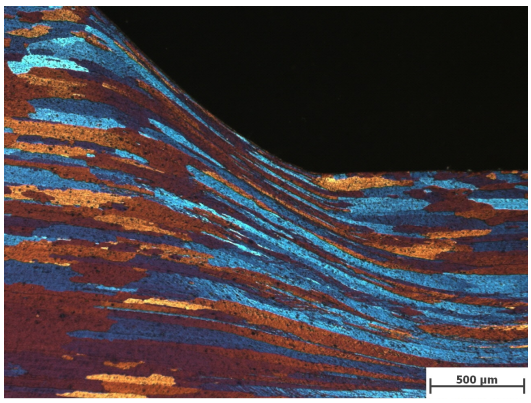

Figure 84: Transition zone after cold deformation

So far only the late stages of recrystallization were observed. To get an idea about

nucleation and growth, sample should be quenched before 100% of recrystallization is reached. In figure 70 the hardness map of a partially recrystallized sample annealed for 2 minutes at 250°C is shown. This sample is also investigated by means of light microscope and EBSD. Figure 85 gives an light microscopic overview the sample. The non-symmetric recrystallization is due to non-homogeneous temperature distribution or non-symmetric strain as already discussed in section 12.2. Further investigation concentrate on the right side of figure 85 (red square).

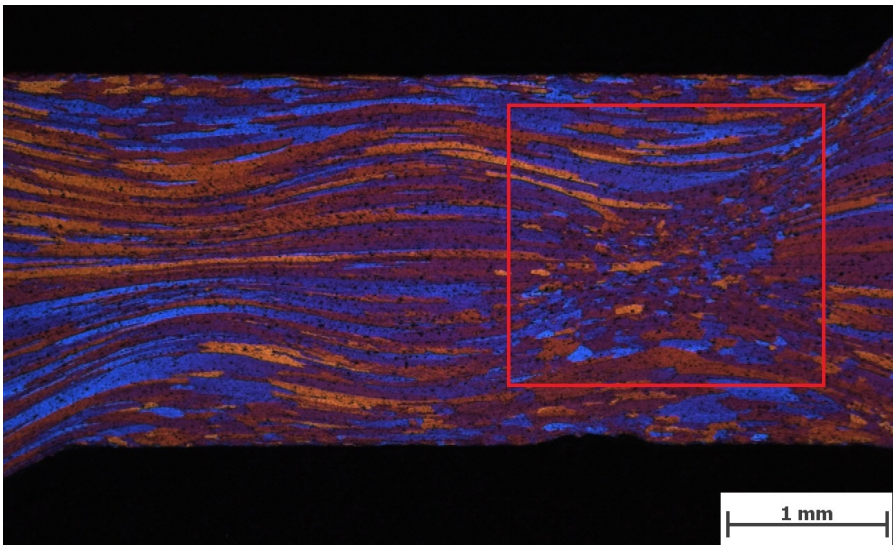

Figure 85: Overview of sample plane strain cold deformed and annealed for 2 minutes at 250°C

In figure 86, the area of investigation is shown. The EBSD measurements allows to determine whether the material is recrystallized or not using image quality map in figure 86c. Dark shaded areas have a distorted crystal lattice, what refers to non-recrystallized material. In the center of the deformation cross, the material seems to be 100% recrystallized. On the top and the bottom of the picture, non-recrystallized grains are observed due to lower local strain (see in section 10). It is interesting to have some non-recrystallized grains which are surrounded by recrystallized ones. The crystal orientation of these grains (indicated with arrows) does not seem to be arbitrary, because in IPF-map (figure 86b) they are preferentially shaded in colours between orange and magenta.

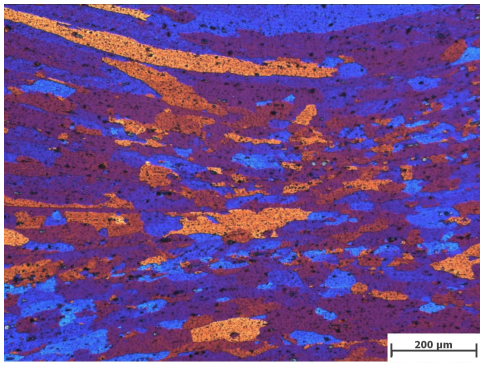

(a) Light microscope

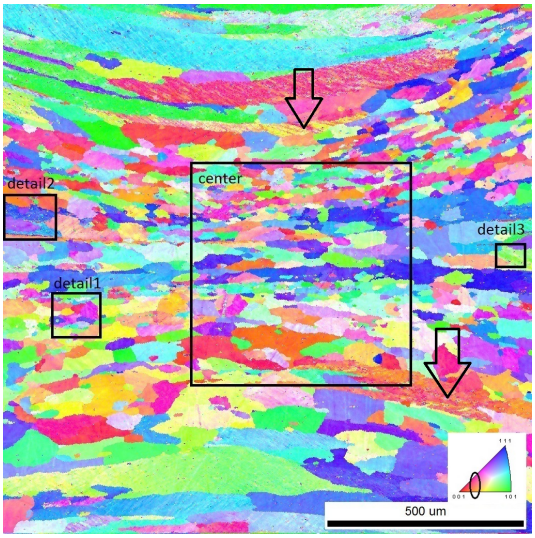

(b) EBSD IPF

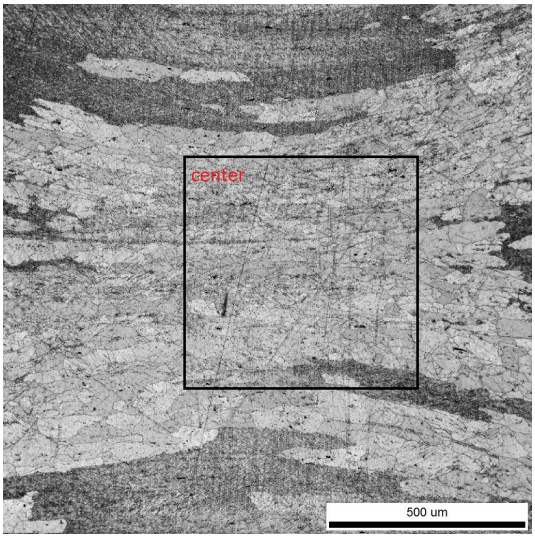

(c) EBSD IQ

Figure 86: Pictures showing the area of investigation of the plane strain cold deformed sample after annealing at 250°C for 2 minutes

A closer look at the center of figure 86c is shown in figure 87 by means of a higher resolution measurement. The two non-recrystallized grains with low IQ values are orange in the IPF map figure 87a. In IPF map there are two prior grain boundaries highlighted to illustrate the alignment of the new grain boundaries.

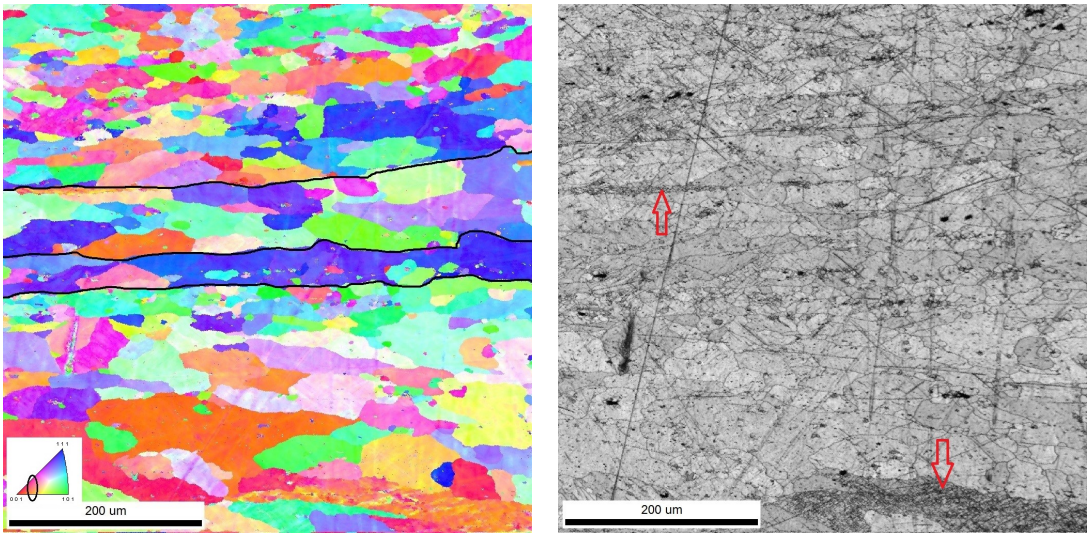

(a) IPF (b) IQ

Figure 87: EBSD measurement showing IPF and IQ pictures of the sample plane strain deformed and annealed at 250°C for 2 minutes

A higher magnification EBSD measurement was done, and some features are shown in detail figure 88. Although there is some substructure in IQ and Kernel map, the material can be considered as fully recrystallized. Grain maps and IPF maps (figures 88a and 88b) reveal the grain structure. In the vicinity of big particles there are many small grains built (especially top left), meaning that particles act as nucleation sites. The substructure must be related to two experimental artefacts: long straight lines are only scratches produced during polishing and curved lines are substructures which are produced due to slightly deformation at the end of the annealing treatment. This deformation causes a plastic strain of approximately 0.05. Therefore this little warm deformation produces the substructure. Preferential site for creation of substructure is the vicinity of particles.

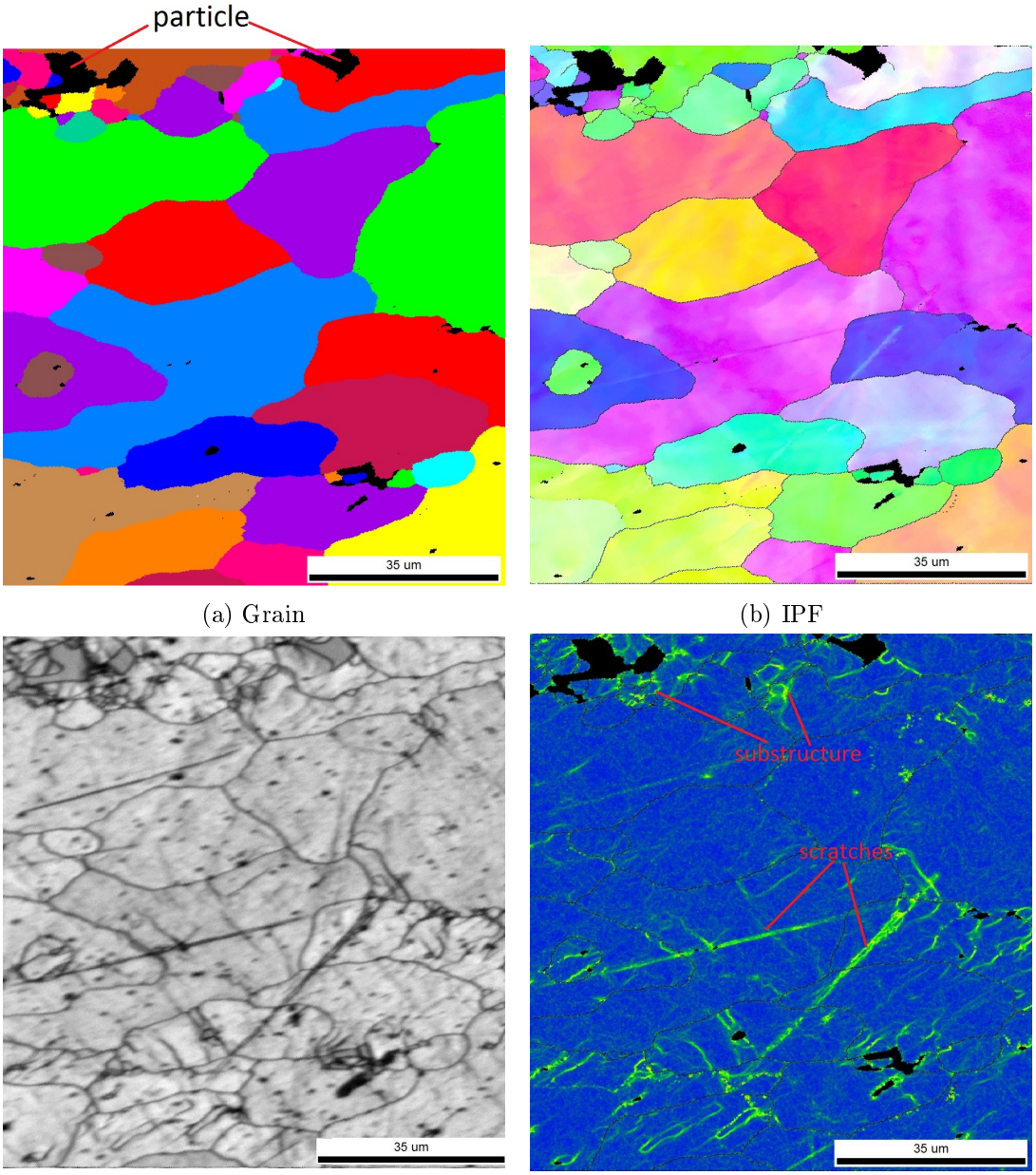

(a) Grain

(b) IPF

(c) IQ

(d) Kernel

Figure 88: EBSD meausurments at detail 1 of sample annealed at 250°C for 2 minutes

The early stages of recrystallization are studied for a condition which is not fully recrystallized. This is the case of detail 2 (figure 89). There are some recrystallized grains with low substructure in IQ and Kernel map (the remaining substructure is an artefact as already mentioned) and there are grains which are not recrystallized. There is no clear evidence for the nucleation sites of most recrystallized grains, since they are

joined to particles as well as to grain boundaries. This is the case for the red, yellow and magenta grains indicated with a star in the grain map (figure 89a). Blue, brown and orange grains exceed the picture size and so nucleation may also happen somewhere else. Comparison of big green grain in grain map and corresponding blue grain in IPF shows that the blue grain in IPF is divided in one big green grain and many small grains in grain map. There are many closed high angular boundaries with misorientation greater than 11°. The rectangle drawn in figure 89c and 89d is shown in figure 90.

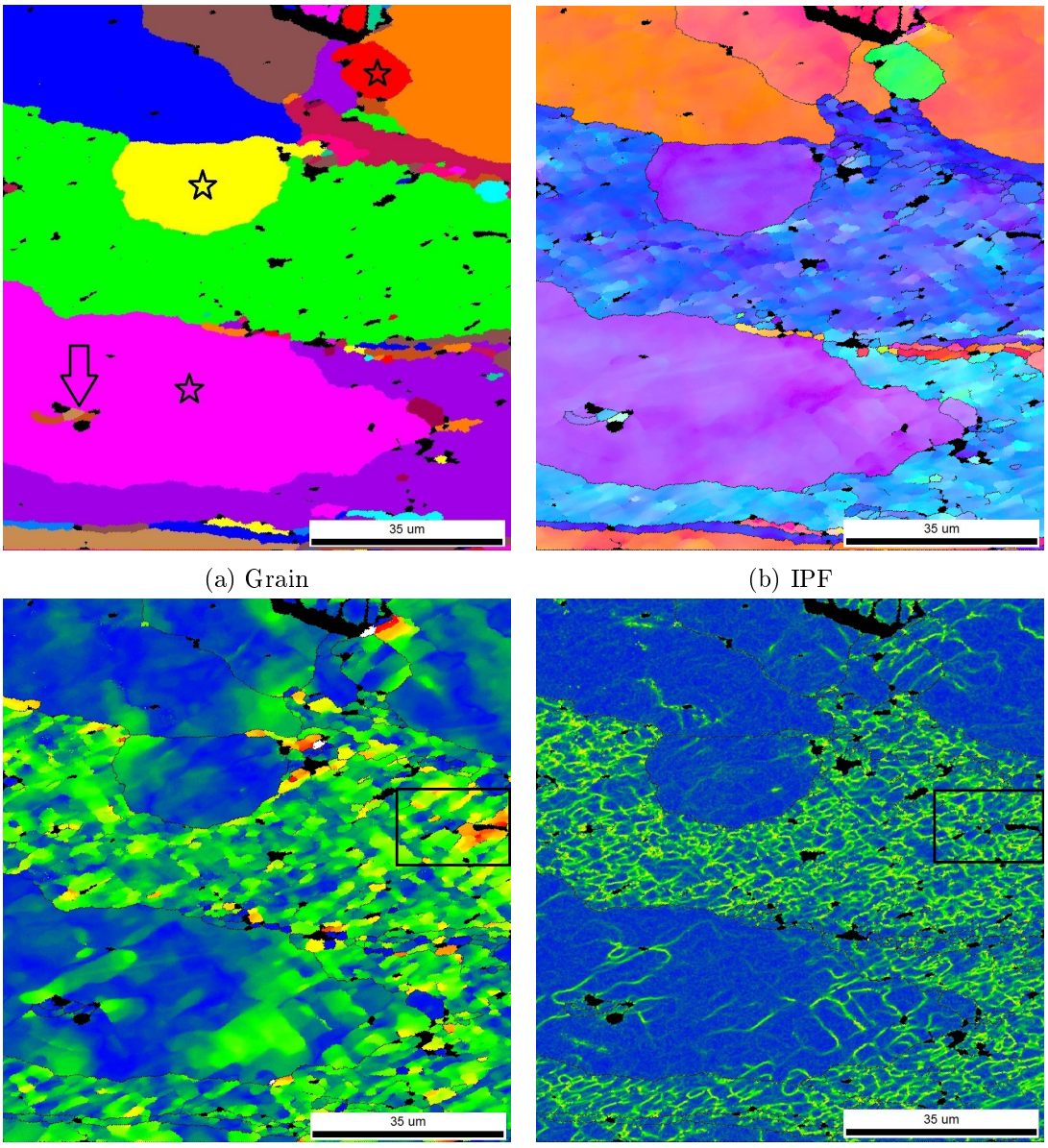

(a) Grain

(b) IPF

(c) GROD

(d) Kernel

Figure 89: EBSD measurement at detail 2 of sample annealed at 250°C for 2 minutes

The subgrain in figure 90 has the ideal condition for nucleation. It has a high misorientation with respect to the surrounding grain and so a high angle boundary has been formed. The local misorientation inside the subgrain (Kernel map) is low and the boundary is able to bulge out. Whether this nucleus will grow fast enough to build a grain or other grains will grow faster, remains unclear from this study. Examples for nuclei which grow not fast enough are shown in figure 89a, where three small brown grains indicated with an arrow have been built inside the big magenta grain.

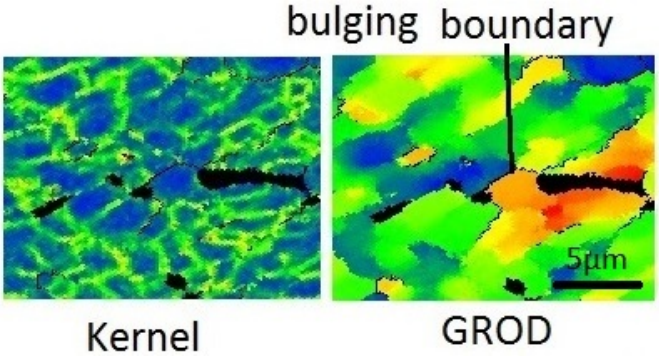

Figure 90: Bulging boundary

In figure 91 a small purple grain has started to grow in the vicinity of a particle (highlighted with black arrow). A bigger purple grain, which has nucleated somewhere on the left side, is growing to the right. The small grain is not able to grow to the left, since there is no stored energy, and it is also not possible to grow downwards due to particles. For the big grain it is easier to overcome particles since the growing surface is much bigger.

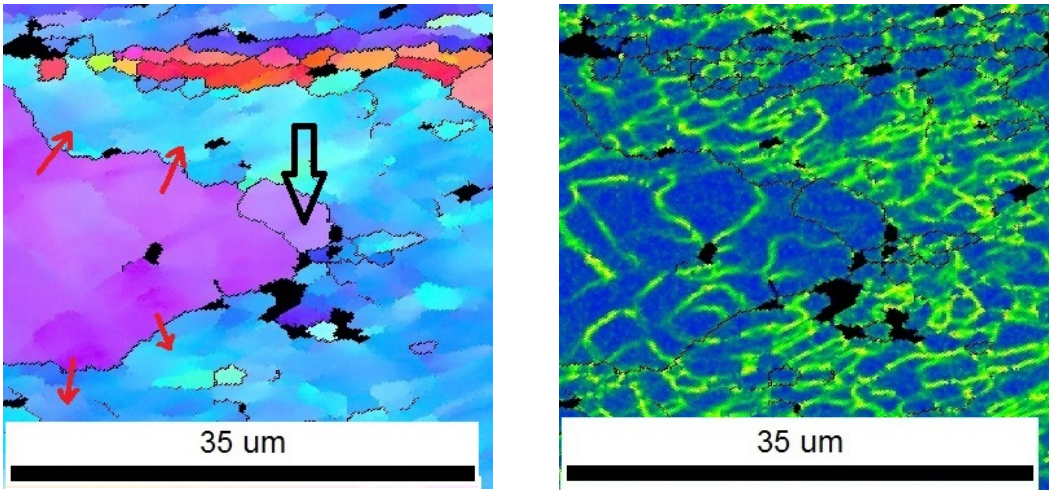

(a) IPF (b) Kernel

Figure 91: Bottom right corner of detail 2

Detail 3 in figure 92 is on the opposite side of the deformation cross (see figure 86b). Although there are some high angle boundaries in the vicinity of particles, they do not seem to move since there no convex side of a boundary having low Kernel values (see figure 92b and 92b inside the circle: area which is black in the GROD map refers to particles). It is not possible to determine the nucleation sites of existing growing grains, since they exceed the picture boundaries.

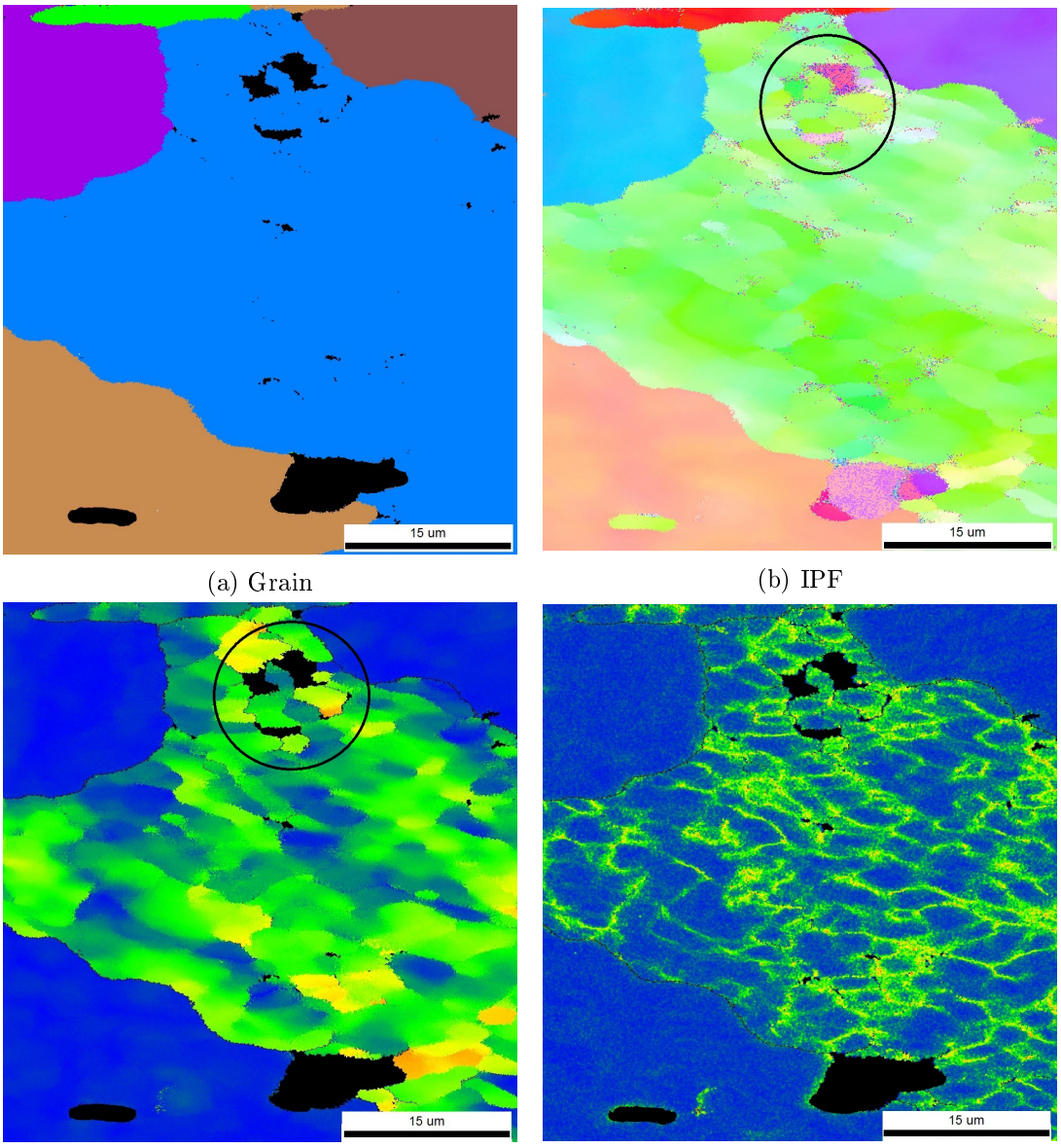

(a) Grain

(b) IPF

(c) GROD

(d) Kernel

Figure 92: EBSD measurement at detail 3 of sample annealed at 250°C for 2 minutes

Larger areas were analysed using LOM. Plane strain cold deformed sample annealed at 300°C for one hour is shown in figure 93. In figure 93d the blue grain in the center is consumed, whereas new grain boundaries indicated with arrows, which started at old grain boundaries move to the center. This effect is well known as strain induced boundary migration SIBM. In this case the length of bulging boundary is 200 micron long. If most new grains start to nucleate at old grain boundaries and move perpendicular to them, the alignment of the new grains will be the same as for old grains. Further the long distance of bulging boundary cause that new grains become also elongated in the direction of the original grains. Finally, boundary movement stops if new grains meet another recrystallized grain.

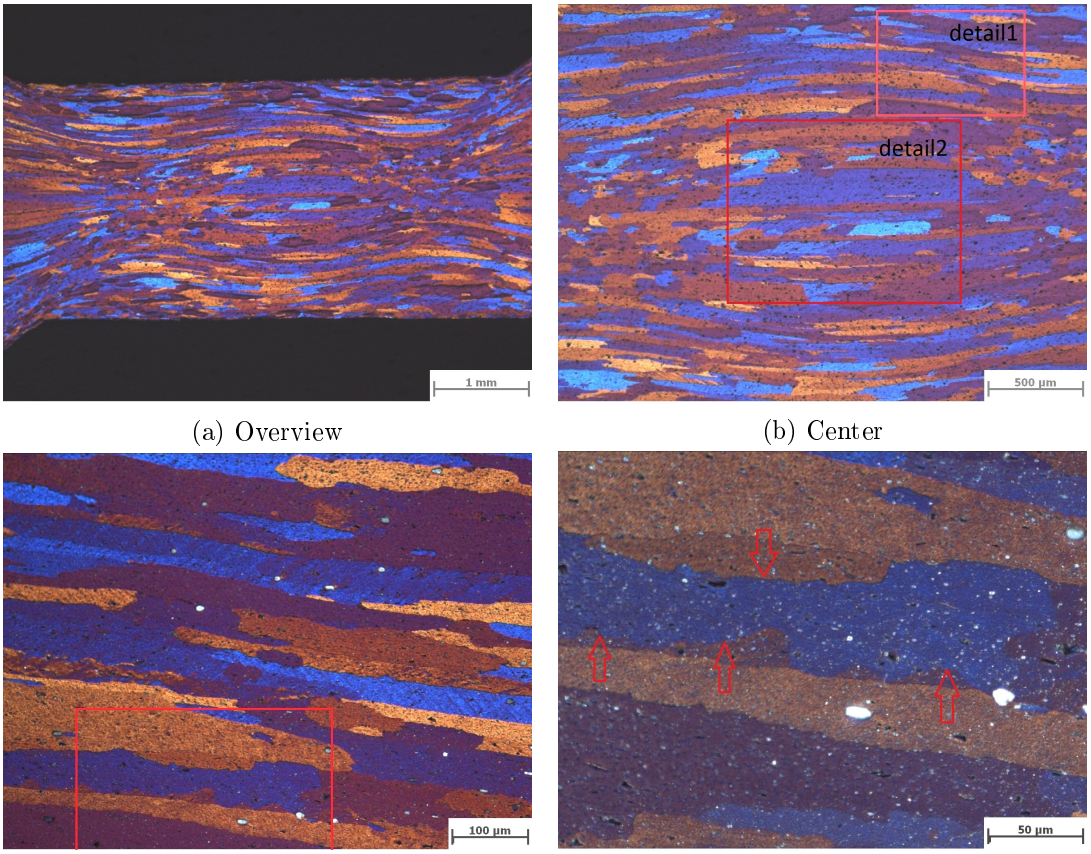

(a) Overview

(b) Center

(c) Detail 1

(d) Detail 1 bulging boundaries

Figure 93: LOM pictures of sample plane strain deformed and oven annealed at 300°C for one hour

In figure 94 the detail 2 of figure 93b is shown. Also here many grains start to grow at original high angle grain boundaries. The most clear case is shown in figure 94c, where an approximately 150 micron long boundary moves downwards (highlighted as black line). There are also some small grains in figure 94c, which nucleated at particles,

but they perhaps will not growth, since their surrounding grain (purple grain) seems to be recrystallized. The information about state of recrystallization of purple grain is obtained from figures 94a and 94b, because the aspect ratio of the purple grain is typical for recrystallized grains.

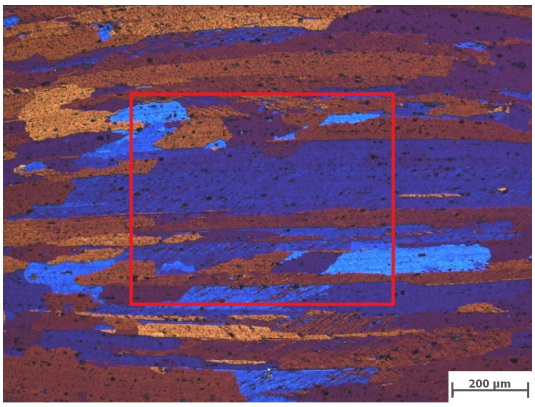

(a) Detail 2

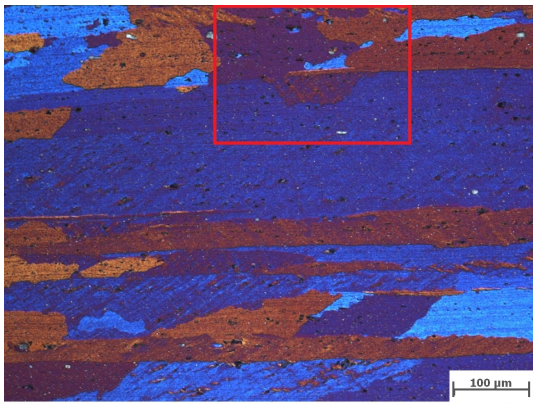

(b) Detail 2

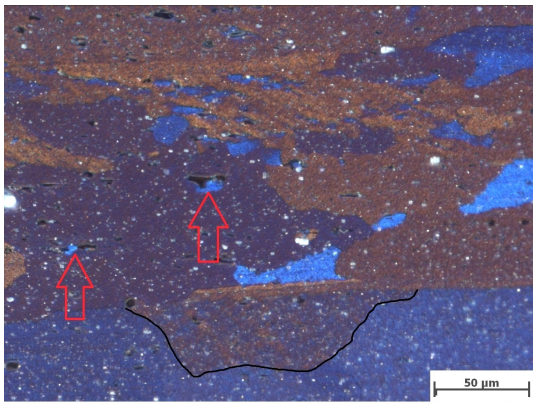

(c) Detail 2 bulging boundary and island grains

Figure 94: LOM pictures at detail 2 of cold deformed sample annealed for 1 hour at 300°C

Sample of figure 95 is annealed at 300°C as sample of figure 94, but only for two minutes. Partial recrystallization occurs at locations of a local strain of approximately 1 in the center of the deformation crosses. There are similar mechanisms for nucleation observed as for sample annealed for 1 hour at 300°C. One difference is the length of the bulging grain boundaries, because bulging length is approximately 50 to 100 microns in figure 95 whereas it is 150 to 200 microns in figure 93 and 94. The bulging length decreases with increasing strain, since sample annealed for 1 hour at 300°C was investigated at local strain of 0.5 in figure 93 and 94.

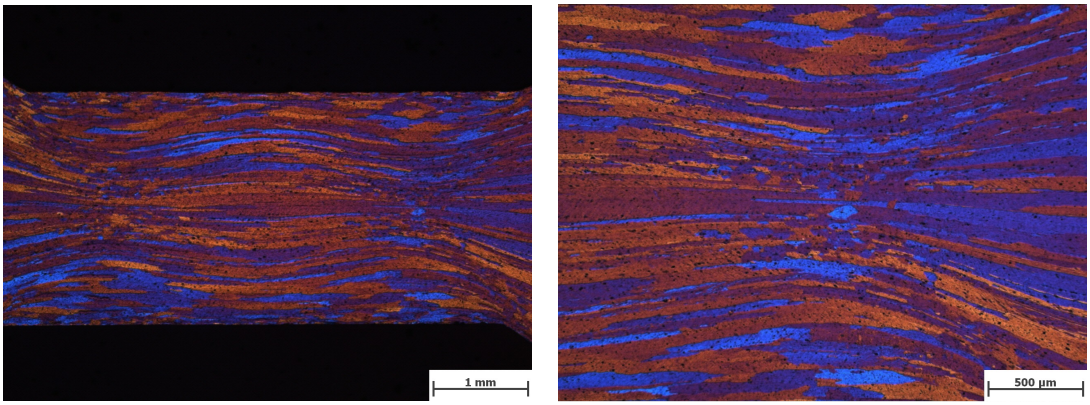

(a) Overview (b) Right cross

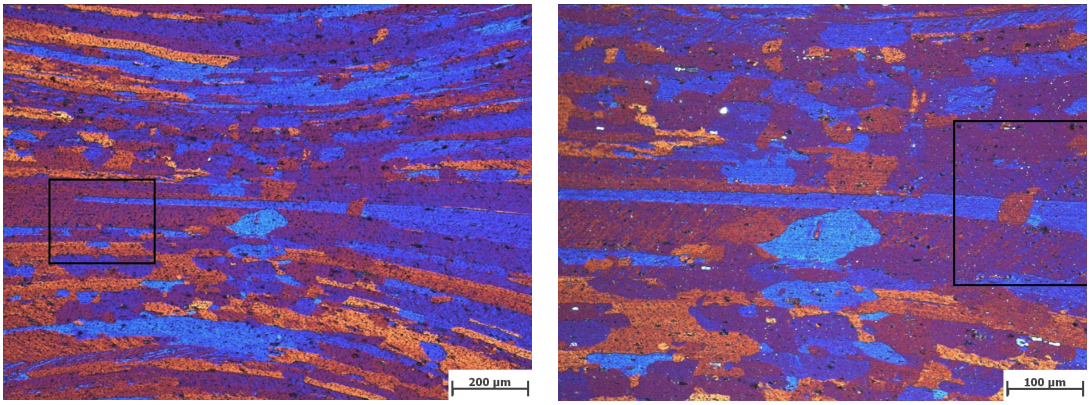

(c) Right cross 1 (d) Right cross 2

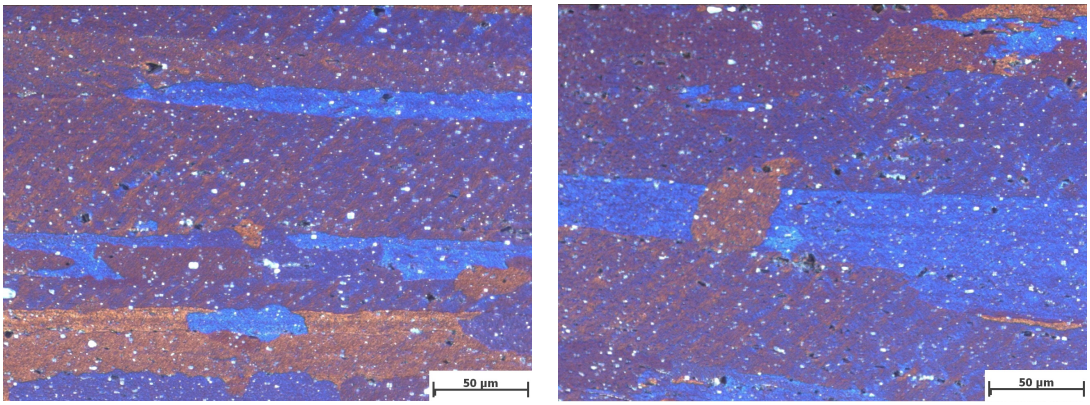

(e) Right cross 1 detail (f) Right cross 2 detail

Figure 95: LOM pictures of sample annealed at 300°C for 2 minutes

Partial recrystallization is also obtained for a sample plane strain cold deformed at a global strain of 0.9 and subsequently annealed in the Gleeble for 2 minutes at 250°C. As already discussed in section 12.2, resistance heating caused troubles and the actual temperature may differ. In figure 96 the center of the sample is shown. The local strain

is approximately 0.9. In figure 96b a new grain (indicated with an arrow) has been built in between of two old grains. So maybe new grains start to grow at the old grain boundaries, and also stop there due to pinning of the moving grain boundary.

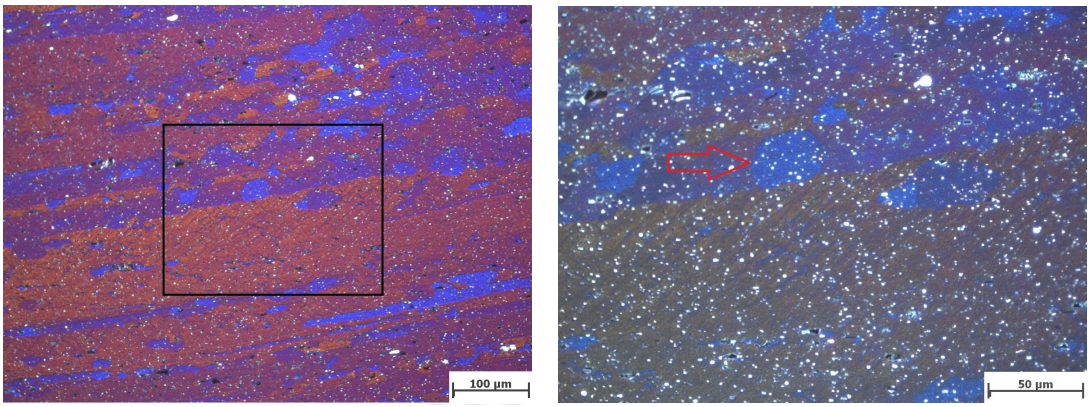

(a) Center (b) New grain blocked by old grain boundaries

Figure 96: LOM pictures of plane strain cold deformed sample at $\varepsilon = 0.9$, tool heated to 250°C, 2min held and quenched

After 2 minutes annealing at 350°C hardness reaches the value of the hot rolled material. In the center of sample (figure 97a) there is clear evidence for a residual non recrystallized grain. At higher strains in the deformation cross small PSN grains are distinguished (figure 97b).

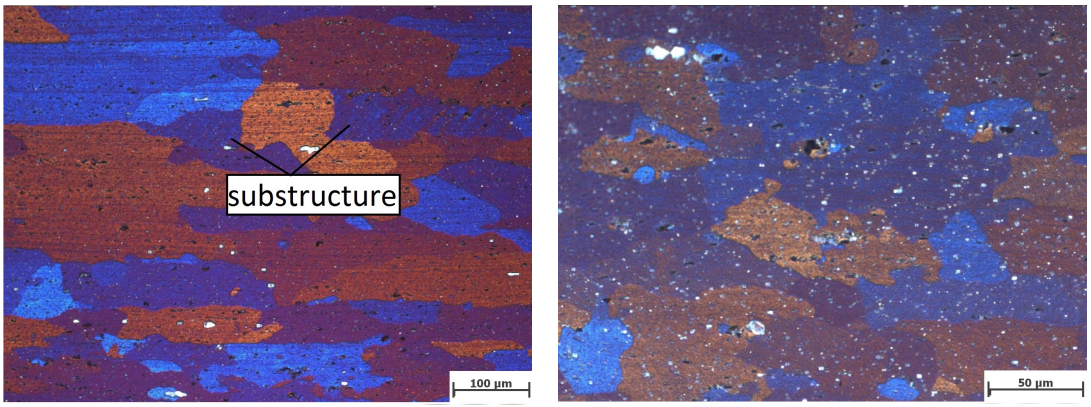

(a) Residual cold deformed grain at center of the sample (b) Smaller PSN grains in the center of the deformation cross

Figure 97: LOM pictures showing plane strain cold deformed sample after 2 minutes annealing at 350°C

Part IV.
Summary and Conclusions

14. Summary and Conclusion

The plane strain cold compression experiments reveal reproducible flow curves (figure 44). A systematic error introduced by the friction can lead to an overestimation of the flow stress. On the other hand additional tensile tests give slightly higher stresses than the plane strain compression tests meaning that the influence of friction during the plane strain tests in this work must be low.
Nevertheless, the influence of friction is discussed in more detail and an equation is derived, which corrects the influence of the friction on the flow curves (equation 22). This equation is validated with FE-simulations and can be used for non-sticking conditions (see table 11). If sticking of the sample occurs, basic assumptions are not valid anymore and the correction method fails. Sticking preferentially occurs if the friction is high and the ratio of the sheet thickness to the tool width is low.
The strain rate for most compression tests is 0.01 s^{-1}. An increase of the strain rate of one or two orders of magnitude leads to a slight increase of the flow stress (figure 47), meaning a strain rate sensitivity m different than zero at room temperature. In the simulations, the strain rate sensitivity can be omitted, since m is small.
Besides the hot rolled samples, samples with an additional homogenisation treatment, are plane strain deformed. There is no difference in the flow curves between both materials, meaning that the coarsening of the Mg_2Si particles, which took place during the homogenisation, does not influence the flow stress of the material.

The local strain is determined by means of FE-simulations and hardness mappings. Therefore, a novel method correlating the hardness and the stress, is used to calculate the strain, using the flow curves (results in figure 55). This method gives comparable strain values than those obtained by FE-simulations. The experimentally determined strain is very sensitive to the stress due to the small slope in the flow curve, and thus small errors in the hardness measurements lead to large errors in the strain map. In a plane strain deformed sample with a global strain of 0.5, the maximum strain in the center of the deformation crosses is approximately 1 and the strain in the center of the sample is approximately the global strain. Furthermore, the strain pattern is a function of the friction. If the friction increases, the two deformation crosses shift to the center of the cross section. FE-simulations performed at different coefficients of friction are compared with the hardness map of a plane strain cold deformed sample. In doing so, it is possible to determine that a value of 0.05 for the coefficient of friction delivers similar strain patterns as in the experiment. Since the friction is rather low, the flow curves are not corrected by the correction factor CF (equation 23).
The hardness is also measured after annealing of the cold deformed samples. After a oven annealing at 250°C, a slight reduction in the hardness is observed. The microstructure

is the same as after cold deformation, meaning that only recovery takes place at this temperature. On the other hand, if heating is performed in the Gleeble machine at a nominal temperature of 250°C, a partial recrystallized sample is produced. This inconsistency may be the result of overheating or, even worse, a heterogeneous distribution of temperature during resistance heating. The critical strain for 100% recrystallization decreases with increasing temperatures. After 2 minutes at 300°C only the areas deformed at approximately a strain of 1 are recrystallized. This strain is reached in the deformation crosses of the plane strain samples. Cold rolled samples of equivalent strain 0.89 and the same annealing treatment are partially recrystallized. For 2 minutes annealing at 350°C, a critical strain of approximately 0.4 is necessary to observe 100% recrystallization. It is difficult to define a sharp limit for the critical strain, because in the hardness maps there are often some measurement points with comparable high hardness values at places of initial high plastic strain. One reason may be the automatic measurement system due to a measurement failure. On the other hand, there are residual grains, which are visible in the micrographs of some samples annealed at 350°C, revealing a substructure similar to the microstructure after cold deformation. A similar observation is made during EBSD measurement of a partial recrystallized sample (figure 86c), where non recrystallized grains are surrounded by recrystallized grains. The crystallographic orientation of residual grains is not random.

Most grains are formed due to grain boundary bulging. This nucleation process may be the reason for residual cold deformed grains, if there are grains which only bulge out and never bulge in. Based on the theory of strain induced boundary migration SIBM, grains of lower stored energy preferentially bulge out (figure 14). A direct observation of bulging boundaries is obtained from the partially recrystallized samples after annealing at 300°C. At a local strain of 0.5 a bulging length of approximately 200μm length is observed whereas at higher local strain bulging length is shorter for samples with the same recrystallized fraction. Many grains start to recrystallize at the original grain boundaries and their growth is stopped by the next grain boundary (figure 96). Therefore, recrystallized grains are aligned with the old grain boundaries.

Many highly misoriented subgrains are observed in the EBSD measurements after cold deformation. Although the misorientation of these boundaries is high, they are not equivalent to grain boundaries due to their larger thickness. During the annealing of the cold deformed samples some small grains grow in the vicinity of the big particles, but they do not have a big influence on the microstructure, since their growth is slow compared to SIBM grains. Thus, the grains nucleating near the particles are then observed as island grains. There are two different explanations for this behaviour. Whether boundaries, which have been built near the particles are less mobile, or the effective pressure on boundary (equation 9) is smaller for the nuclei near to the particles. Since the subgrains near the particles are always smaller than the bulging length at grain boundaries, the retarding pressure due to curvature is always higher at the nuclei near the particles. In addition long bulging boundaries at grain boundaries are able to overcome the obstacles more easily.

Part V.
Outlook

15. Outlook

This work has shown that plane strain tests give reproducible results for flow curves at room temperature, although problems related the temperature control still need to be solved. For further experiments the heating rate, the contact pressure and the lubricant between the anvils and the sample must be optimised to get a more uniform temperature distribution and to avoid overheating.
The distribution of the local strain depends on the actual geometry of the tools and of the sample and the friction. Hence, new FE-simulations and hardness mappings have to be carried out if the experimental conditions are not the same as in this work (especially at higher temperatures).
To get more information about the early stages of recrystallization additional EBSD measurements are necessary. The samples already heated in the Gleeble present artefacts due to the hot deformation after annealing. It means that the plane strain cold deformed samples annealed at 300 °C in the oven should be used for further EBSD measurement, whereas places of partial recrystallized material should be investigated. The analysis of the big bulges coming from SIBM is an interesting task, since there may be some substructure inside the bulges as reported in the literature. In this work, highly misoriented subgrains are observed near big particles after cold deformation. Small grains are visible after subsequent annealing near to big particles. The evolution of the subgrains visible after cold deformation during subsequent annealing is still an open question. One possible method to observe the growth of one special subgrain is to make alternating EBSD measurements and short time annealing treatments [13]. Another possibility to get information about the growth of the subgrains is to compare an ensemble of similar subgrains near particles after just one annealing cycle. Even if the subgrains are similar, they will not grow with the exact same speed. So it seems to be possible to compare different stages of subgrain growth within one micrograph. The local strain path has an influence on the formation of subgrains near particles and can be used to alter the misorientation of subgrains.

References

[1] F.J. Humphreys and M. Hatherly. *Recrystallization and Related Annealing Phenomena.* Elsevier, Oxford, 2^{nd} edition, 2004.

[2] Günter Gottstein. *Physikalische Eigenschaften von Materialien.* Springer Verlag, Berlin, 3^{rd} edition, 2007.

[3] Erik Nes. Modelling of work hardening and stress saturation in fcc metals. *Progress in Materials Science*, 41:129–193, 1998.

[4] Jrmantei. Versetzung im 2D-Kristall. Website, 2010-06-12. Available online at http://commons.wikimedia.org/wiki/File:Versetzung_im_2D-Kristall.svg, visited on November 5th 2013.

[5] F.J. Humphreys M.J. Jones. Interaction of recrystallization and precipitation: The effect of Al_3Sc on the recrystallization behaviour of deformed aluminium. *Acta Materialia*, 51:2149–2159, 2003.

[6] Peter Loidolt. Statische Rekristallisation von AA6082. Project work at Graz University of Technology, 2012.

[7] Dynamic Systems Inc., New York State. *Hydrawedge Mobile Conversion Unit*, 1996.

[8] P. Bate R. Higginson. Substructure drag effects and recrystallization textures in aluminium. *Acta Mater.*, 47:1079–1090, 1999.

[9] Saul Martinez Rehlaender. Plane strain compression testing of aluminium alloy 6061 at elevated temperatures. Master's thesis, The University of British Columbia, 1994.

[10] Gasoila chemicals. Thred gard nickel. Product Data Sheet, 2013.

[11] Jean-Loup Chenot Robert H. Wagoner. *Fundamentals of Metal Forming.* John Wiley and Sons, Inc, New York, 1997.

[12] Z.F. Zhang P.Zhang, S.X. Li. General relationship between strenght and hardness. *Material Science and Engineering A*, 529:62–73, 2011.

[13] N. Bozzolo S. Jacomet, R.E. Logé. Fast in-situ annealing stage coupled with ebsd: A suitable tool to observe quick recrystallization mechanismus. *Materials Characterization*, 70:28–32, 2012.